# Wound healing in the *Arabidopsis* root meristem

by

**Lukas Hoermayer**

August, 2021

*A thesis submitted to the*
*Graduate School*
*of the*
*Institute of Science and Technology Austria*
*in partial fulfillment of the requirements*
*for the degree of*
*Doctor of Philosophy*

Committee in charge:
Prof. Mario de Bono, Chair
Prof. Jiří Friml
Prof. Eva Benková
Prof. Bert De Rybel

The thesis of Lukas Hoermayer, titled *Wound healing in the Arabidopsis root meristem*, is approved by:

**Supervisor**: Prof. Jiří Friml, IST Austria, Klosterneuburg, Austria

Signature: _____

**Committee Member**: Prof. Eva Benková, IST Austria, Klosterneuburg, Austria

Signature: _____

**Committee Member**: Prof. Bert De Rybel, VIB/Ghent University, Ghent, Belgium

Signature: _____

**Defense Chair**: Prof. Mario de Bono, IST Austria, Klosterneuburg, Austria

Signature: _____

Signed page is on file

IST Austria Thesis, ISSN: 2663-337X

I hereby declare that this thesis is my own work and that it does not contain other people's work without this being so stated; this thesis does not contain my previous work without this being stated, and the bibliography contains all the literature that I used in writing the dissertation.

I declare that this is a true copy of my thesis, including any final revisions, as approved by my thesis committee, and that this thesis has not been submitted for a higher degree to any other university or institution.

I certify that any republication of materials presented in this thesis has been approved by the relevant publishers and co-authors.

Signature: _____

Lukas Hoermayer

August, 2021

Signed page is on file

## Abstract

Blood – this is what animals use to heal wounds fast and efficient. Plants do not have blood circulation and their cells cannot move. However, plants have evolved remarkable capacities to regenerate tissues and organs preventing further damage. In my PhD research, I studied the wound healing in the *Arabidopsis* root. I used a UV laser to ablate single cells in the root tip and observed the consequent wound healing. Interestingly, the inner adjacent cells induced a division plane switch and subsequently adopted the cell type of the killed cell to replace it. We termed this form of wound healing "restorative divisions". This initial observation triggered the questions of my PhD studies: How and why do cells orient their division planes, how do they feel the wound and why does this happen only in inner adjacent cells.

For answering these questions, I used a quite simple experimental setup: 5 day - old seedlings were stained with propidium iodide to visualize cell walls and dead cells; ablation was carried out using a special laser cutter and a confocal microscope. Adaptation of the novel vertical microscope system made it possible to observe wounds in real time. This revealed that restorative divisions occur at increased frequency compared to normal divisions. Additionally, the major plant hormone auxin accumulates in wound adjacent cells and drives the expression of the wound-stress responsive transcription factor ERF115. Using this as a marker gene for wound responses, we found that an important part of wound signalling is the sensing of the collapse of the ablated cell. The collapse causes a radical pressure drop, which results in strong tissue deformations. These deformations manifest in an invasion of the now free spot specifically by the inner adjacent cells within seconds, probably because of higher pressure of the inner tissues. Long-term imaging revealed that those deformed cells continuously expand towards the wound hole and that this is crucial for the restorative division.

These wound-expanding cells exhibit an abnormal, biphasic polarity of microtubule arrays before the division. Experiments inhibiting cell expansion suggest that it is the biphasic stretching that induces those MT arrays. Adapting the micromanipulator aspiration system from animal scientists at our institute confirmed the hypothesis that stretching influences microtubule stability. In conclusion, this shows that microtubules react to tissue deformation and this facilitates the observed division plane switch. This puts mechanical cues and tensions at the most prominent position for explaining the growth and wound healing properties of plants. Hence, it shines light onto the importance of understanding mechanical signal transduction.

## Acknowledgments

I would like to thank my supervisor Jiří Friml, whom I am very grateful of his constant support and encouragement to pursue my PhD project. It has been a delight to work with him and in his group. I would especially like to thank him for convincing me to start with the PhD program and hence leading me towards great and interesting 5 years of academic and personal education.

I would like to thank my family, my parents Elisabeth and Lorenz and my brother Hannes, and my friends for their lifelong support of my ideas and dreams.

I would also like to thank all my colleagues and friends at IST for their valuable support, help, constructive feedback and great fun moments we have had together.

I would like to thank staff at the Bioimaging and Life Science Facilities at Institute of Science and Technology Austria for their invaluable assistance. I have received funding from the European Research Council (ERC) under the European Union's Seventh Framework Programme (FP7/2007-2013)/ERC grant agreement 742985 and from the Austrian Science Fund under stand-alone grant P29988.

I would like to thank my committee members Eva Benková and Bert De Rybel for their time and interest in my research and PhD work.

And I would especially like to thank my friends Juan Carlos and Lesia, who shared with me their enthusiasm about science, life and friendship and whom I am extremely grateful for the time we have spent together here at IST.

## About the Author

Lukas Hoermayer completed his BSc in Medicinal Chemistry and Pharmaceutical Sciences at the Dublin Institute of Technology in 2013 and his MSc in Biological Chemistry at the University of Vienna in 2016 and joined IST Austria in April 2016. His main research interests are the wound healing mechanisms in plant roots. Lukas developed a system of long-term imaging of wounded plant roots combining a laser ablation setup with vertical stage microscopy. He published his results about stem-cell activity during wound healing in Cell and his findings about cellular pressure and auxin regulation of tissue regeneration in PNAS.

## List of Publications

**Hoermayer, L.**, & Friml, J. (2019). Targeted cell ablation-based insights into wound healing and restorative patterning. *Current opinion in plant biology*

Marhava P., **Hoermayer L**., Saiko Y., Marhavy P., Benkova E. and Friml J. (2019). Re-activation of stem cell pathways for pattern restoration in plant wound healing. *Cell*

**Hoermayer L.**, Montesinos JC., Marhava P., Benkova E., Yoshida S. and Friml J. (2020). Wounding-induced changes in cellular pressure and localized auxin signalling spatially coordinate restorative divisions in roots. *PNAS*

# Table of Contents

# Chapter 1

## Targeted cell ablation-based insights into wound healing and restorative patterning

Lukas Hoermayer, Jiří Friml

Institute of Science and Technology Austria, 3400 Klosterneuburg, Austria

Published in

Curr Opin Plant Biol. 2019 Dec; 52: 124–130.

**Summary:**

Plants as sessile organisms are constantly under attack by herbivores, rough environmental situations, or mechanical pressure. These challenges often lead to the induction of wounds or destruction of already specified and developed tissues. Additionally, wounding makes plants vulnerable to invasion by pathogens, which is why wound signalling often triggers specific defence responses. To stay competitive or, eventually, survive under these circumstances the plants need to regenerate efficiently, which in rigid, tissue migration-incompatible plant tissues requires post-embryonic patterning and organogenesis. Now, several studies used laser-assisted single cell ablation in the Arabidopsis root tip as a minimal wounding proxy. Here, we discuss their findings and put them into context of a broader spectrum of wound signalling, pathogen responses and tissue as well as organ regeneration.

## Introduction

Well-studied mechanisms of wound healing in animals rely strongly on targeted migration of cells to the wound area. In plant tissues, this is not possible, since plant cells are encapsulated by their rigid cell walls. Thus, regeneration in plants has to rely on oriented cell divisions, acquisition of new cell fates and on directional cell elongation. Early wounding studies in the 19$^{th}$ and beginning of 20$^{th}$ century provided initial phenomenology of regeneration (1, 2, 3) but only in the last decade approaches mainly involving the surgical removal of the root tip provided much insight into the mechanism of regeneration and accompanied transcriptional reprograming (4, 5). However, the cellular processes and, in particular, molecular mechanisms underlying this regeneration response remain poorly characterized. Recent studies employing local, targeted cell elimination in the roots of the model plant *Arabidopsis thaliana* promise to provide fresh insights into the still mysterious mechanism of wound healing in plants.

## Non-targeted wounding studies

Most of the earlier wounding experiments involved surgically induced, rather large-scale injuries in different tissues of various plant models. Originally, these studies involved simple observation of processes following the wounding and, later, mainly with the use of *Arabidopsis* root, they employed global transcriptome analysis and more sophisticated use of molecular markers and other genetic tools.

*Cellular responses during regeneration*

The most obvious response of surrounding cells to wounding is (re)entry into mitosis, also in differentiated cells that have left the cell cycle. These cells dedifferentiate, divide and form the new cell walls parallel to the wound site ultimately filling the wound with new cells (2, 6, 3). In the root meristem, where cells are constantly in the cell cycle, wounding enhances cell divisions in cells close to the wound site; these wound-activated root cells subsequently lose their identity and adopt embryonic/stem cell-like identity (Fig. 1A) (5, 7). Although these processes have been well described, neither the signal that activates the neighbouring cells nor the mechanism coordinating which cells are responsive, have been identified.

Notably, even when the whole stem cell niche of the root is removed, the root meristem pattern is re-established *de novo* with correct arrangement of the lost cell types (Fig. 1A) (4). Single cell sequencing revealed that the newly generated cells quickly adopt the required new cell types, and this is partly dependent on the spatially separated maxima of two major phytohormones, auxin and cytokinin (Fig. 1A). However, this *de novo* cell fate acquisition occurred (albeit with less efficiency) also when these maxima were disrupted, which suggests so far unknown intercellular positional signalling that coordinates the re-patterning of the root tip (5). This highlights the superior ability of plant organs to fully regenerate and restore correct tissue patterns.

*Primary wound signalling*

For the efficient initiation of defence responses and regeneration, plants need to quickly recognize the invaders or the induced destruction and signal to the immediate surroundings and the rest of the plant (8, 9, 10). The first known downstream signalling events that occur after herbivore attack or wounding are $Ca^{2+}$ wave initiation (11, 12) and an accumulation of reactive oxygen species (ROS) (Fig. 1B) (13, 14, 15). Wounding and pathogen associated elicitors also induce the production of small peptides that act as defence activators (16), e.g. Pep1 and Pep2, which activate downstream immune responses against root pathogens (17, 18, 19).

Although these processes are well established to occur after the wounding/herbivore attack and mediate immune responses in plants (for a detailed review see: 20), they are triggered by an initial wound signal that is still unknown. Cell wall integrity sensing by constant measurement of the wall composition (20, 21) is thought to be a crucial element of wound detection. However, no direct, mechanistic connection between the known

components of the cell wall integrity sensing and the wound/herbivore responses has been established.

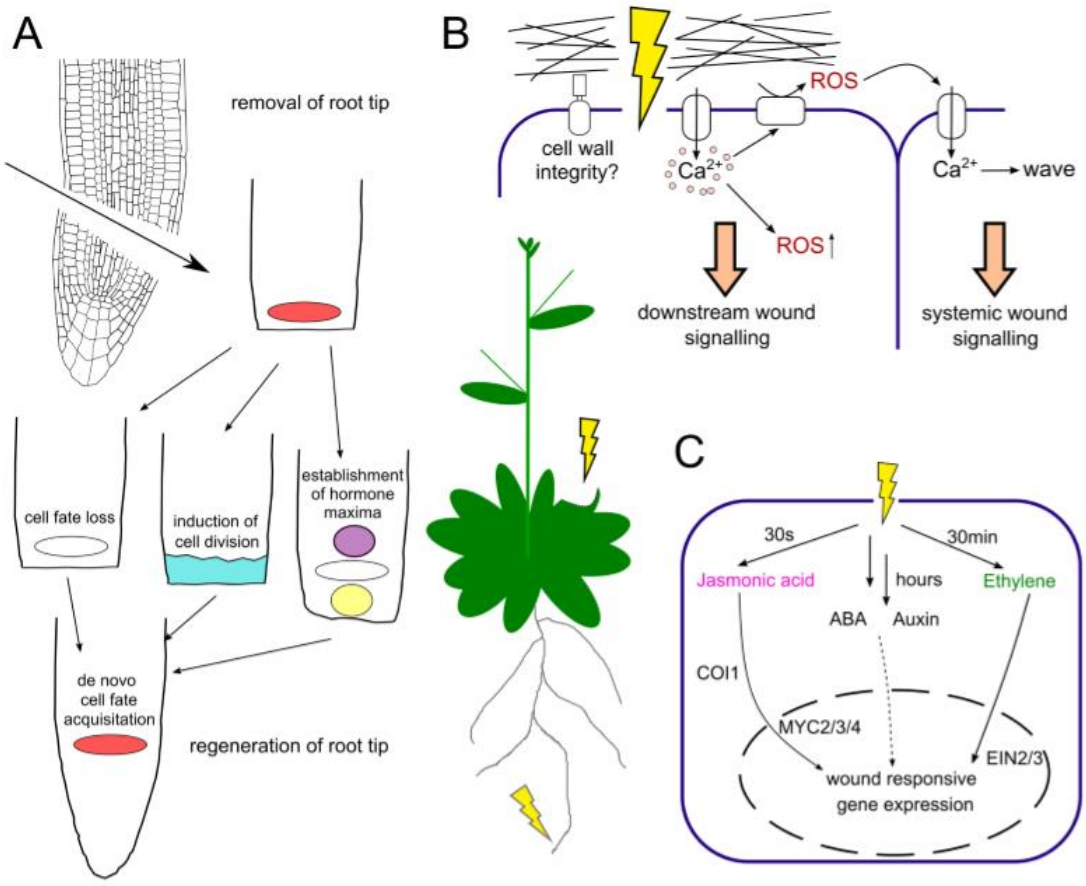


**Figure 1: Wounding triggers primary wounding signals, phytohormone signalling and complex regeneration responses**

**(A)** Cutting off the root tip including the stem cell niche leads to a complete rebuilding of the missing structures by the following processes: (i) Dedifferentiation in cells close to the wound and adoption of embryonic/stem cell programs (5,7); (ii) Increase in division rates in cells close to the wound and switch in division planes (7); (iii) Establishment of new accumulation zones for the phytohormones cytokinin (purple) and auxin (yellow) to define the new stem cell niche (5); (iv) Finally, *de novo* establishment of correct cell types in newly generated cells to restore the original tissue pattern (4,5) .

**(B)** Wounding on a cellular level means the disruption of the cellular envelope - cell wall (black) and plasma membrane (blue). Cell wall integrity sensing is presumably involved in wound signalling (20, 21). Wound signalling quickly manifests as a $Ca^{2+}$ wave which spreads through neighbouring tissues (11, 12). The $Ca^{2+}$ wave relates to the production of ROS in the apoplast and causes itself an oxidative burst inside and outside the cells (13, 14, 15). Together, $Ca^{2+}$ and ROS trigger multiple downstream signalling events at the wound site and in distal organs to induce immune responses (12, 14, 20).

**(C)** Wounding induces production of various phytohormones with different dynamics. Jasmonate accumulation starts seconds after the wounding (50) and is perceived by CORONATINE INSENSITIVE1 (COI1) (51). This leads to the activation of MYC2/3/4 transcription factors regulating downstream genes (52). Ethylene accumulates 30min after wounding by an increased activity of its biosynthesis genes (24) and acts through ETHYLENE-INSENSITIVE PROTEIN 2/3 (EIN2/3) transcription factors (53, 20). ABA accumulation after wounding occurs after several hours in desiccated tissues and presumably functions in maintaining healthy plant physiology rather than immune responses (26). Wounding induces changes in auxin accumulation and signalling after removal of the whole root tip; this involves induction of YUCCA biosynthetic components that play an important role in rebuilding destroyed structures (25, 46).

---

Unsurprisingly, phytohormones, as universal endogenous signals, are induced with different dynamics after attack to contribute to the balance of growth and immunity/defence (22). Historically, by extracting organic compounds from wound sites, the signalling compound traumatin was isolated which accelerates the wound healing when exogenously applied (3). Similarly, wounding induces jasmonic acid (JA) (23), ethylene (Et) (24) and less directly, auxin (25) and abscisic acid (ABA) (Fig. 1C) (26, 27). While the biosynthetic pathways for most of these phytohormones are known, the exact production sites and the signalling mechanism underlying their activation, have not been investigated.

## Wounding by targeted cell elimination

Recent reports have made use of targeted elimination of a single cell or small group of cells coupled with state-of-the-art live imaging allowing for more precise characterization of the wound responses and regeneration processes.

### *Laser ablation technique*

In the 90s, the UV laser ablation technique was introduced allowing for elimination of single cells. Originally, this was used to study cell-to-cell signalling and patterning mechanisms rather than as a tool to induce wounding and study regeneration. This technique has the advantage of removing a cell with spatial and temporal preciseness (28, 29), in contrast to genetic (30) or chemical ablations (31, 32). Different types of lasers on different imaging setups (28, 29, 31, 33, 34) have been used with propidium iodide staining which stains cell

walls, allow identification of dead cells and also pre-sensitises cells for ablation (35). This allowed the first live observation of wound healing responses in real time and *in situ* (32).

*Cellular responses during regeneration*

The root meristem is a tissue where cells are constantly in the cell cycle to proliferate for a sustained growth. Cell elimination dramatically accelerates division rates of adjacent cells predominately at its inner adjacent side, as the time required for one division is reduced from 18 to 5-12 hours (depending on the cell type) (Fig. 2C). These "restorative divisions" involve a change in division planes from anticlinal (perpendicular to the growth axis) to periclinal (parallel to the growth axis) allowing for efficient replacement of the dead cells in the wound from the inside. Earlier studies showed that also in the stem cell niche, ablated cells are replaced by irregular divisions of adjacent cells (28). Outside of the stem cell niche, in differentiating cells, stem cell programs aid the regeneration process as seen by the re-activation of the endodermis/cortex (SHR/SCR and CYCD6;1) or the lateral root cap/epidermis (FEZ and SMB) stem cell regulators (Fig. 2C) (32). Additionally, PLETHORA transcription regulators expressed in a decreasing gradient from the stem cell niche and associated with root stem cell activity (36) appear to endow cells with the competence to induce restorative divisions outside of the stem cell niche (32).

Already the earlier ablation experiments suggested that cells in the root adopt their fate depending on the tissue context (28, 29). This is manifested dramatically during restorative divisions of any cell type. After the division plane switch, the inner daughter cell, which stays in the cell file it originated from, retains its identity. Remarkably, the outer daughter cell rapidly adopts the cell identity of the eliminated cell, which it replaces (Fig. 2C) (32).

The restorative divisions, which require accelerated cell cycle progression, division plane switch and finally cell fate change of the daughter cells, appear to be very robust and likely dependent on multiple redundant stem cell program-dependent and –independent mechanisms. However, what signal triggers these divisions and what mechanism restricts them to cells only directly adjacent to the wound, remains elusive.

*Primary wound signalling*

Similar to herbivore attacks, wounding of single cells in the root meristem induces $Ca^{2+}$ waves in the surrounding tissue. However, harmed cells exhibit a greater $Ca^{2+}$ influx with an

increased duration which is translated by a novel $Ca^{2+}$-responsive protease, metacaspase MC4, into the rapid processing and release of Pep1 peptide. Eventually, the secreted Pep1 reaches the surface of neighbouring cells and starts signalling through PEPR1/2 receptors to activate defence-related genes (Fig. 2B) (34).

Ablation of cells outside the root meristem (in the elongation zone) also triggers a $Ca^{2+}$ wave and an increase in ROS accumulation in cells close to the wound site. Similar to previous studies (13), this $Ca^{2+}$ wave and its propagation partly depend on enzymatic ROS production in the apoplast (37). These phenomena also coincide with a membrane depolarization close to the ablation site which probably comes from changed ion fluxes, like $Ca^{2+}$and other available ions (Fig. 2A) (37).

Ablation experiments in the shoot apical meristem induce similar $Ca^{2+}$ waves, which are required for the repolarisation of the auxin efflux transporter PIN1 away from the wounded tissues (38), consistent with previously established importance of $Ca^{2+}$ signalling for PIN polarity in roots (39). Additionally, microtubules rearrange in the same cells after ablation as a consequence of a changed mechanical stresses, but this seems to be independent of the $Ca^{2+}$ waves, indicating more complex and yet unknown mechanosensitive signalling mechanisms responsive to wounding (38).

*Involvement of phytohormones*

As expected, multiple phytohormones are involved in coordinating regenerative processes following wounding but their exact role and interactions are far from clarified. Cell ablation or infection with root-invading nematodes, which can lead to the specific removal of single cells in the root, leads to the increase of the transcriptional ethylene response marker ACS6 as early as 3 hours after ablation. Defence against these invaders depends on ethylene signalling through EIN2 (37, 40) and this triggering of the ethylene signalling partly depends on the $Ca^{2+}$ wave and ROS production by apoplast-localised oxidases. Overall, these observations reveal an important role of ethylene in the root immune and wound response (Fig. 2A) (37).

Jasmonates (JA), phytohormones typically associated with plant immunity, are induced around wounds specifically in the central root meristem as early as 30s after the ablation (Fig. 2D). Similarly, nematode infestation or root growing through rough soil inducs JA (41). Pending evidence to the contrary, it seems JA response is not induced in root tissues other than the root meristem (37).

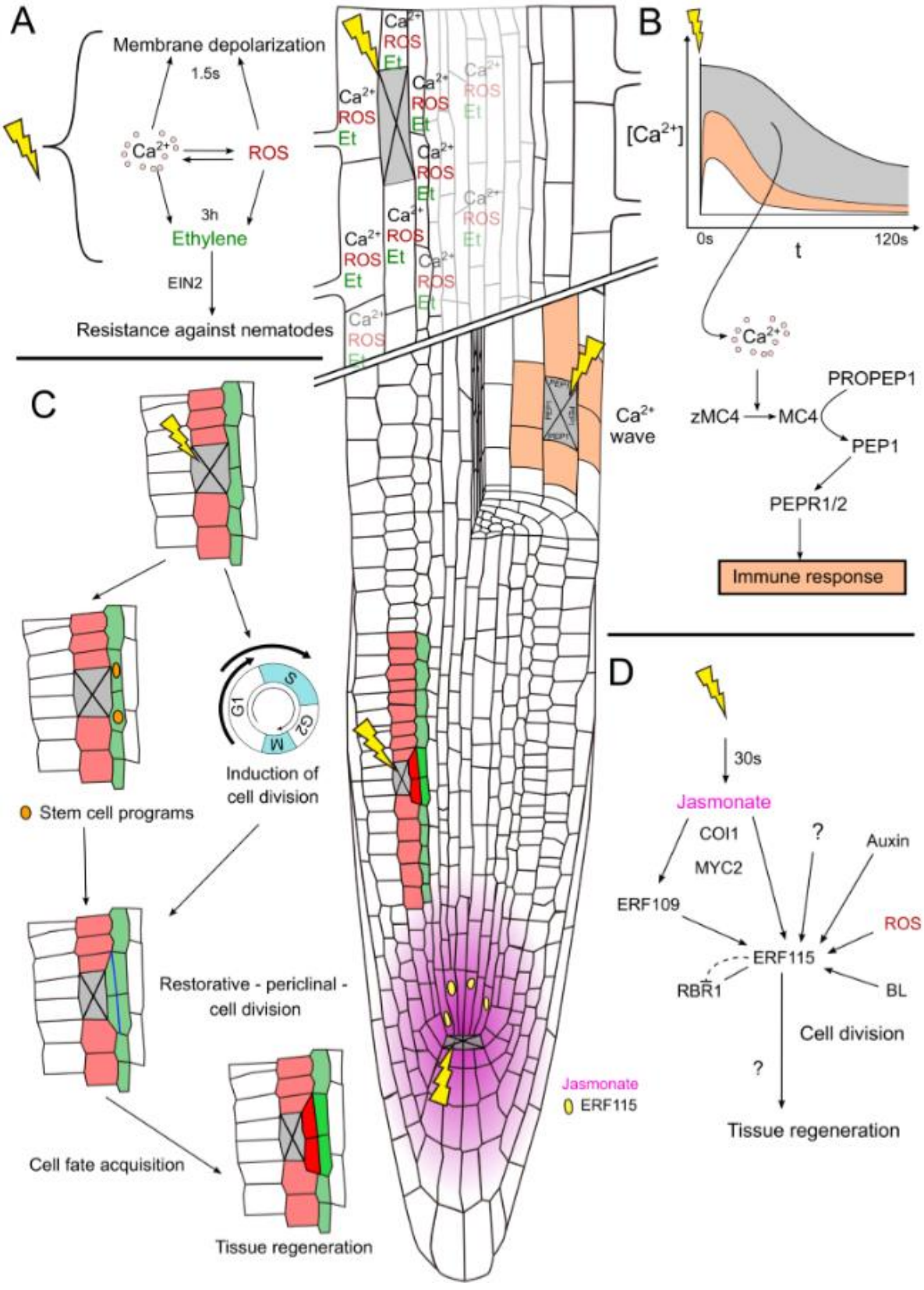


**Figure 2. Single cell ablation in the Arabidopsis root meristem triggers multiple local and regional wounding responses.**

**(A)** Ablation of cortex cells in the elongation zone triggers the induction of $Ca^{2+}$, ROS, ethylene and

membrane depolarisation. The increase in $Ca^{2+}$ influx after ablation is dependent on ROS production in the apoplast by RBOH enzymes and allows the fast change in membrane polarisation (1.5s after ablation). Additionally, it induces an accumulation of ROS around the wound that occurs ~6min after the ablation. Both, $Ca^{2+}$ influx and ROS production contribute to the ethylene signalling induction by an increased ACC SYNTHASE 6 (ACS6) expression starting 3 hours after ablation. Eventually, ethylene signalling via EIN2 increases the resistance against nematode infection (37)

**(B)** Laser ablation of epidermis cells in the transition zone triggers a $Ca^{2+}$ influx that spreads throughout the adjacent tissue but results in different amplitudes depending on the distance from the harmed cell. Harmed cells (grey) exhibit a stronger $Ca^{2+}$ influx than those directly adjacent to the eliminated cells (orange) and cells further away (white). Strong influx and complete destruction of membrane integrity activates METACASPASE4 (MC4) from inactive zMC4, which cleaves the PRECURSOR OF PEP1 (PROPEP1) into Pep1. By this, it becomes translocated from the vacuolar membrane to the cytosol to be perceived by the PEPR1 and PEPR2 receptors at the cell surface of neighbouring (orange) cells (34).

**(C)** Ablation in the root meristem triggers restorative divisions to replace the eliminated cells. These divisions happen predominately in the inner adjacent cells. They are induced by the activation of stem cell programs (orange nuclei; here: SHR – CYCD6;1) and an accelerated progression through the cell cycle. They include the switch of the division plane from anticlinal to periclinal, and the newly generated outer daughter cells adopt the cell fate of the eliminated cells to eventually regenerate the disrupted tissue pattern (32).

**(D)** Ablations in the stem cell niche trigger a jasmonate induction within 30s which is perceived by COI1 to activate MYC2, a JA-dependent transcription factor. MYC2 binds to the promoter of ERF115 to enhance its expression around the wound site (41). ERF115 is also activated by its JA/MYC2-dependent homologue ERF109 (41) and by downstream signalling of auxin (41), ROS (49) and brassinosteroids (BL) (47, 48). In ablations outside the stem cell niche, ERF115 expression is confined to cells directly adjacent to the killed cell (31, 32). ERF115 can bind to RETINOBLASTOMA-RELATED1 (RBR1) and inhibit its activity to regulate the division rate in the quiescent centre and the stem cell niche (41). Few downstream targets of ERF115 have been identified. One of them, PSK5, might be involved in the acceleration of the cell cycle progression (47). Eventually, ERF115 transcription factor activity contributes greatly to tissue regeneration after single cell ablation as well as whole root tip removal (31, 32, 41).

Yellow thunderbolts indicate UV laser ablation.

---

Auxin has been implicated among many other processes, also in regulation of division plane orientation, cell fate (re)specification (42) and for the maintenance of the stem cell

niche in the root meristem centre (43). Removal of the root tip triggers a strong auxin accumulation above the ablated cells, presumably due to a disruption of the intercellular auxin flow, to induce replacement of the meristem centre (44). Chilling stress induces natural death in root tip cells, which thereby block auxin transport anatomically. The resulting auxin accumulation helps maintaining the meristem centre during the stress (45). Increased auxin biosynthesis, on the other hand, occurs in wounded leaves (25) and root stumps after meristem removal (46) and is crucial for the efficient tissue re-establishment. However, it remains unknown how wound-responsive auxin transport, biosynthesis or signalling play a role in local regenerative processes.

*Downstream transcriptional regulations*

Besides the above mentioned glimpses into wound-triggered signalling processes, little is known about the downstream mechanisms leading to regeneration. One of the few identified components is the ETHYLENE RESPONSE FACTOR 115 (ERF115), a transcription factor required for the efficient initiation of restorative divisions (31, 32), and its close homologue and upstream regulator ERF109 (41). Without wounding, the ERF115 expression domain is usually restricted to the rarely occurring cell divisions in the quiescent centre, where it is controlled by brassinosteroids (47, 48), but it can be slightly increased by exogenous application of ROS, auxin and JA (41, 49). In some cell types after wounding, ERF115 becomes upregulated in a JA-dependent manner during restorative divisions in cells directly adjacent to the wound (Fig. 2D) (41, 31). It remains a mystery how such spatially restricted ERF115 induction is achieved by rather broadly spreading signals, exactly which factors are involved in cell types where ERF115 is not induced and which downstream targets of ERF115 mediate the regeneration.

**Conclusions**

Several recent studies using the single cell ablation allowed identifying wound response processes at different levels: i.) local - cells directly adjacent to the wounds, ii.) regional - cell groups in close proximity, or iii.) systemic - the whole tissue in the same organ or in completely different parts of the plants. Comparable responses after cell ablation, nematode infestation or naturally occurring wounding suggest that laser-assisted cell elimination can be used to study mechanism of wound healing.

Multiple signals have been identified to be involved in the response to wounding, but the nature of the primary wound signal which activates the adjacent cells remains completely

elusive, along with most of the downstream regeneration mechanisms. Further studies, building up on these initial findings and combining laser-assisted cell elimination with live imaging, forward genetic screens and single cell transcriptomics will allow us to get detailed molecular insights of what is happening at the local, regional and systemic levels and how different signalling mechanisms cooperatively contribute towards wound healing. These studies will reveal not only mechanism of tissue regeneration but also help us to understand the general mechanisms of positional information-based tissue patterning.

**Acknowledgements**

Research in the J.F. laboratory is funded by the European Union's Horizon2020 program (ERC grant agreement n° 742985).

**References**

1. Molisch, H. (1888). Zur Kenntniss der Thyllen, nebst Beobachtungen über Wundheilung in der Pflanze. éditeur non identifié.
2. Hartsema, A. (1926). Anatomische und experimentelle Untersuchungen über das Auftreten von Neubildungen an Blättern von Begonia Rex.
3. Bloch, R. (1941). Wound Healing in Higher plants. Botanical Review, 7(2), 110-146.
4. Sena, G., Wang, X., Liu, H.-Y., Hofhuis, H., & Birnbaum, K. (2009, 2 28). Organ regeneration does not require a functional stem cell niche in plants. Nature, 457(7233), 1150-1153.
5. Efroni, I., Mello, A., Nawy, T., Ip, P.-L., Rahni, R., DelRose, N., . . . Birnbaum, K. (2016, 6 16). Root Regeneration Triggers an Embryo-like Sequence Guided by Hormonal Interactions. Cell, 165(7), 1721-1733.
6. Hush, J., Hawes, C., & Overall, R. (1990). Interphase microtubule re-orientation predicts a new cell polarity in wounded pea roots. Journal of Cell Science, 96(1).
7. Barlow, P. (1974). Regeneration of the cap of primary roots of Zea mays. New phytologist, 73(5), 937-954.
8. León, J., Rojo, E., & Sánchez-Serrano, J. (2001, 1 1). Wound signalling in plants. Journal of Experimental Botany, 52(354), 1-9.
9. Heil, M., & Land, W. (2014, 10 31). Danger signals - damaged-self recognition across the tree of life. Frontiers in Plant Science, 5, 578.
10. Henry, G., Thonart, P., & Ongena, M. (2012). PAMPs, MAMPs, DAMPs and others: an update on the diversity of plant immunity elicitors. BASE.

11. Knight, M., Read, N., Campbell, A., & Trewavas, A. (1993, 4). Imaging calcium dynamics in living plants using semi-synthetic recombinant aequorins. The Journal of cell biology, 121(1), 83-90.

12. Toyota, M., Spencer, D., Sawai-Toyota, S., Jiaqi, W., Zhang, T., Koo, A., . . . Gilroy, S. (2018, 9 14). Glutamate triggers long-distance, calcium-based plant defense signaling. Science (New York, N.Y.), 361(6407), 1112-1115.

13. Mittler, R., Vanderauwera, S., Suzuki, N., Miller, G., Tognetti, V., Vandepoele, K., . . . Van Breusegem, F. (2011, 6). ROS signaling: the new wave? Trends in Plant Science, 16(6), 300-309.

14. Suzuki, N., & Mittler, R. (2012, 12 15). Reactive oxygen species-dependent wound responses in animals and plants. Free Radical Biology and Medicine, 53(12), 2269-2276.

15. Kobayashi, M., Ohura, I., Kawakita, K., Yokota, N., Fujiwara, M., Shimamoto, K., . . . Yoshioka, H. (2007, 3 9). Calcium-Dependent Protein Kinases Regulate the Production of Reactive Oxygen Species by Potato NADPH Oxidase. THE PLANT CELL ONLINE, 19(3), 1065-1080.

16. Roberts, K. (1992). Potential awareness of plants. Nature, 360(6399), 14.

17. Huffaker, A., Pearce, G., & Ryan, C. (2006, 6 27). An endogenous peptide signal in Arabidopsis activates components of the innate immune response. Proceedings of the National Academy of Sciences, 103(26), 10098-10103.

18. Krol, E., Mentzel, T., Chinchilla, D., Boller, T., Felix, G., Kemmerling, B., . . . Hedrich, R. (2010, 4 30). Perception of the Arabidopsis danger signal peptide 1 involves the pattern recognition receptor AtPEPR1 and its close homologue AtPEPR2. The Journal of biological chemistry, 285(18), 13471-9.

19. Bartels, S., Lori, M., Mbengue, M., van Verk, M., Klauser, D., Hander, T., . . . Boller, T. (2013, 12 1). The family of Peps and their precursors in Arabidopsis: differential expression and localization but similar induction of pattern-triggered immune responses. Journal of Experimental Botany, 64(17), 5309-5321.

20. Savatin, D., Gramegna, G., Modesti, V., & Cervone, F. (2014). Wounding in the plant tissue: the defense of a dangerous passage. Frontiers in plant science, 5, 470.

21. Nühse, T. (2012, 12 11). Cell wall integrity signaling and innate immunity in plants. Frontiers in Plant Science, 3, 280.

22. Huot, B., Yao, J., Montgomery, B., & He, S. (2014, 8). Growth-defense tradeoffs in plants: a balancing act to optimize fitness. Molecular plant, 7(8), 1267-1287.

23. Creelman, R. A., Tierney, M. L., & Mullet, J. E. (1992). Jasmonic acid/methyl jasmonate accumulate in wounded soybean hypocotyls and modulate wound gene expression. Proceedings of the National Academy of Sciences, 89(11), 4938-4941.

24. Boller, T., & Kende, H. (1980, 7). Regulation of wound ethylene synthesis in plants. Nature, 286(5770), 259-260.

25. Chen, L., Tong, J., Xiao, L., Ruan, Y., Liu, J., Zeng, M., ... & Xu, L. (2016). YUCCA-mediated auxin biogenesis is required for cell fate transition occurring during de novo root organogenesis in Arabidopsis. Journal of experimental botany, 67(14), 4273-4284.

26. Birkenmeier, G., & Ryan, C. (1998, 6 1). Wound Signaling in Tomato Plants. Plant Physiology, 117(2), 687-693.

27. Johnson, S. N., Erb, M., & Hartley, S. E. (2016). Roots under attack: contrasting plant responses to below-and aboveground insect herbivory. New Phytologist, 210(2), 413-418.

28. van den Berg, C., Willemsen, V., Hage, W., Weisbeek, P., & Scheres, B. (1995, 11). Cell fate in the Arabidopsis root meristem determined by directional signalling. Nature, 378(6552), 62-65.

29. Berger, F., Haseloff, J., Schiefelbein, J., & Dolan, L. (1998, 4 9). Positional information in root epidermis is defined during embryogenesis and acts in domains with strict boundaries. Current Biology, 8(8), 421-430.

30. Weijers, D., Hamburg, J.-P., Rijn, E., Hooykaas, P., & Offringa, R. (2003, 12 1). Diphtheria Toxin-Mediated Cell Ablation Reveals Interregional Communication during Arabidopsis Seed Development. Plant Physiology, 133(4), 1882-1892.

31. Heyman, J., Cools, T., Canher, B., Shavialenka, S., Traas, J., Vercauteren, I., . . . De Veylder, L. (2016, 11 31). The heterodimeric transcription factor complex ERF115–PAT1 grants regeneration competence. Nature Plants, 2(11), 16165.

32. Marhava, P., Hoermayer, L., Yoshida, S., Marhavý, P., Benková, E., & Friml, J. (2019). Re-activation of Stem Cell Pathways for Pattern Restoration in Plant Wound Healing. Cell, 177(4), 957-969.

33. Marhavý, P., Montesinos, J., Abuzeineh, A., Van Damme, D., Vermeer, J., Duclercq, J., . . . Benková, E. (2016, 2 15). Targeted cell elimination reveals an auxin-guided biphasic mode of lateral root initiation. Genes & Development, 30(4), 471-483.

34. Hander, T., Fernández-Fernández, Á., Kumpf, R., Willems, P., Schatowitz, H., Rombaut, D., . . . Stael, S. (2019, 3 22). Damage on plants activates Ca2+-dependent metacaspases for release of immunomodulatory peptides. Science (New York, N.Y.), 363(6433), eaar7486.

35. Lo Schiavo, F., Last, R., Morelli, G., & Raikhel, N. (Eds.). (1998). Cellular Integration of Signalling Pathways in Plant Development. Berlin, Heidelberg: Springer Berlin Heidelberg.

36. Galinha, C., Hofhuis, H., Luijten, M., Willemsen, V., Blilou, I., Heidstra, R., & Scheres, B. (2007, 10 25). PLETHORA proteins as dose-dependent master regulators of Arabidopsis root development. Nature, 449(7165), 1053-1057.

37. Marhavý, P., Kurenda, A., Siddique, S., Tendon, V. D., Zhou, F., Holbein, J., ... & Geldner, N. (2019). Single-cell damage elicits regional, nematode-restricting ethylene responses in roots. The EMBO journal, 38(10), e100972.

38. Li, T., Yan, A., Bhatia, N., Altinok, A., Afik, E., Durand-Smet, P., ... & Meyerowitz, E. M. (2019). Calcium signals are necessary to establish auxin transporter polarity in a plant stem cell niche. Nature communications, 10(1), 726.

39. Zhang, J., Vanneste, S., Brewer, P. B., Michniewicz, M., Grones, P., Kleine-Vehn, J., ... & Hoyerová, K. (2011). Inositol trisphosphate-induced Ca2+ signaling modulates auxin transport and PIN polarity. Developmental cell, 20(6), 855-866.

40. Bisson, M. M., Bleckmann, A., Allekotte, S., & Groth, G. (2009). EIN2, the central regulator of ethylene signalling, is localized at the ER membrane where it interacts with the ethylene receptor ETR1. Biochemical Journal, 424(1), 1-6.

41. Zhou, W., Lozano-Torres, J., Blilou, I., Zhang, X., Zhai, Q., Smant, G., . . . Scheres, B. (2019, 5 2). A Jasmonate Signaling Network Activates Root Stem Cells and Promotes Regeneration. Cell, 177(4), 942-956.e14.

42. Vanneste, S., & Friml, J. (2009). Auxin: a trigger for change in plant development. Cell, 136(6), 1005-1016.

43. Ding, Z., & Friml, J. (2010). Auxin regulates distal stem cell differentiation in Arabidopsis roots. Proceedings of the National Academy of Sciences, 107(26), 12046-12051.

44. Xu, J., Hofhuis, H., Heidstra, R., Sauer, M., Friml, J., & Scheres, B. (2006). A molecular framework for plant regeneration. Science, 311(5759), 385-388.

45. Hong, J. H., Savina, M., Du, J., Devendran, A., Ramakanth, K. K., Tian, X., ... & Xu, J. (2017). A sacrifice-for-survival mechanism protects root stem cell niche from chilling stress. Cell, 170(1), 102-113.

46. Xu, D., Miao, J., Yumoto, E., Yokota, T., Asahina, M., & Watahiki, M. (2017, 10 1). YUCCA9-Mediated Auxin Biosynthesis and Polar Auxin Transport Synergistically Regulate Regeneration of Root Systems Following Root Cutting. Plant and Cell Physiology, 58(10), 1710-1723.

47. Heyman, J., Cools, T., Vandenbussche, F., Heyndrickx, K., Leene, J., Vercauteren, I., . . . Veylder, L. (2013, 11 15). ERF115 Controls Root Quiescent Center Cell Division and Stem Cell Replenishment. Science, 342(6160), 860-863.

48. Lee, H.-S., Kim, Y., Pham, G., Kim, J., Song, J.-H., Lee, Y., . . . Kim, S.-H. (2015, 8). Brassinazole resistant 1 (BZR1)-dependent brassinosteroid signalling pathway leads to ectopic activation of quiescent cell division and suppresses columella stem cell differentiation. Journal of experimental botany, 66(15), 4835-49.

49. Kong, X., Tian, H., Yu, Q., Zhang, F., Wang, R., Gao, S., . . . Ding, Z. (2018, 1 30). PHB3 Maintains Root Stem Cell Niche Identity through ROS-Responsive AP2/ERF Transcription Factors in Arabidopsis. Cell Reports, 22(5), 1350-1363.

50. Glauser, G., Dubugnon, L., Mousavi, S. A., Rudaz, S., Wolfender, J. L., & Farmer, E. E. (2009). Velocity estimates for signal propagation leading to systemic jasmonic acid accumulation in wounded Arabidopsis. Journal of Biological Chemistry, 284(50), 34506-34513.

51. Xie, D. X., Feys, B. F., James, S., Nieto-Rostro, M., & Turner, J. G. (1998). COI1: an Arabidopsis gene required for jasmonate-regulated defense and fertility. Science, 280(5366), 1091-1094.

52. Kazan, K., & Manners, J. M. (2013). MYC2: the master in action. Molecular plant, 6(3), 686-703.

53. Alonso, J. M., Hirayama, T., Roman, G., Nourizadeh, S., & Ecker, J. R. (1999). EIN2, a bifunctional transducer of ethylene and stress responses in Arabidopsis. Science, 284(5423), 2148-2152.

# Chapter 2

## Re-activation of stem cell pathways for pattern restoration in plant wound healing

Petra Marhava[a,b*], Lukas Hoermayer [a*], Saiko Yoshida[a,c*], Peter Marhavý[a,b], Eva Benková[a] and Jiří Friml[a,1,§]

[a]Institute of Science and Technology Austria, 3400 Klosterneuburg, Austria

[b]Current address: University of Lausanne, DBMV, CH-1015 Lausanne, Switzerland

[c]Current address: Max Planck Institute for Plant Breeding Research, 50829 Carl-von-Linné-Weg 10, Cologne, Germany

[*]These authors contributed equally

[1]Lead contact

[§]Correspondence

Published in

Cell. 2019 May 2; 177(4): 957–969.e13.

**Summary**

Patterning in plants relies on oriented cell divisions and acquisition of specific cell identities. Plants regularly endure wounds caused by abiotic or biotic environmental stimuli and have developed extraordinary abilities to restore their tissues after injuries. Here we provide insight into a mechanism of restorative patterning that repairs tissues after wounding. Laser-assisted elimination of different cells in *Arabidopsis* root combined with live imaging tracking during vertical growth allowed analysis of the regeneration processes *in vivo*. Specifically, the cells adjacent to the inner side of the injury re-activated their stem cell transcriptional programs. They accelerated their progression through cell cycle, coordinately changed the cell division orientation, and ultimately acquired *de novo* the correct cell fates to replace missing cells. These observations highlight existence of unknown intercellular positional signaling and demonstrate the capability of specified cells to re-acquire stem cell programs as a crucial part of the plant-specific mechanism of wound healing.

## Introduction

Multicellular animals and plants emerged well after the split of these two lineages during evolution and thus these major eukaryotic groups utilize largely independent mechanisms to deal with challenges of multicellularity such as cell-to-cell communication, development coordination and tissue patterning. Unlike in animals, plant cells are encapsulated within rigid cell walls and thus cannot use cell migration during tissue patterning or wound healing. Therefore, plants rely mainly on strictly controlled orientation of cell divisions followed by the acquisition of specific cell fates (Rasmussen and Bellinger, 2018). Despite the core cell cycle machinery is conserved between animals and plants (Harashima et al., 2013), signals and mechanisms regulating the transition of cell cycle stages and control of the cell division plane during patterning are presumably plant-specific. Multiple molecular components and mechanisms of cell fate specification have been elucidated in plants (Benfey et al., 1993; De Rybel et al., 2013) but little is known about how these individual mechanisms are activated and integrated during the concerted tissue patterning processes.

Plants as sessile organisms have to regularly endure wounds caused by abiotic or biotic environmental factors; therefore, they evolved a remarkable ability to regenerate wounded tissues e.g. reconnecting interrupted vascular strands (Mazur et al., 2016) or regenerating whole complex structures such as the root apical meristem (Efroni et al., 2016; Sena et al., 2009). It has been known for almost a century that harmed plant tissues activate cell division in adjacent cells and switch division planes to fill the wound with new daughter cells (Hartsema, 1926; Hush et al., 1990; Sinnott and Bloch, 1941). Later, when *Arabidopsis* root has been established as essential model for elucidation of patterning mechanisms in plants (Benfey et al., 1993; Dolan et al., 1993), more specific, microsurgical, laser-assisted cell eliminations allowed the observation of cell re-specification to regenerate lost cells, in particular in the area of the root stem cell niche (Van den Berg et al., 1995; Xu et al., 2006). Similar approaches also demonstrated that constant positional signaling is essential for maintaining the root meristem pattern during continuous development (Berger et al., 1998; Kidner et al., 2000). However, the phenomenon of wound healing and restoration of correct tissue pattern after injury has not been addressed specifically in *Arabidopsi*s roots. In particular, how the tissue re-acquires a correct pattern of cell types and what positional signaling mechanisms contribute to this, remain unknown.

Here, we established a method of well-defined wounding by targeted cell elimination of individual cells or cell groups in *Arabidopsis* root meristem and combined this with extended

live imaging at the vertical stage microscope. This allowed analysis of the phenomenon of restorative patterning during wound healing. Restorative patterning involves activation of respective stem cell pathways and manifests in an immediate induction of cell division, controlled reorientation of division planes and acquisition of specific, correct cell fates. These observations provide insights into plant-specific wound healing and reveal previously unappreciated aspects of mechanisms underlying cell division orientation, cell fate acquisition and positional signaling as well as coordination of these processes during tissue patterning.

## Results

### Restorative cell divisions induced by local wounding

The root apex of *Arabidopsis thaliana* proved to be a great model for studying tissue patterning in plants. A small group of cells with stem cell-like properties surrounds the so-called quiescent center (QC) and generates all different cell types that form the root (Berger et al., 1998; De Rybel et al., 2016; Kidner et al., 2000; Kumpf and Nowack, 2015; Scheres et al., 2002). Once the different cell types are established by the stereotypic, asymmetric cell divisions, the daughter cells undergo only proliferative, anticlinal (perpendicular to the root axis) divisions that propagate the cell files on their way out of the meristem (Figures 1A and 1C).

We adapted the targeted UV-laser ablation technique (Marhavý et al., 2016; Xu et al., 2006) to eliminate specifically individual cells or cell groups in different cell layers of the root tip. 3D reconstruction of the area around the ablated cell confirmed an ablation of single cells with intact surrounding tissues (Figure 1B; Movie S1).

The cell ablation led invariantly to a switch from anticlinal to periclinal (parallel to the root axis) division typically of the inner (very rarely also outer) adjacent cell leading to eventual replacement of the eliminated cell (Figures 1D-1G, Table S1 and Movie S2). This capacity to initiate cell division was observed in all major cell types of the root meristem, no matter in which layer the ablation was performed: Ablation of a young lateral root cap (LRC) cell induced periclinal divisions in adjacent epidermis cells (Figure 1D); ablation of epidermis induced division of adjacent cortex (Figure 1E); ablation of a cortex cell led to the endodermis division (Figures 1F, S1A, S1B and Movie S2) and ablation of endodermis induced pericycle division (Figure 1G). Periclinal cell divisions also occurred when larger injuries of two or three neighboring cells of different cell layers were ablated, always leading to the periclinal division of the first intact cell at the inner side of the eliminated cells (Figures S1C-S1F). In this case,

the inner adjacent cells continued to divide periclinally until all dead cells were replaced (Figure S1G). To eliminate cells by a different method, we used treatment with hydroxyurea (HU), an inhibitor of ribonucleotide reductase, which inhibits DNA replication and induces cell death (Cools et al., 2011). We observed random cell deaths in cortex and endodermis and all these events led to the periclinal divisions of the inner adjacent cells (Figures S1K-S1M), as seen in the case of laser-assisted cell elimination. Naturally occurring wounds occasionally observed even in laboratory growth conditions induced similar periclinal divisions in inner adjacent cells (Figure S1N).

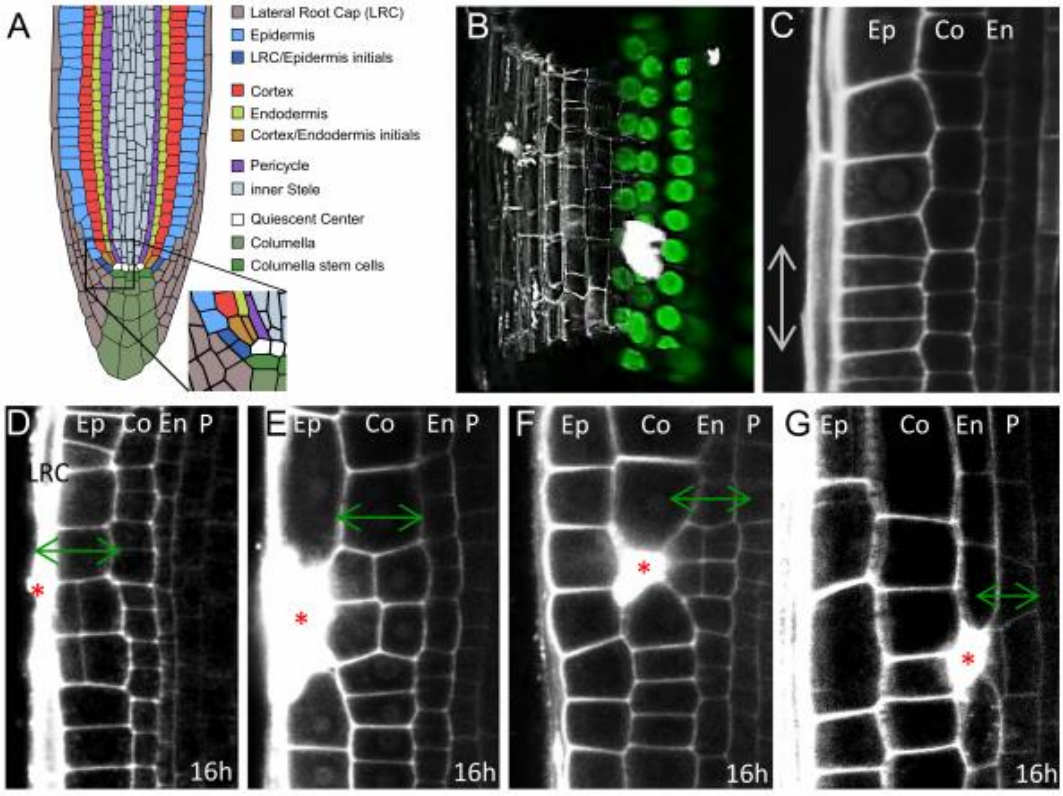


**Figure 1. Ablation triggers restorative cell divisions in inner adjacent cells.**

**(A)** Cell types in the *Arabidopsis* root meristem. Inset shows magnification of stem cell niche.

**(B)** 3D reconstruction of a single ablated endodermal cell in *SCR::SCR-YFP* root just after ablation. Propidium iodide (PI) stains cell walls and is not permeant to living cells, therefore was used to identify the ablated cell and intact neighboring cells. Shortly after ablation, PI becomes over-saturated and thus can partly overlap also with neighboring non-ablated cells. Later, PI staining is more restricted to the collapsed eliminated cell (see Figure S1C-S1D).

**(C)** Anticlinal division of cells in root meristem (grey arrow).

**(D-G)** Periclinal divisions of the inner adjacent cells (green arrows) after ablation. Ablation in lateral root cap **(D)**, epidermis **(E)**, cortex **(F)** and endodermis **(G)**. Total number of ablations; n = 30-60 per cell type.

LRC: lateral root cap, Ep: epidermis, Co: cortex, En: endodermis, P: pericycle. Red asterisks: sites of ablation.

See also Figure S1

---

Moreover, when we ablated cells in the roots of dicots *Capsella rubella, Nicotiana benthamiana* and the monocot *Oryza sativa*, we observed the same phenomenon of wound-induced activation of periclinal cell division (Figures S1H-S1J). Genetics and marker lines analysis (Figure S7A-G) revealed that the injury-induced division do not require known regulators of periclinal cell division (*LHW*, *TMO5*, *LOG4, TCS*), mechanosensing (*feronia*, *theseus*, *mca1* and *mca2*, *mslΔ5*), or formation of the preprophase band (*trm6,7,8*) suggesting existence of unknown signaling mechanism conserved across higher plants.

These observations show that controlled, localized injuries in the root meristem of various species invariantly induce periclinal cell divisions in the inner adjacent cells. Notably, in the undisturbed situation, cells in these root regions undergo only anticlinal divisions, but the wound does not, typically, heal by this type of simple proliferation of the injured cell file but requires signaling to the different cell files adjacent to the inner side of the wound, possible activation of their division and the re-orientation of the division plane. As these processes ultimately lead to the regeneration of the wounded tissue, we termed this previously unappreciated phenomenon - the restorative cell division.

**Competence to initiate restorative cell divisions**

Our observations suggested that various root cell types have a capacity to initiate periclinal cell divisions in response to wounding also well outside of the stem cell niche, to where this type of divisions is normally confined. Thus, we tested systematically the competence of different cell types depending on their distance from the stem cell niche. We eliminated cells at different positions in the root apex (Figure 2A) and measured their position within the root apex by different means at 1 hour (h) after cell ablation along with the ability of inducing restorative cell divisions after 16 h (Figures 2B and S2A). We found that the capacity of cells to induce restorative divisions gradually decreases at different rates in various cell types, with the distance from the QC (Figure 2B). It appears that epidermis loses the responsiveness to cell ablation first (around 150 μm), followed by cortex (190 μm) and endodermis (220 μm), while

pericycle maintains its competence to initiate restorative divisions - consistent with its behavior as a “dormant meristem” throughout the whole root development (Marhavý et al., 2016).

This demonstrates that epidermis, cortex, endodermis and pericycle cells, all are competent to initiate restorative cell divisions well outside of the stem cell niche with their competence decreasing at different rates with the distance from it.

**PLETHORA regulators mediate competence for restorative cell divisions**

To get further insight into the mechanism underlying decreasing competence to initiate restorative cell divisions in more differentiated parts of the root meristem, we analyzed roots with shortened meristems. First, we analyzed *cre1 ahk2 ahk3* triple mutant of the cytokinin receptor genes and plants treated with cytokinin and brassinolide which all displayed reduced meristematic activity (Higuchi et al., 2004; Marhavý et al., 2011; Zhu et al., 2013). While the ability to induce restorative cell division in epidermis and cortex was significantly reduced, division rate in endodermis was only slightly decreased (Figures S2B- S2D). Thus, as expected, the regenerative competence in some cell types depends highly on meristematic activity.

Next, we analyzed the potential involvement of members of the PLETHORA (PLT) regulators of stem cell activities, which form an expression gradient decreasing with distance from the QC (Galinha et al., 2007, Figures S2F and S2G) thus correlating with the decrease of regenerative competence. Moreover, ectopic expression of PLT1 and PLT2 initiates a variety of phenotypes including increased meristem size and ectopic root formation throughout the plant (Aida et al., 2004; Galinha et al., 2007). Thus, we analyzed regeneration competence 12 h after ablation in the transition and elongation zones of the *35S::PLT2-GR* line. Ectopic PLT2 expression strongly rescued the capacity of cortex cells to induce restorative divisions after epidermis ablation even when they already left the division zone of the root tip (Figure 2C); also, in some cases, ablation of LRC cells at the end of the division zone induced periclinal or oblique divisions in epidermis (Figure S2E). Similarly, the cells of endodermis slightly regained the competence to divide periclinally following cortex ablations even outside of the division zone (Figure 2C). Notably, induction of PLT2 expression as short as 1 h prior ablation was sufficient to increase the rate of restorative divisions within (150-200 μm) and at the end of the division zone (200-230 μm) and even allowed cells that already left the division zone to induce restorative divisions (at 275-400 μm from 0% in WT to ~70% in *35S::PLT-GR;* Figure 2D).

In a reciprocal experiment, we analyzed *plt1* and *plt2* mutants and found that single mutants showed no reduction in periclinal division rates in epidermis but possessed increased

number of periclinal divisions in cortex (*plt1*) and endodermis (*plt2*). Notably, *plt1plt2* double mutant is strongly defective in restorative divisions in epidermis (Figure 2E and 2F).

Our results identified PLT transcription factors as being necessary and sufficient components of the root cell competence to initiate restorative division. Moreover, the regenerative competence depends on PLT expression levels and correlates with the PLT expression gradient in the root.

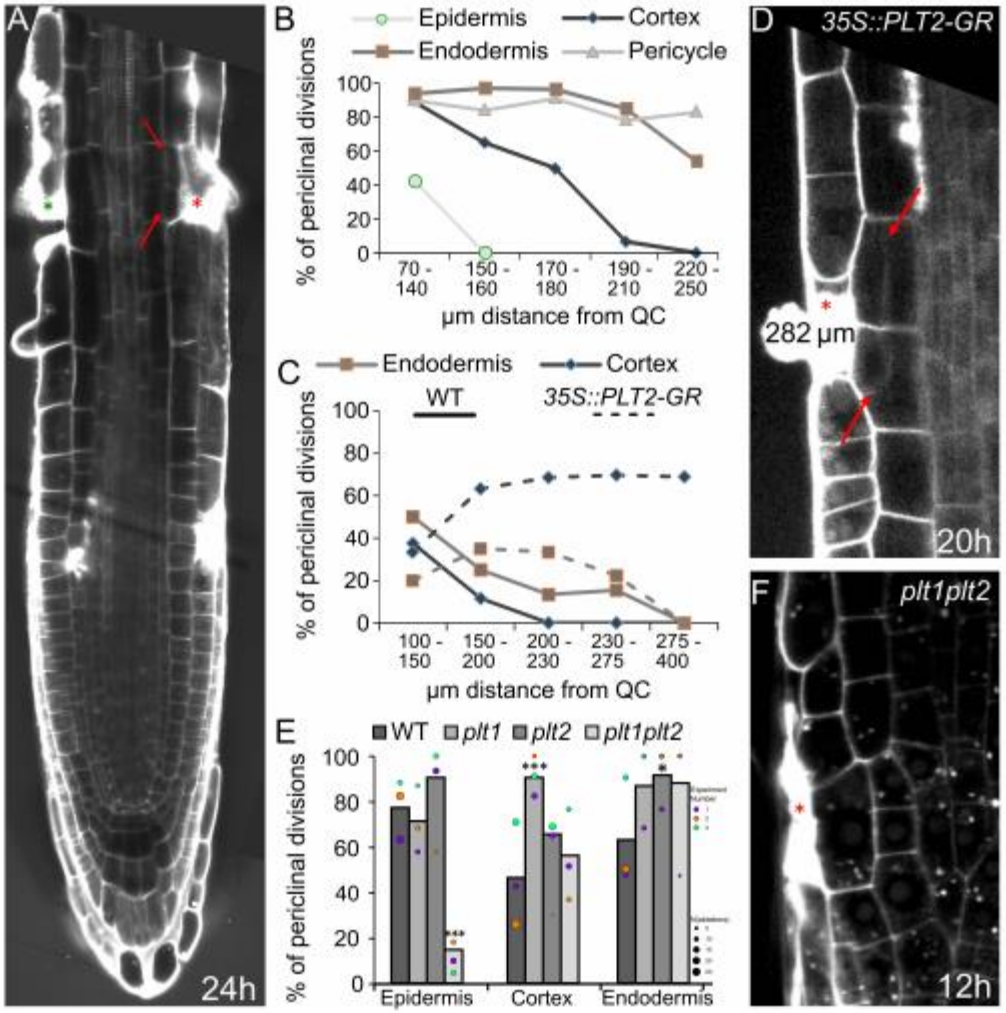


**Figure 2. Decreasing competence of restorative divisions correlates with PLT activity**

**(A)** Tile scan of a root 24 h after ablation of cortex and epidermis. While ablation of cortex cells (red asterisk) induced periclinal cell divisions in endodermis (red arrows), ablation of epidermis (green asterisk) did not induce periclinal division in cortex, which lost the competence to divide. In contrast, ablation of epidermis closer to the quiescent center induced the periclinal cortex cell divisions. Marked ablated cells moved from meristem into elongation zone during growth.

**(B)** Number of periclinal divisions decreases with distance from QC; as measured in various cell types after 16 h depending on distance from the QC at the time of ablation (µm). Total number of ablations; n = 15-50 for every 10 µm (70-250 µm).

**(C)** Number of periclinal divisions in cortex and endodermis cells depending on the distance from the QC at the time of ablation is increased after PLT2 induction; as measured in WT and *35S::PLT2-GR* (treated with 5 µM DEX 1 h prior ablation) 12 h after ablation. Roots with ectopic oblique divisions were excluded from the quantifications. Number of ablations per data point; n = 3-26

**(D)** Overexpression of PLT2 starting 1 h before ablation triggered periclinal and oblique divisions in inner adjacent cells. Cortex cells are already partly elongated. Ablation was performed at 282 µm distance from the QC.

**(E)** Number of periclinal divisions after ablation in *plt1*, *plt2* single and *plt1plt2* double mutants in different cell layers at random distance from the QC after 12 h. Data are represented as weighted mean (bar) and individual experiments (dots, area indicates sample size)**.** Asterisks correspond to p-values from conditional logistic regression (CLR); *plt1* (cortex): 0.000538, *plt2* (endodermis): 0.0231, *plt1plt2* (epidermis): 9.99E-07.

**(F)** Periclinal division was not induced in epidermis in the *plt1plt2* double mutant 12 h after ablation. Red asterisks: sites of ablation. Roots were stained with propidium iodide.

See also Figure S2

---

**Accelerated progression through cell cycle during restorative division**

To analyze whether the wounding only changes the plane of cell division from anticlinal to periclinal or, in addition, also accelerates the entry into and/or progression of the cell cycle, we performed a time series counting the divisions associated with the ablation events using the vertical stage microscope with automatic tracking (Von Wangenheim et al., 2017). Roots without ablations underwent anticlinal divisions in a spatially and temporarily regular manner, which can be observed as a nearly linear increase of cumulative divisions over time. Fitted sigmoidal curves showed nearly flat derivatives showing that there is equal probability of cell divisions during the observed time frame in all cell types (Figure 3A). In contrast, wounding-induced periclinal divisions showed different but very uniform characteristics within different roots. After a lag-time of approx. 5-7 h, the cumulative periclinal division events from ~40 ablation sites increased rapidly and reached a maximum within 10 additional hours. The derivatives of the fitted sigmoidal curves showed that ablation highly increased the probability of divisions (Figure 3B). Additionally, the speed of induction of restorative cell divisions varied markedly between cell types. Whereas epidermis cells induced divisions almost uniformly, endodermis division events spread over a slightly broader time scale. The ability to specifically induce divisions in cortex cells varied from a rate comparable to endodermis (Figure S3A) to situations without wounding (Figure S3B) but mostly was somewhere between these two extrema (Figure 3B). In most cases for cortex (60%) and epidermis (70%), exponential curves

showed a better fit, while endodermis curves in majority (70%) fitted better to a sigmoidal behavior. Pericycle cells are not efficiently trackable for prolonged periods, but endpoint measurements (e.g. 12 h) after ablation revealed induction times similar to the endodermis (Figure S3C). Despite these differences, the minimal observed induction time of ~5 h is consistent within all cell types.

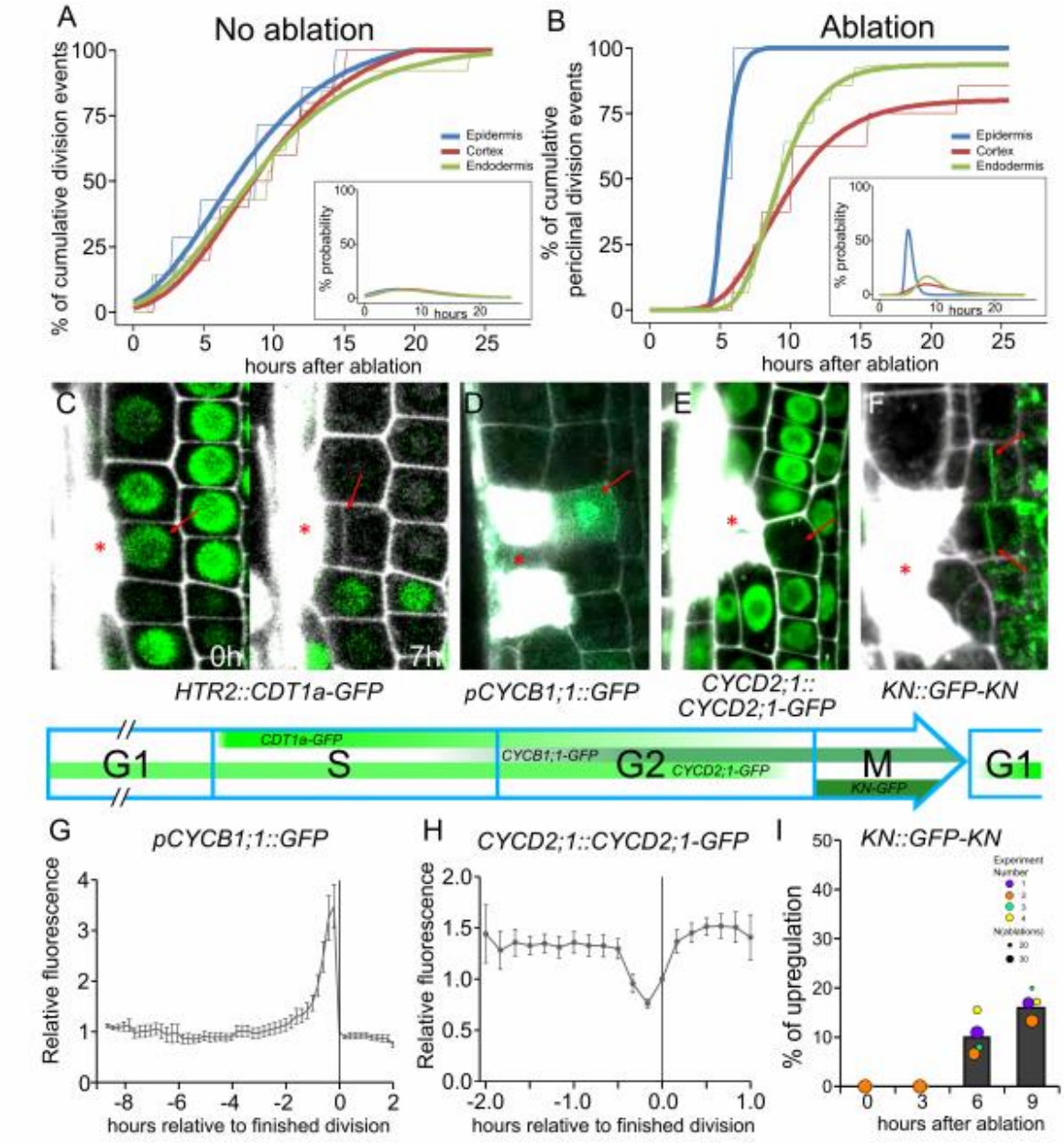


**Figure 3. Accelerated activation of cell cycle progression**

**(A** and **B)** Cumulative divisions in roots monitored by vertical stage microscopy (observed roots; n = 10 for each experiment). Without ablations all cell types divided slowly at the same rate, as seen in the quantification of anticlinal divisions in roots with virtual ablations (n = 4 per root) **(A),** whereas division rates were much faster and differed markedly between cell types after wounding, as seen in quantifications of periclinal divisions in roots with laser ablations ( n = 3 per root) **(B).** Thin lines show

raw data and thick lines show fitted curves calculated by least square estimates (sigmoidal curves: y=a*e^(-b*e^(-c*x))). Insets show derivatives of fitted curves.

**(C-F)** Expression pattern of cell cycle regulators during restorative divisions. Inner adjacent cells of ablated cells were already in S-phase during ablation as indicated by strong *HTR2::CDT1a-GFP* signal (left) but still performed periclinal cell division (right) **(C)**. Mean *CDT1a-GFP* fluorescence intensity at 0 h after ablation relative to the first time point after ablation: 9.3 ± 1.6 (n = 8 cells). G2/M transition marker, *pCYCB1;1::GFP* is specifically upregulated before restorative divisions **(D)**, while *CYCD2;1::CYCD2;1-GFP* leaves the nucleus shortly before division **(E)** and cytokinesis marker, *KN::GFP-KN* is upregulated at the newly formed cell plate **(F)**. Progression of cell cycle phases are shown in blue arrow with green stripes indicating expression patterns as observed or previously reported (for *CDT1a-GFP*: Yin et al., 2014).

**(G-I)** Quantification of fluorescent signals of marker gene expressions of *pCYCB1;1::GFP* **(G),** *CYCD2;1::CYCD2;1-GFP* **(H)** and *KN::GFP-KN* **(I)** during restorative divisions after ablation. Data for *pCYCB1;1::GFP* and *CYCD2;1::CYCD2;1-GFP* was collected by long-term vertical stage imaging over 24 h and are presented as mean fluorescence intensity relative to time point of finished division of subsequently followed cells (n = 16 and n = 10, respectively) ± SEM and is supported by three qualitative experiments. *KN::GFP-KN* is represented as mean (bar) and individual experiments (dots, area indicates sample size) of qualitative analysis of GFP signals.

Red asterisks: sites of ablation. Roots were stained with propidium iodide.

See also Figure S3

---

Next, we observed progression of the cell cycle after ablation and analyzed, which transition steps are required for the initiation of restorative cell divisions. We tested the expression of S, G2/M and cytokinesis-specific markers which also showed dynamic changes in proliferative cell divisions occurring in a seemingly random diverse spatial and temporal distribution within the root meristem (Dewitte and Murray, 2003). The evolutionary conserved inhibitor of the G1 to S-phase transition RETINOBLASTOMA-RELATED1 (RBR1) (Ebel et al., 2004) in the *RBR1::RBR1-GFP* marker line showed occasionally specific downregulation in the inner neighbor cells to the wound before restorative divisions were induced (Figure S3J). However, in long-term imaging experiments, we could not observe any specific expression changes in most cells that perform restorative divisions. So we investigated a synthetic S-phase marker, *HTR2::CDT1a-GFP,* which gets promptly activated when a cell enters the S-phase and gets slowly degraded until the cytokinesis (Yin et al., 2014). Most cells in the root meristem showed strong expression in this marker, meaning they were currently in S-phase. When we ablated cells adjacent to such cells, we observed that S-phase cells were able to trigger

restorative divisions including the switch to periclinal orientation (Figure 3C) suggesting that a G1 to S-phase transition (e.g. by downregulation of RBR1) is not crucial for restorative divisions.

A transcriptional activator of G1/S phase transition genes, ETHYLEN RESPONSE FACTOR 115 (in the *ERF115::GFP-NLS* line) was upregulated around 4-5 h after ablation, prior to restorative cell divisions as described previously (Heyman et al., 2016; Heyman et al., 2013). Nonetheless, the ERF115 upregulation is specific to endodermal and stele cells next to wound and was not observed in epidermis and cortex cells (Figures S3D-S3G). Accordingly, the *ERF115-SRDX* dominant negative line showed significantly reduced number of restorative cell divisions in endodermis and lower number of divisions in pericycle (Figure S3H). This suggests that, although not required, the transition from G1 to S phase is part of the restorative division initiation and increases the amount of restorative cell divisions that occur within 12 h. The binding partner of ERF115, PHYTOCHROME A SIGNAL TRANSDUCTION1 (PAT1, Heyman et al., 2016) and one of the downstream targets WOUND INDUCED DEDIFFERENTIATION 1 (WIND1, Iwase et al., 2011) did not show any specific expression changes during restorative divisions (Figure S3K and S3L). Additionally, *wind1* mutant and overexpression lines did not show any defects in periclinal division after ablation (Figure S3I).

Next, we observed the progression through the G2 phase and its importance for restorative divisions. Using long-term imaging during restorative divisions, we observed upregulation of the G2/M marker *pCYCB1;1::GFP* (Ubeda-Tomás et al., 2009) and downregulation of *CYCD2;1::CYCD2;1-GFP* (Sanz et al., 2011) as it normally occurs during progression through G2 phase (Figure 3D-E and 3G-H). Additionally, we observed the cytokinesis onset and progression as marked by the cytokinesis-specific protein KNOLLE in *KN::GFP-KN* (Reichardt et al., 2007) at the newly formed cell plate during restorative divisions (Figures 3F and 3I). This demonstrates, that enhanced progression through the cell cycle requires the differential expression of canonical G2 and M phase genes.

Thus, the quantifications of cumulative cell divisions revealed that wounding-induced restorative divisions occur significantly faster than regular proliferative divisions. Notably, whereas for the normal, proliferative cell division rates, there are no visible differences between the cell types, the restorative cell divisions show strongly divergent rates of divisions in different cell types. Whereas these quantifications cannot discriminate between accelerated entry and accelerated progression of the cell cycle, the molecular markers further confirmed the accelerated cell cycle progression. Additionally, it showed that coordinated G1/S phase

transition is not required for restorative cell division, while G2/M phase transitions are tightly controlled after wounding.

**Restorative cell divisions generate daughter cells with distinct, correct fates**

Next, we addressed the cell fate of the daughter cells generated by restorative cell divisions. In the root, the stereotypic divisions of the stem cells generate all cell types, which, subsequently after leaving the stem cell niche, have their fixed identities propagated by the proliferative anticlinal cell divisions (Van den Berg et al., 1995; Berger et al., 1998; Dolan et al., 1993; Kidner et al., 2000).

To assess possible cell fate changes, we used specific marker lines for different cell types (Figure 4A) and followed their expression during and after restorative cell divisions. After ablation of LRC cells in the LRC-specific marker line *SMB::SMB-GFP* (Willemsen et al., 2008), we measured GFP fluorescence in both daughter cells generated by a restorative division of the epidermis. The SMB-GFP expression in outer daughter cells, facing the ablation site, as compared to the inner cell, became significantly higher 4 h after division (Figures 4B and 4G). This indicates that the outer epidermis daughter cell generated by the restorative division acquired rapidly the LRC fate replacing the eliminated cell.

Next, we observed dividing cortex cells after ablation of epidermal cells in the roots of the cortex and endodermis-specific marker line *J0571* (Haseloff, 1999; Mylona et al., 2002). The difference between inner and outer daughter cells appeared about 24 h after ablation and the GFP signal almost disappeared from the outer cells after 32 h, indicating that these cells were losing cortex cell fate and acquired their new fate (Figures 4C and 4H). Additionally, at about 24 h after epidermis ablation, outer cells of periclinally divided cortex cells started to express the epidermal marker *WER::GFP* (Lee and Schiefelbein, 1999) confirming that these cells were in process of acquiring the cell fate of the eliminated epidermal cell (Figures 4D and 4H).

After ablation of cortex cells, we monitored the endodermis-specific marker *SCR::SCR-YFP* and the cortex-specific marker *Co2::HYFP* (Heidstra et al., 2004) to analyze the cell fate changes after restorative divisions. Also in this case, the outer daughter cell gradually lost its endodermal fate, as evidenced by decreasing SCR-YFP expression (Figures 4I and S4A), and acquired the cortex fate (increasing *Co2::HYFP* expression) at about 16 h - 24 h after ablation (Figures 4E and 4I).

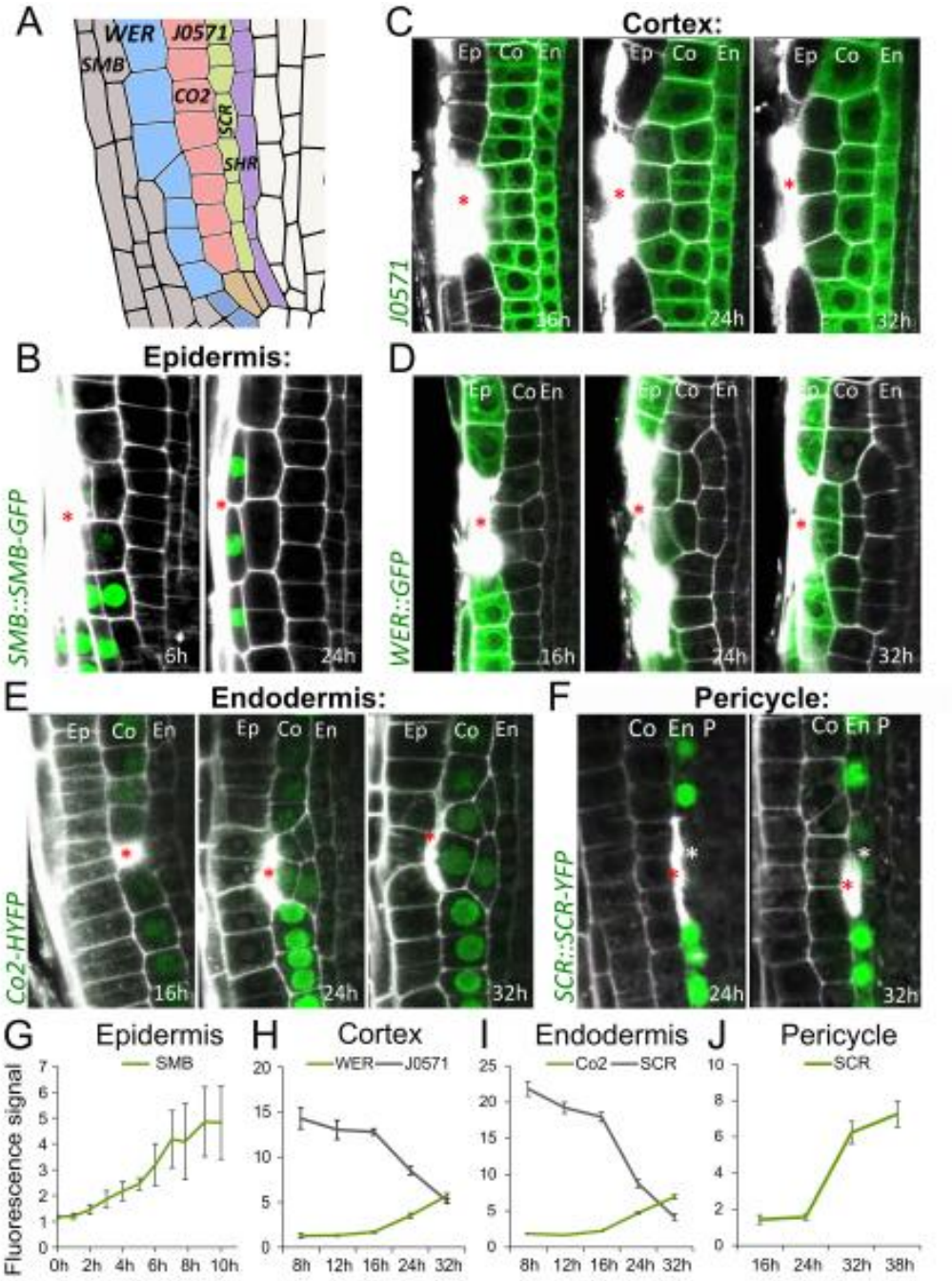


**Figure 4. Restorative cell divisions generate daughter cells with distinct cell fates**

**(A)** Expression domains of marker lines in *Arabidopsis* root meristem.

**(B)** Ablation of LRC cells. Expression of LRC marker, *SMB::SMB-GFP* is restored in newly formed LRC cells. Total number of ablations; n = 5 for all time points.

**(C** and **D)** Ablation of epidermal cells. Expression of cortex and endodermis marker *J0571* is downregulated in the outer daughter cells of periclinally divided cortex cells **(C)**, while epidermis marker *WER::GFP* is upregulated **(D).** Numbers of ablations per time point; n = 19-77 (*J0571*), n = 16-66 (*WER::GFP*).

**(E)** Ablation of cortex. Expression of cortex marker *Co2::HYFP* is upregulated in outer daughter cells of periclinally divided endodermis cells, while endodermis marker *SCR::SCR-YFP* is downregulated (see Figure S4A). *Co2::HYFP*; n = 43-79 ablations per time point.
**(F)** Ablation of endodermis. Expression of *SCR::SCR-YFP* is upregulated in outer cells of periclinally divided pericycle cells. n = 13-23 ablations per time point.
**(G-J)** Quantification of fluorescent signals of marker gene expressions in periclinally divided cells after ablation. Relative signal intensity between outer/inner daughter cells in periclinally divided epidermis **(G)** and average fluorescent signal in cortex **(H),** endodermis **(I)** and pericycle **(J)** at different time points. Outer daughters were measured if the inner adjacent cells divided multiple times (as seen in **D**). Data are represented as mean ± SEM.
Red asterisks: sites of ablation. Roots were stained with propidium iodide.
See also Figure S4

---

We also followed cell fate changes after elimination of an endodermal cell, which is replaced by the restorative division of the adjacent pericycle cell using endodermal *SCR::SCR-YFP* and *SHR::SHR-GFP* that is more uniformly distributed in stele including pericycle cells but is restricted to the nucleus specifically in endodermis (Nakajima et al., 2001). Analogically to other cell types, we observed that the newly formed outer daughter cell gradually changed its fate to become endodermis as manifested by the activation of SCR-YFP expression (Figures 4F, 4J and S4B) and nuclear appearance of SHR-GFP (Figure S4C).

In rare cases (well below 10% of events) also cells at the outer side of the wound would divide periclinally, in addition to cells at the inner side. Notably, in such cases we did not detect any changes in cell fate of the daughter cells using *SCR::SCR-YFP*, *WER::GFP* and *E4722* marker lines (Fig. S4D-S4I) contrasting with consistent cell fate re-specifications at the inner wound side. This suggests that an inside-to-outside intercellular signaling is required for correct re-specification during wound regeneration.

Taken together, restorative periclinal divisions induced by wounding generate daughter cells that replace dead or damaged cells by acquiring a new, "correct" cell fate. Thus, restorative cell division represents a special case of formative division. This necessitates the existence of multiple intercellular signaling mechanisms constantly providing positional information to the cells, which acts also outside the stem cell niche.

**Re-activation of SHR/SCR-CYCD6 stem cell program replaces eliminated cortex**

How do the cells adjacent to the wound get activated and can generate cells with new, correct identities during wound healing? The asymmetric cell division generating different cell types occurs typically only in the stem cell niche. For example, cortex and endodermis cell files originate from the same stem cell, the cortex-endodermis initial (CEI). The CEI continuously divides anticlinally to renew itself and produce a daughter cell, which further divides periclinally to generate cortex and endodermis (De Rybel et al., 2016; Helariutta et al., 2000; Kumpf and Nowack, 2015; Scheres et al., 2002). This process is governed by the transcription factors SHORTROOT (SHR) and SCARECROW (SCR), which activate the expression of CYCD6;1 and thus initiate a switch in division plane orientation (Heidstra et al., 2004; Sozzani et al., 2010; Figure 5A). Hence, *scr* and *shr* mutants lacking the initial formative division contain only a single layer of ground tissue, while overexpression of SHR or CYCD6;1 leads to the formation of additional ground tissue cell layers (Benfey et al., 1993; Sevilem et al., 2015). Despite SHR and SCR being expressed throughout the whole root meristem, activation of CYCD6;1 and formative cell division within young seedlings occurs only in the stem cell niche (Cruz-Ramírez et al., 2012; Heidstra et al., 2004; Sozzani et al., 2010; Yu et al., 2017).

We have examined involvement of the SHR/SCR-CYCD6;1 module in the restorative division. In the *shr* and *scr* mutants, the restorative cell divisions specifically in the single ground tissue layer were significantly defective, whereas the division of other cell types occurred normally (Figures 5B and 5C). Notably, *CYCD6;1::GFP* and *CYCD6;1::CYCD6;1-GFP* expression, typically detectable only in the stem cells, was upregulated specifically in endodermal cells next to eliminated cortex cells and started between 3 and 7 h after wounding well before the onset of the restorative division (Figures 5D, S5A and Movie S4). On the other hand, SHR-GFP and SCR-YFP signal intensity decreased before and during mitosis (Figures 5E, S5B and S5C). A similar downregulation of SCR/SHR and activation of CYCD6;1 expression can be observed outside of the stem cell niche during initiation of an additional cortex layer, so called middle cortex (Benfey et al., 1993; Paquette and Benfey, 2005). Middle cortex formation shares some similarities with restorative divisions of endodermis such as switch of cell division plane to periclinal. However, it occurs only in older roots and is under a strong control of the phytohormone gibberellic acid (GA) (Cui and Benfey, 2009; Gong et al., 2016; Paquette and Benfey, 2005). Notably, neither application of GA nor GA biosynthesis inhibitor paclobutrazol (PAC) had an influence on the competence of endodermis cells to undergo restorative divisions (Figures S5D-S5G) implying that restorative division and middle cortex formation while both depending on SHR/SCR–CYCD6;1 signaling, use at least partly divergent mechanisms.

Our observations show that cortex elimination by wounding activates the endodermis/cortex SHR/SCR–CYCD6;1 stem cell program in the underlying endodermis cell enabling its restorative division and ultimately healing the wound by generating daughter cells with the correct fate.

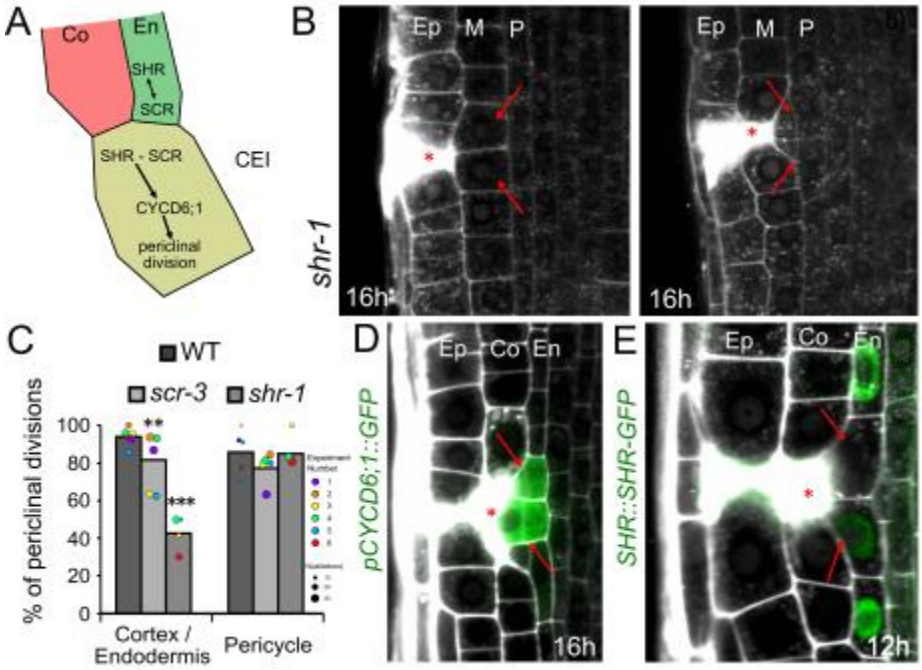


**Figure 5. Re-activation of SHR/SCR-CYCD6;1 module during restoration of cortex.**

**(A)** SHR/SCR-CYCD6;1 module in ground tissue development (Fisher and Sozzani, 2016; Sozzani et al., 2010).

**(B** and **C)** Ablation of epidermal cells **(B - left)** and ground tissue **(B - right)** in *shr-1* mutant. Quantification of periclinal divisions in *scr-3* and *shr-1* **(C)**. Data are represented as weighted mean (bar) and individual experiments (dots, area indicates sample size); p-values from CLR for *scr-3*: 0.00234; *shr-1*: 8.61E-9.

M: ground tissue layer formed in *shr* mutants.

**(D** and **E)** Expression of *CYCD6;1::GFP* is upregulated in periclinally divided endodermis cell after ablation of cortex (For the translational fusion see Figure S5A) **(D)**, while *SHR::SHR-GFP* is downregulated before periclinal division (see also Figure S5B) **(E)**. Total number of ablations; n = 109 (CYCD6;1), n = 101 (SHR).

Red asterisks: sites of ablation. Roots were stained with propidium iodide.

See also Figure S5

**Re-activation of FEZ/SMB stem cell program replaces eliminated epidermis**

Besides cortex/endodermis initials, the stem cell niche consists of other initials that divide asymmetrically to form distinct cell types, such as the LRC/epidermis initials (LEI).

Their correct division pattern is regulated by two transcription factors, FEZ and SOMBRERO (SMB) (Fisher and Sozzani, 2016; Willemsen et al., 2008). FEZ induces the asymmetric division of the initial, while SMB inhibits further divisions of already specified LRC cells. *fez* mutants lack additional stem cell divisions and show decreased number of LRC layers, while stem cells in *smb* undergo more periclinal divisions and generate additional LRC layers (Fisher and Sozzani, 2016; Willemsen et al., 2008). The concomitant expression of both proteins is specific to LRC/epidermis initials in the stem cell niche and very young LRC cells, where they interact with each other in a negative feedback loop, and their expression is never observed in already specified epidermis cells (Figure 6A).

We observed a specific upregulation of both *FEZ::FEZ-GFP* and *SMB::SMB-GFP* in epidermis cells adjacent to wounded LRC cells (Figures 6B, 6C, S6A and S6B). The upregulation started 4-6 h after LRC elimination and was always followed by a periclinal division. While the FEZ expression dropped shortly after division, SMB was asymmetrically upregulated in the newly forming LRC cells, and it vanished in the remaining epidermis cells (see Figure 4B). In the *fez* mutant we observed a reduction in epidermis division rate and an increase in the rates of cortex and endodermis (Figures 6D and 6E). In the *smb* mutant, the rate of epidermis division following LRC elimination dropped significantly, whereas other cell types showed normal rate of restorative divisions (Figures 6D and 6F).

These observations revealed a specific upregulation and functional requirement of both these stem cell regulators for the restorative cell division of epidermis leading to the replacement of the eliminated LRC by daughter cells with a correct cell fate. Thus, as in case of cortex replacement, the re-activation of the specific stem cell program mediates also the replacement of LRC during wound healing.

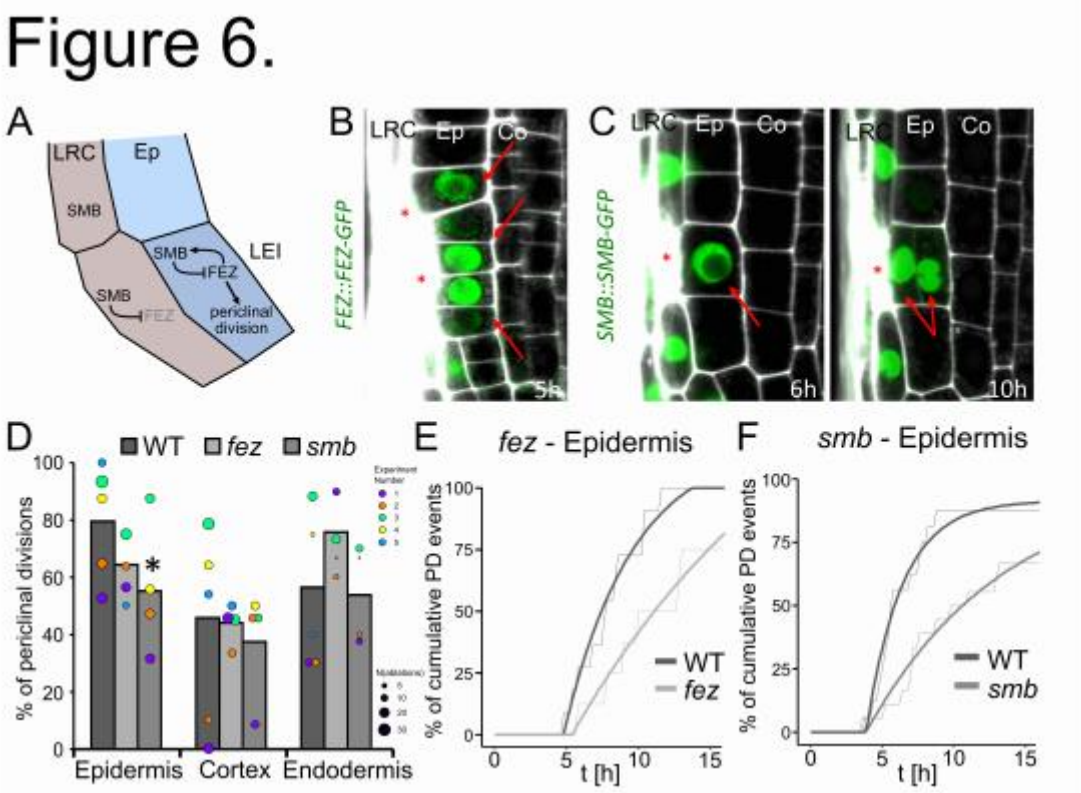


**Figure 6. Reactivation of FEZ/SMB module during restoration of LRC.**

**(A)** FEZ/SMB module in LRC development (Fisher and Sozzani, 2016; Willemsen et al., 2008). Grey font shows reduced expression.

**(B** and **C)** Expression of *FEZ::FEZ-GFP* **(B)** and *SMB::SMB-GFP* **(C)** is upregulated in epidermal cells after ablation of LRC (see also Figure S6A & S6B).

**(D)** Quantification of periclinal divisions after ablation in *fez* and *smb* mutants in different layers show reduced numbers in mutant epidermis cells. Data are represented as weighted mean (bar) and individual experiments (dots, area indicates sample size); p-values from CLR: *fez*: 0.075 (epidermis), 0.50 (cortex), 0.077 (endodermis); *smb*: 0.013 (epidermis), 0.79 (cortex), 0.73 (endodermis)

**(E** and **F)** Cumulative divisions over time in *fez* **(E)** and *smb* **(F)** monitored by vertical stage microscopy. Observed ablations; n = 20 per genotype. Thin lines show raw data and thick lines show fitted curves calculated by least square estimates (y=a-b*e^(c*x)). See also Figure S6C.

Red asterisks: sites of ablation. Roots were stained with propidium iodide.

See also Figure S6.

## Discussion

Plants evolved distinct mechanisms of patterning as compared to animals due to the constraints of immobile cells encapsulated within cell walls. Owing to their sessile life style, they also frequently must endure injuries, but little is known how the tissue is restored after wounding.

In this work, we address the mechanisms underlying wound healing and pattern restoration using targeted laser elimination of different cell types coupled to prolonged live cell imaging. This approach allowed us to identify in multiple plant species the process of restorative patterning, which encompasses restorative cell divisions initiated after injury, subsequent *de novo* specification of the correct cell fates and ultimately leads to replacement of the eliminated cells and correct regeneration of the injured tissues.

**Restorative cell divisions specifically and correctly replace eliminated cells**

We have shown here that root cells disrupted by injury are not simply replaced by a proliferation of healthy cells from the same cell file adjacent above and below to the wound. Instead, inner adjacent cells become activated to replace the dead neighbor by a process we call restorative patterning. This special type of formative cell division involves several coordinated processes: (i) recognition of the disrupted tissue by inner adjacent cells; (ii) accelerated entry into and progress through the cell cycle; (iii) reorientation of the cell division plane; and (iv) "correct" cell fate re-specification of the generated daughter cell, which fills the wound. Furthermore, restorative divisions in inner adjacent cells were observed independently of the nature of tissue disruption: ablation of single or multiple cell layers, drug-induced cell death and natural collapse of multiple cells.

The underlying signaling cascades for restorative patterning remain largely elusive however, we provide some initial insights. The known components of mechanosensing, periclinal cell divisions and preprophase band formations do not seem to be involved (Figure S7). On the other hand, the graded expression of PLT transcription regulators seems to provide some cell types of the root with their regenerative competence.

Our observations also show that the main fraction of dividing cells finish mitosis between 5 and 8 h, the minimum time frame required for cell divisions in plants and other eukaryotes (Mickelson-Young et al., 2016). Therefore, signaling from the wound to initiate cell cycle transitions in inner adjacent cells must happen very rapidly after tissue disruption and likely relies on non-genomic factors, such as mechanical properties and local geometry of disrupted tissues.

The switch in the division plane is a crucial part of the restorative patterning. Notably, it has been shown that mechanical perturbations, including cell ablation, in the shoot apical meristem can trigger division plane reorientation of surrounding cells (Louveaux et al., 2016) indicating that the process of restorative patterning and the coordinated cell division plane switching, here characterized in the root, may operate more globally throughout the plant.

**Reactivation of stem cell mechanisms mediates restorative patterning**

A remarkable feature of restorative patterning is that cells undergoing proliferative divisions with already clearly specified fates start to perform formative divisions and undergo cell fate re-specification. This allows the generation of daughter cells with correct cell fates to regenerate the disrupted tissue.

In the cell type lineages, which share common ancestors in the stem cell niche, such as Lateral Root Cap/Epidermis initials and Cortex/Endodermis initials, we observed an activation of regulators usually specific only to the respective stem cells. The upstream activators of these stem cell pathways await identification, but the genetic analysis revealed that restorative patterning is much less efficient albeit not completely prevented in mutants defective in those stem cell regulators. Nonetheless, restorative divisions where the ablated and the activated cell do not have a common ancestor (especially cortex division after epidermis ablation) still occur but with reduced efficiency in division plane switching and wound healing. This implies some redundancy in mechanisms for restorative patterning and indicates the existence of a slower mechanism, which potentially operates in all cell types regardless of their stem cell ancestry. Hence, the additional activation of the stem cell regulators, which were shown to ectopically induce periclinal divisions by overexpression (Sozzani et al., 2010; Willemsen et al., 2008; Yu et al., 2017), provides increased efficiency and robustness to this so far unidentified, "default", cell type-independent restorative mechanism.

For the part of restorative patterning mechanism that involves stem cell pathway activation, one can envision that even already specified cells preserve a "memory" of their stem cell ancestry and upon receiving a wound signal reactivate the stem cell pathway. However, the basal, default restorative patterning implies the existence of global positional signaling mechanism(s) that determine which cell fate the daughter cells should adopt following restorative division. While the cell fates of inner, wound-adjacent cells of ablation is re-specified, the cell fate of occasionally dividing outer adjacent cells is not affected, suggesting that the positional signaling mediating the coordinated cell fate changes occurs in a radial direction from inside to outside. Thus, the mechanism of wound healing by restorative divisions starts always from the inner tissues regardless of the wounding process.

As suggested previously (Van den Berg et al., 1995; Berger et al., 1998; Kidner et al., 2000), such positional signaling would operate outside the stem cell niche, hence constantly allow already specified cells to adapt their cell fate according to their position within the tissue

architecture. In case of endodermis specification, this is likely the well-known SHR/SCR radial signaling module that is expressed and operates throughout the whole root meristematic zone (Heidstra et al., 2004) but for other cell types; any notion of this signaling remains elusive.

**Conclusion**

In summary, this work provides insights into the plant-specific mechanism underlying wound healing. Focusing on the coordinated response of already specified root cells to the local injury we uncovered a process of restorative patterning, which correctly replaces eliminated cells and allows plant tissues to heal despite the absence of cell migration, which is the basis of wound healing in animals. The nature of the wound signal remains enigmatic, but the downstream restorative patterning involves re-activation of stem cell-specific signaling pathways inducing asymmetric, formative divisions and cell fate re-specifications ultimately closing and healing the wound. In addition to the regenerative competence requiring and correlating with the gradually decreasing expression of PLT transcription factors, our result also suggested the existence of undiscovered signaling mechanisms constantly conveying positional information throughout all tissues of the root meristem.

Besides these insights into the mechanism of wound healing, our method of laser-assisted local tissue perturbation coupled with long-term, high-resolution imaging during vertical growth opens new possibilities to address the mechanism of intercellular signaling and patterning in plant tissues. Thus, further studies into restorative patterning using molecular genetics, single cell transcriptomics and mechanical modeling among other approaches will reveal not only a broader understanding of the mechanism of wound healing but also how plants establish and maintain their body patterns.

**Acknowledgements**

We are thankful to Philip Benfey, Malcolm Bennett, David Bouchez, Kim Boutilier, Alice Cheung, Bert de Rybel, Lieven de Veylder, Walter Dewitte, Zhaojun Ding, Jean-Marie Frachisse, Renze Heidstra, Ykä Helariutta, Gerd Jürgens, Zoltan Magyar, Moritz Nowack, Ben Scheres, John Schieffelbein, Arp Schnittger, Keiko Sugimoto, Masao Tasaki, Steffen Vanneste, Dolf Weijers, Viola Willemsen and Shuang Wu for sharing material. We would also like to acknowledge the Bioimaging Facility at IST Austria for providing imaging service and assistance. The research leading to these results has received funding from the European Research Council under the European Union's Seventh Framework Programme (FP7/2007-

2013) / ERC grant agreement n° 742985, Marie Curie Fellowship (contract 753138) to S.Y. and from the Federation of European Biochemical Societies (FEBS) Long-Term Fellowship to P.My.

## Author contributions

P.Ma. and J.F. initiated the project. P.Ma., L.H., S.Y. and P.My. performed experiments and analyzed data. P.Ma., L.H., S.Y. and J.F. wrote the manuscript. P.My. and E.B. edited the manuscript. J.F. and P.My. acquired funding.

## Declaration of Interests

The authors declare no competing interests.

## References

Aida, M., Beis, D., Heidstra, R., Willemsen, V., Blilou, I., Galinha, C., Nussaume, L., Noh, Y.-S., Amasino, R., and Scheres, B. (2004). The PLETHORA genes mediate patterning of the Arabidopsis root stem cell niche. Cell *119*, 109–120.

Benfey, P.N., Linstead, P.J., Roberts, K., Schiefelbein, J.W., Hauser, M.T., and Aeschbacher, R.A. (1993). Root development in Arabidopsis: four mutants with dramatically altered root morphogenesis. Development *119*, 57–70.

Van den Berg, C., Willemsen, V., Hage, W., Weisbeek, P., and Scheres, B. (1995). Cell fate in the Arabidopsis root meristem determined by directional signalling. Nature *378*, 62–65.

Berger, F., Haseloff, J., Schiefelbein, J., and Dolan, L. (1998). Positional information in root epidermis is defined during embryogenesis and acts in domains with strict boundaries. Curr. Biol. *8*, 421–430.

Blilou, I., Xu, J., Wildwater, M., Willemsen, V., Paponov, I., Friml, J., Heidstra, R., Aida, M., Palme, K., and Scheres, B. (2005). The PIN auxin efflux facilitator network controls growth and patterning in Arabidopsis roots. Nature *433*, 39–44.

Campbell, M. J. (2006). Statistics at square two: understanding modern statistical applications in medicine (Blackwell).

Colombelli, J., Grill, S.W., and Stelzer, E.H.K. (2004). Ultraviolet diffraction limited nanosurgery of live biological tissues. Rev. Sci. Instrum. *75*, 472.

Cools, T., Iantcheva, A., Weimer, A.K., Boens, S., Takahashi, N., Maes, S., Van den Daele, H., Van Isterdael, G., Schnittger, A., and De Veylder, L. (2011). The Arabidopsis thaliana Checkpoint Kinase WEE1 Protects against Premature Vascular Differentiation during Replication Stress. Plant Cell *23*, 1435–1448.

Cruz-Ramírez, A., Díaz-Triviño, S., Blilou, I., Grieneisen, V.A., Sozzani, R., Zamioudis, C., Miskolczi, P., Nieuwland, J., Benjamins, R., Dhonukshe, P., et al. (2012). A bistable circuit involving SCARECROW-RETINOBLASTOMA integrates cues to inform asymmetric stem cell division. Cell *150*, 1002–1015.

Cui, H., and Benfey, P.N. (2009). Interplay between SCARECROW, GA and LIKE HETEROCHROMATIN PROTEIN 1 in ground tissue patterning in the Arabidopsis root. Plant J. *58*, 1016–1027.

De Rybel, B., Möller, B., Yoshida, S., Grabowicz, I., Barbier de Reuille, P., Boeren, S., Smith, R.S., Borst, J.W., and Weijers, D. (2013). A bHLH complex controls embryonic vascular tissue establishment and indeterminate growth in Arabidopsis. Dev. Cell *24*, 426–437.

De Rybel, B., Adibi, M., Breda, A.S., Wendrich, J.R., Smit, M.E., Novák, O., Yamaguchi, N., Yoshida, S., Van Isterdael, G., Palovaara, J., et al. (2014). Plant development. Integration of growth and patterning during vascular tissue formation in Arabidopsis. Science *345*, 1255215.

De Rybel, B., Mähönen, A.P., Helariutta, Y., and Weijers, D. (2016). Plant vascular development: from early specification to differentiation. Nat. Rev. Mol. Cell Biol. *17*, 30–40.

Dewitte, W., and Murray, J.A.H. (2003). The plant cell cycle. Annu. Rev. Plant Biol. *54*, 235–264.

Dolan, L., Janmaat, K., Willemsen, V., Linstead, P., Poethig, S., Roberts, K., and Scheres, B. (1993). Cellular organisation of the Arabidopsis thaliana root. Development *119*, 71–84.

Duan, Q., Kita, D., Li, C., Cheung, A.Y., and Wu, H.-M. (2010). FERONIA receptor-like kinase regulates RHO GTPase signaling of root hair development. Proc. Natl. Acad. Sci. U. S. A. *107*, 17821–17826.

Ebel, C., Mariconti, L., and Gruissem, W. (2004). Plant retinoblastoma homologues control nuclear proliferation in the female gametophyte. Nature *429*, 776–780.

Efroni, I., Mello, A., Nawy, T., Ip, P.-L., Rahni, R., DelRose, N., Powers, A., Satija, R., and Birnbaum, K.D. (2016). Root Regeneration Triggers an Embryo-like Sequence Guided by Hormonal Interactions. Cell *S0092-8674*, 1–13.

Fisher, A.P., and Sozzani, R. (2016). Uncovering the networks involved in stem cell maintenance and asymmetric cell division in the Arabidopsis root. Curr. Opin. Plant Biol. *29*, 38–43.

Fukaki, H., Fujisawa, H., and Tasaka, M. (1996). SGR1, SGR2, SGR3: novel genetic loci involved in shoot gravitropism in Arabidopsis thaliana. Plant Physiol. *110*, 945–955.

Galinha, C., Hofhuis, H., Luijten, M., Willemsen, V., Blilou, I., Heidstra, R., and Scheres, B. (2007). PLETHORA proteins as dose-dependent master regulators of Arabidopsis root development. Nature *449*, 1053–1057.

Gifford, M.L., Dean, A., Gutierrez, R.A., Coruzzi, G.M., and Birnbaum, K.D. (2008). Cell-specific nitrogen responses mediate developmental plasticity. Proc. Natl. Acad. Sci. U. S. A. *105*, 803–808.

Gong, X., Flores-Vergara, M.A., Hong, J.H., Chu, H., Lim, J., Franks, R.G., Liu, Z., and Xu, J. (2016). SEUSS integrates gibberellin signaling with transcriptional inputs from the SHR-SCR-SCL3 module to regulate middle cortex formation in the Arabidopsis root. Plant Physiol. *170*, 1675–1683.

Harashima, H., Dissmeyer, N., and Schnittger, A. (2013). Cell cycle control across the eukaryotic kingdom. Trends Cell Biol. *23*, 345–356.

Hartsema, A. (1926). Anatomische und experimentelle Untersuchungen über das Auftreten von Neubildungen an Blättern von Begonia Rex. Rec Trav Bot N *23*, 305–361.

Haseloff, J. (1999). GFP variants for multispectral imaging of living cells. Methods Cell Biol. *58*, 139–151.

Haswell, E.S., Peyronnet, R., Barbier-Brygoo, H., Meyerowitz, E.M., and Frachisse, J.-M. (2008). Two MscS homologs provide mechanosensitive channel activities in the Arabidopsis root. Curr. Biol. CB *18*, 730–734.

Heidstra, R., Welch, D., and Scheres, B. (2004). Mosaic analyses using marked activation and deletion clones dissect Arabidopsis SCARECROW action in asymmetric cell division. Genes Dev. *18*, 1964–1969.

Helariutta, Y., Fukaki, H., Wysocka-Diller, J., Nakajima, K., Jung, J., Sena, G., Hauser, M.T., and Benfey, P.N. (2000). The SHORT-ROOT gene controls radial patterning of the Arabidopsis root through radial signaling. Cell *101*, 555–567.

Hématy, K., Sado, P.-E., Van Tuinen, A., Rochange, S., Desnos, T., Balzergue, S., Pelletier, S., Renou, J.-P., and Höfte, H. (2007). A receptor-like kinase mediates the response of Arabidopsis cells to the inhibition of cellulose synthesis. Curr. Biol. CB *17*, 922–931.

Heyman, J., Cools, T., Vandenbussche, F., Heyndrickx, K.S., Van Leene, J., Vercauteren, I., Vanderauwera, S., Vandepoele, K., De Jaeger, G., Van Der Straeten, D., et al. (2013). ERF115 controls root quiescent center cell division and stem cell replenishment. Science *342*, 860–863.

Heyman, J., Cools, T., Canher, B., Shavialenka, S., Traas, J., Vercauteren, I., Van Den Daele, H., Persiau, G., De Jaeger, G., Sugimoto, K., et al. (2016). The heterodimeric transcription factor complex ERF115-PAT1 grants regeneration competence. Nat. Plants *2*, 1–7.

Higuchi, M., Pischke, M.S., Mähönen, A.P., Miyawaki, K., Hashimoto, Y., Seki, M., Kobayashi, M., Shinozaki, K., Kato, T., Tabata, S., et al. (2004). In planta functions of the Arabidopsis cytokinin receptor family. Proc. Natl. Acad. Sci. U. S. A. *101*, 8821–8826.

Hush, J.M., Hawes, C.R., and Overall, R.L. (1990). Interphase microtubule re-orientation predicts a new cell polarity in wounded pea roots. J. Cell Sci. *96*, 47–62.

Iwase, A., Mitsuda, N., Koyama, T., Hiratsu, K., Kojima, M., Arai, T., Inoue, Y., Seki, M., Sakakibara, H., Sugimoto, K., et al. (2011). The AP2/ERF transcription factor WIND1 controls cell dedifferentiation in Arabidopsis. Curr. Biol. CB *21*, 508–514.

Kidner, C., Sundaresan, V., Roberts, K., and Dolan, L. (2000). Clonal analysis of the Arabidopsis root confirms that position, not lineage, determines cell fate. Planta *211*, 191–199.

Kleinbaum, D. G., & Klein, M. (2010). Logistic regression: a self-learning text (Springer Science & Business Media).

Kumpf, R.P., and Nowack, M.K. (2015). The root cap: a short story of life and death. J. Exp. Bot. *66*, 5651–5662.

Lee, M.M., and Schiefelbein, J. (1999). WEREWOLF, a MYB-related protein in Arabidopsis, is a position-dependent regulator of epidermal cell patterning. Cell *99*, 473–483.

Li, C., Yeh, F.-L., Cheung, A.Y., Duan, Q., Kita, D., Liu, M.-C., Maman, J., Luu, E.J., Wu, B.W., Gates, L., et al. (2015). Glycosylphosphatidylinositol-anchored proteins as chaperones and co-receptors for FERONIA receptor kinase signaling in Arabidopsis. ELife *4*.

Louveaux, M., Julien, J.-D., Mirabet, V., Boudaoud, A., and Hamant, O. (2016). Cell division plane orientation based on tensile stress in Arabidopsis thaliana. Proc. Natl. Acad. Sci. U. S. A. *113*, E4294-4303.

Magyar, Z., Horváth, B., Khan, S., Mohammed, B., Henriques, R., De Veylder, L., Bakó, L., Scheres, B., and Bögre, L. (2012). Arabidopsis E2FA stimulates proliferation and endocycle separately through RBR-bound and RBR-free complexes. EMBO J. *31*, 1480–1493.

Marhavý, P., and Benková, E. (2015). Real-time Analysis of Lateral Root Organogenesis in Arabidopsis. Bio-Protoc. *5*.

Marhavý, P., Bielach, A., Abas, L., Abuzeineh, A., Duclercq, J., Tanaka, H., Pařezová, M., Petrášek, J., Friml, J., Kleine-Vehn, J., et al. (2011). Cytokinin modulates endocytic trafficking of PIN1 auxin efflux carrier to control plant organogenesis. Dev. Cell *21*, 796–804.

Marhavý, P., Montesinos, J.C., Abuzeineh, A., Van Damme, D., Vermeer, J.E.M., Duclercq, J., Rakusová, H., Nováková, P., Friml, J., Geldner, N., et al. (2016). Targeted cell elimination reveals an auxin-guided biphasic mode of lateral root initiation. Genes Dev. *30*, 471–483.

Mazur, E., Benková, E., and Friml, J. (2016). Vascular cambium regeneration and vessel formation in wounded inflorescence stems of Arabidopsis. Sci. Rep. *6*, 33754.

Mickelson-Young, L., Wear, E., Mulvaney, P., Lee, T.-J., Szymanski, E.S., Allen, G., Hanley-Bowdoin, L., and Thompson, W. (2016). A flow cytometric method for estimating S-phase duration in plants. J. Exp. Bot. *67*, 6077–6087.

Mylona, P., Linstead, P., Martienssen, R., and Dolan, L. (2002). SCHIZORIZA and radial pattern of Arabidopsis root. Development *129*, 4327–4334.

Nakajima, K., Sena, G., Nawy, T., and Benfey, P.N. (2001). Intercellular movement of the putative transcription factor SHR in root patterning. Nature *413*, 307–311.

Paquette, A.J., and Benfey, P.N. (2005). Maturation of the Ground Tissue of the Root Is Regulated by Gibberellin and SCARECROW and Requires SHORT-ROOT. Plant Physiol. *138*, 636–640.

Rasmussen, C.G., and Bellinger, M. (2018). An overview of plant division-plane orientation. New Phytol. *219*, 505–512.

Reichardt, I., Stierhof, Y.D., Mayer, U., Richter, S., Schwarz, H., Schumacher, K., and Jürgens, G. (2007). Plant Cytokinesis Requires De Novo Secretory Trafficking but Not Endocytosis. Curr. Biol. *17*, 2047–2053.

Sanz, L., Dewitte, W., Forzani, C., Patell, F., Nieuwland, J., Wen, B., Quelhas, P., De Jager, S., Titmus, C., Campilho, A., et al. (2011). The Arabidopsis D-Type Cyclin CYCD2;1 and the Inhibitor ICK2/KRP2 Modulate Auxin-Induced Lateral Root Formation. Plant Cell *23*, 1–20.

Schaefer, E., Belcram, K., Uyttewaal, M., Duroc, Y., Goussot, M., Legland, D., Laruelle, E., de Tauzia-Moreau, M.-L., Pastuglia, M., and Bouchez, D. (2017). The preprophase band of microtubules controls the robustness of division orientation in plants. Science *356*, 186–189.

Scheres, B., Benfey, P., and Dolan, L. (2002). Root development. Arab. Book *1*, e0101.

Sena, G., Wang, X., Liu, H.Y., Hofhuis, H., and Birnbaum, K.D. (2009). Organ regeneration does not require a functional stem cell niche in plants. Nature *457*, 1150–1154.

Sevilem, I., Yadav, S.R., and Helariutta, Y. (2015). Plasmodesmata: channels for intercellular signaling during plant growth and development. Methods Mol. Biol. Clifton NJ *1217*, 3–24.

Sinnott, E.W., and Bloch, R. (1941). The Relative Position of Cell Walls in Developing Plant Tissues. Am. J. Bot. *28*, 607–617.

Sozzani, R., Cui, H., Moreno-Risueno, M.A., Busch, W., Van Norman, J.M., Vernoux, T., Brady, S.M., Dewitte, W., Murray, J.A.H., and Benfey, P.N. (2010). Spatiotemporal regulation of cell-cycle genes by SHORTROOT links patterning and growth. Nature *466*, 128–134.

Ubeda-Tomás, S., Federici, F., Casimiro, I., Beemster, G.T.S., Bhalerao, R., Swarup, R., Doerner, P., Haseloff, J., and Bennett, M.J. (2009). Gibberellin signaling in the endodermis controls Arabidopsis root meristem size. Curr. Biol. CB *19*, 1194–1199.

Von Wangenheim, D., Hauschild, R., Fendrych, M., Barone, V., Benková, E., and Friml, J. (2017). Live tracking of moving samples in confocal microscopy for vertically grown roots. ELife *6*.

Willemsen, V., Bauch, M., Bennett, T., Campilho, A., Wolkenfelt, H., Xu, J., Haseloff, J., and Scheres, B. (2008). The NAC domain transcription factors FEZ and SOMBRERO control the orientation of cell division plane in Arabidopsis root stem cells. Dev. Cell *15*, 913–922.

Xu, J., Hofhuis, H., Heidstra, R., Sauer, M., and Scheres, B. (2006). A Molecular Framework for Plant Regeneration. Science. *311*, 1–5.

Yamanaka, T., Nakagawa, Y., Mori, K., Nakano, M., Imamura, T., Kataoka, H., Terashima, A., Iida, K., Kojima, I., Katagiri, T., et al. (2010). MCA1 and MCA2 that mediate Ca2+ uptake have distinct and overlapping roles in Arabidopsis. Plant Physiol. *152*, 1284–1296.

Yin, K., Ueda, M., Takagi, H., Kajihara, T., Sugamata Aki, S., Nobusawa, T., Umeda-Hara, C., and Umeda, M. (2014). A dual-color marker system for in vivo visualization of cell cycle progression in Arabidopsis. Plant J. Cell Mol. Biol. *80*, 541–552.

Yu, Q., Li, P., Liang, N., Wang, H., Xu, M., and Wu, S. (2017). Cell-Fate Specification in Arabidopsis Roots Requires Coordinative Action of Lineage Instruction and Positional Reprogramming. Plant Physiol. *175*, 816–827.

Zhu, W., Wang, H., Fujioka, S., Zhou, T., Tian, H., Tian, W., and Wang, X. (2013). Homeostasis of brassinosteroids regulated by DRL1, a putative acyltransferase in Arabidopsis. Mol. Plant *6*, 546–558.

Zürcher, E., Tavor-Deslex, D., Lituiev, D., Enkerli, K., Tarr, P.T., and Müller, B. (2013). A robust and sensitive synthetic sensor to monitor the transcriptional output of the cytokinin signaling network in planta. Plant Physiol. *161*, 1066–1075.

## Supplemental Information

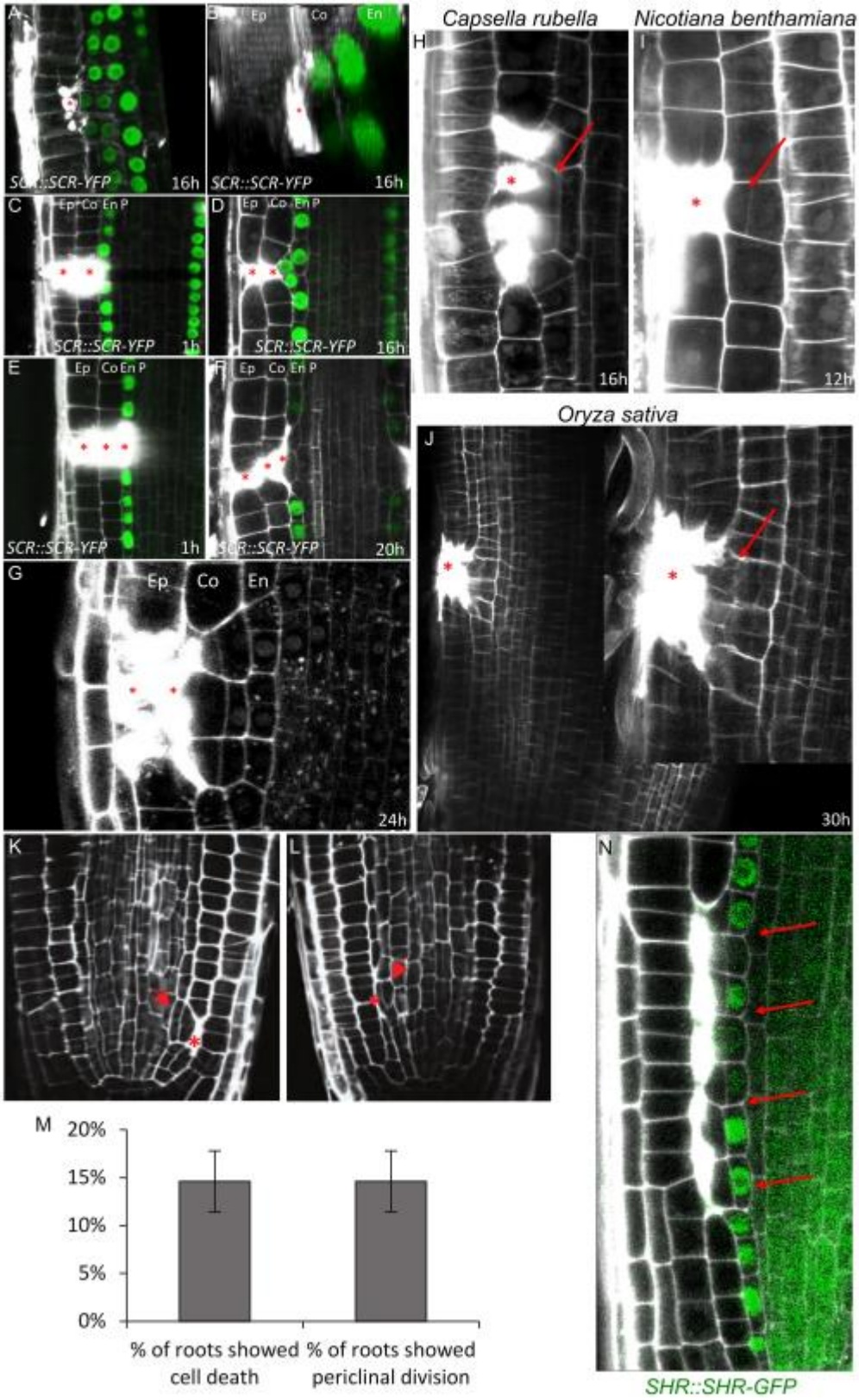


**Figure S1. Effects of non-targeted cell eliminations and single/multiple ablations in Arabidopsis and other plant species, Related to Figure 1.**

**(A** and **B)** 3D reconstruction front view **(A)** and top view **(B)** of a single ablated cortex cell followed by periclinal division of endodermal cells after 16 h.

**(C** and **D)** Multiple ablations of epidermis and cortex after 1 h **(C)** and 16 h **(D)** of ablation. Total number of ablations; n = 10-20 per cell type.

**(E** and **F)** Multiple ablations of epidermis, cortex and endodermis 1 h **(E)** and 20 h **(F)** after ablation. Total number of ablations; n = 10-20 per cell type.

**(G)** Multiple ablations of epidermis and cortex lead to repeated divisions of endodermis cells to replace eliminated cells.

**(H-J)** Single and multiple cell ablations of various cell types trigger periclinal cell divisions in inner adjacent cells in dicots *Capsella rubella* **(H)** *Nicotiana benthamiana* **(I)**, and monocot *Oryza sativa* **(J)**.

**(K** and **L)** Restorative divisions in endodermis **(K)** and pericycle **(L)** after induction of non-targeted cell death by hydroxyurea.

**(M)** Quantification of dead cells by hydroxyurea accompanied with periclinal divisions of neighboring cells. Data are represented as mean from four experiments ± SD (observed roots; n = 26, 15, 21, 41).

**(N)** Restorative divisions in endodermis after natural death of cortex cells monitored in the *SHR::SHR-GFP* marker line.

Ep: epidermis, Co: cortex, En: endodermis, P: pericycle.

Red asterisks: ablated cells, red arrows: periclinal divisions. Roots were stained with propidium iodide.

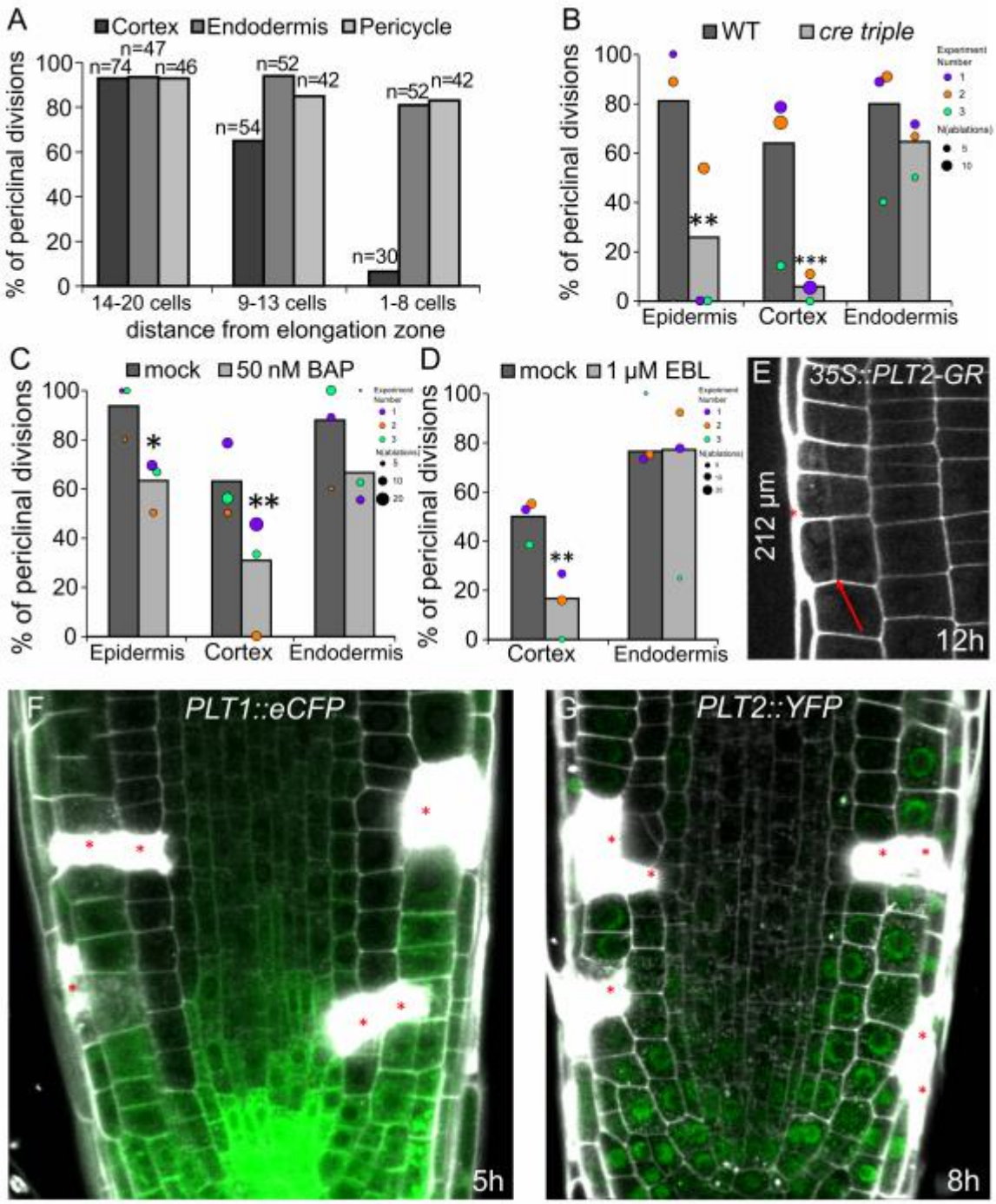


**Figure S2. Role of meristem activity and PLT expression gradient in regenerative competence, Related to Figure 2.**

**(A)** Rate of periclinal divisions depends on the distance from the meristem end to ablated meristematic cell (total number of ablations is indicated in chart).

**(B-D)** Rate of periclinal divisions 12 h after ablation in *cre1 ahk2 ahk3* triple mutants **(B),** in seedlings treated with 50 nM cytokinin (benzyl amino purine, BAP) **(C)** and with 1 µM 24-epibrassinolide (EBL) **(D)**. Data are represented as weighted mean (bar) and individual experiments (dots, area indicates sample size); asterisks indicate p-values from CLR.

**(E)** Regeneration of epidermis competence can be greatly increased by overexpression of PLT2 as LRC ablated at 212 μm distance from the QC was able to trigger periclinal cell division in epidermis 12 h after ablation.
**(F-G)** Expression patterns of *PLT1::eCFP* **(F)** and *PLT2::YFP* **(G)** were not affected by ablation of different cell types in cells undergoing restorative divisions. Red asterisks: sites of ablation, red arrows: periclinal divisions. Roots were stained with propidium iodide.

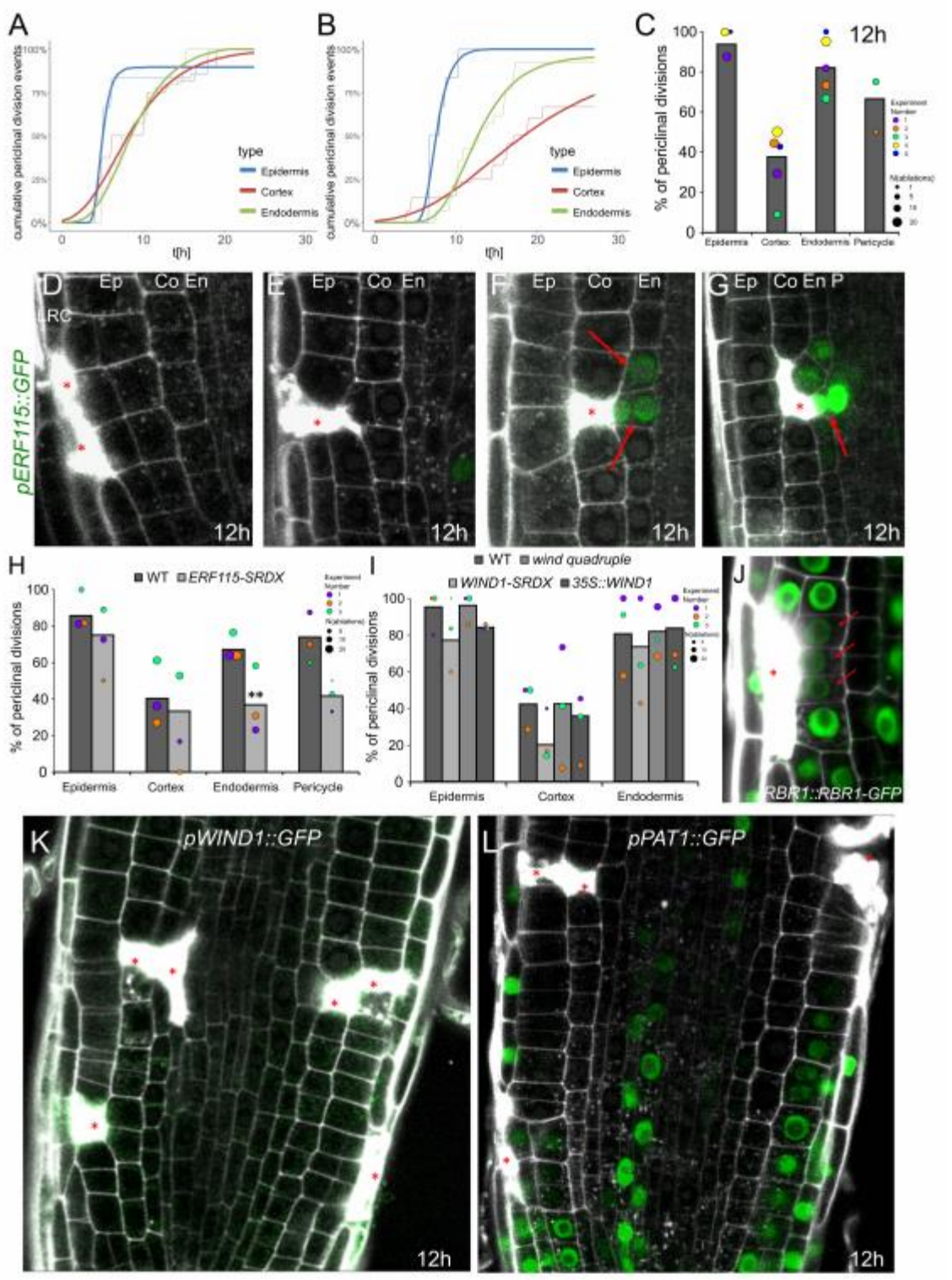


**Figure S3. Activation of cell cycle machinery triggered by ablation, Related to Figure 3.**

**(A** and **B)** Restorative division rate in cortex cells varies highly between different experiments: compare red line in **(A)**, **(B)** and Figure 3B. Cumulative periclinal division events in 10 roots with 1 ablation site per cell type each were monitored by vertical stage microscopy. Thin lines show raw data and thick lines show fitted curves calculated by least square estimates (sigmoidal curves: y=a*e^(-b*e^(-c*x))).

**(C)** Restorative division rates differ highly between cell types 12 h after ablation. Data are represented as weighted mean (bar) and individual experiments (dots, area indicates sample size)

**(D-G)** *ERF115::GFP* expression after ablation of LRC **(D)**, epidermis **(E)**, cortex **(F)** and cortex and endodermis **(G)**. Upregulation is specific to restorative divisions in endodermis and pericycle.

**(H)** Rate of periclinal divisions after ablation in *ERF115-SRDX* line. Data are represented as weighted mean (bar) and individual experiments (dots, area indicates sample size); p-values from CLR: epidermis: 0.178, cortex: 0.134, endodermis: 0.00232, pericycle: 0.129.

**(I)** Rate of periclinal divisions induced by ablation in *wind* quadruple mutants, *WIND1-SRDX* line and *35S::WIND1* line in various cells. Data are represented as weighted mean (bar) and individual experiments (dots, area indicates sample size).

**(J)** Specific downregulation of the G1/S phase transition inhibitor *RBR1::RBR1-GFP* was only observed in rare cases in inner adjacent cells prior to restorative divisions.

**(K)** Expression of *pWIND1::GFP* was not detected in roots after 12 h of ablation, during restorative division initiation.

**(L)** Expression of *pPAT1::GFP* was not upregulated after 12 h of ablation, during restorative divisions. Red asterisks: sites of ablation. Roots were stained with propidium iodide.

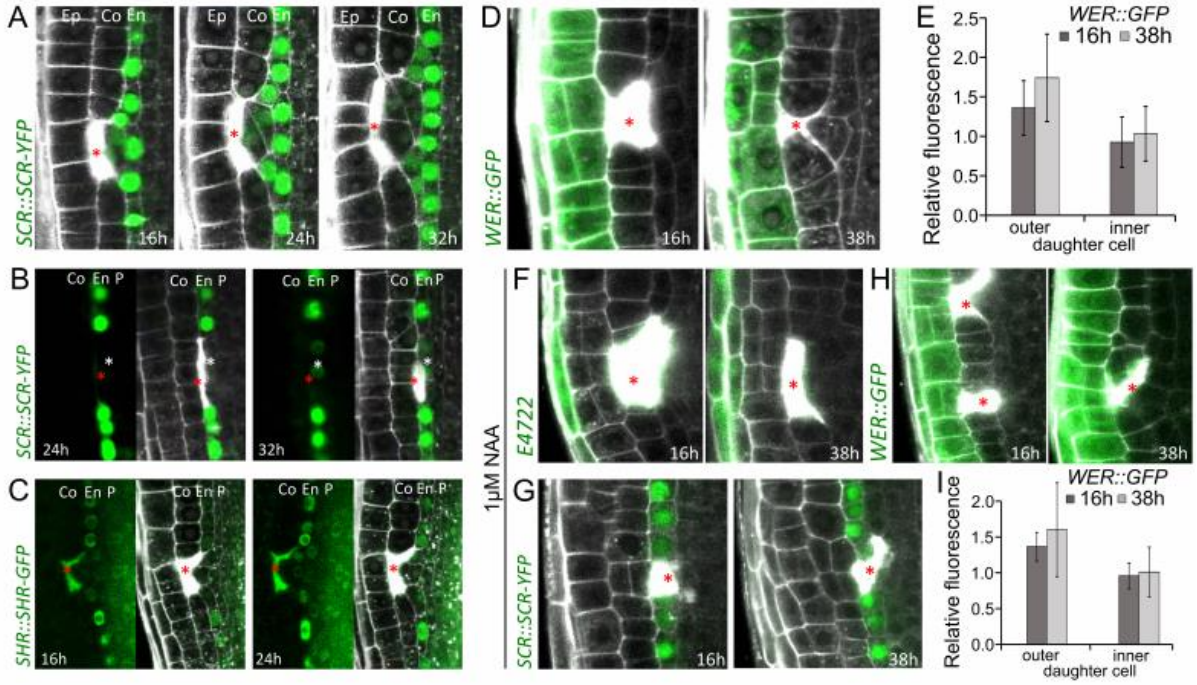


**Figure S4. Cell fates of inner and outer adjacent cells of ablation, Related to Figure 4.**

**(A)** Ablation of a cortex cell results in decreased expression of endodermis marker *SCR::SCR-YFP*. Total number of ablations; n = 42 (8 h), n = 47 (12 h), n = 95 (16 h), n = 63 (24 h), n = 47 (32 h) - see increased cortex marker *Co2::HYFP* expression in Figure 4E.

**(B** and **C)** Ablation of endodermal cell results in upregulation of *SCR::SCR-YFP* in pericycle **(B)**. Ablation of cortex and endodermis results in nuclear localization of *SHR::SHR-GFP* **(C)** in outer daughter cells of periclinally divided pericycle cells. Total number of ablations; n = 71 (16 h), n = 55 (24 h), n = 22 (32 h), n = 22 (38 h).

**(D-I)** Rarely induced restorative divisions in outer adjacent cells did not trigger cell fate change in any of the daughter cells. After 16 h and 38 h of cortex ablation, expression pattern of *WER::GFP* in outer adjacent periclinally divided daughter cells did not change **(D** and **E)**. Expression patterns of LRC marker *E4722* (**F**, 16 h; n = 52/52, 38 h; n = 43/45), *SCR::SCR-YFP* (**G**, 16 h; n = 24/24, 38 h; n = 37/37), and *WER::GFP* (**H and I**) after 16 h and 38 h of ablation did not change in the presence of 1 µM NAA, which increased occurrence of restorative divisions at the outer adjacent side. Relative fluorescence signal was calculated as follows; *WER::GFP* signals in the periclinally divided cells were divided by non-periclinally divided epidermal cells. Sample numbers are as follows; in D and E (16 h; n = 14, 38h; n = 9), in H and I (16 h; n = 10, 38h; n = 7). The error bars show SD.

Red asterisks: sites of ablation. Roots were stained with propidium iodide.

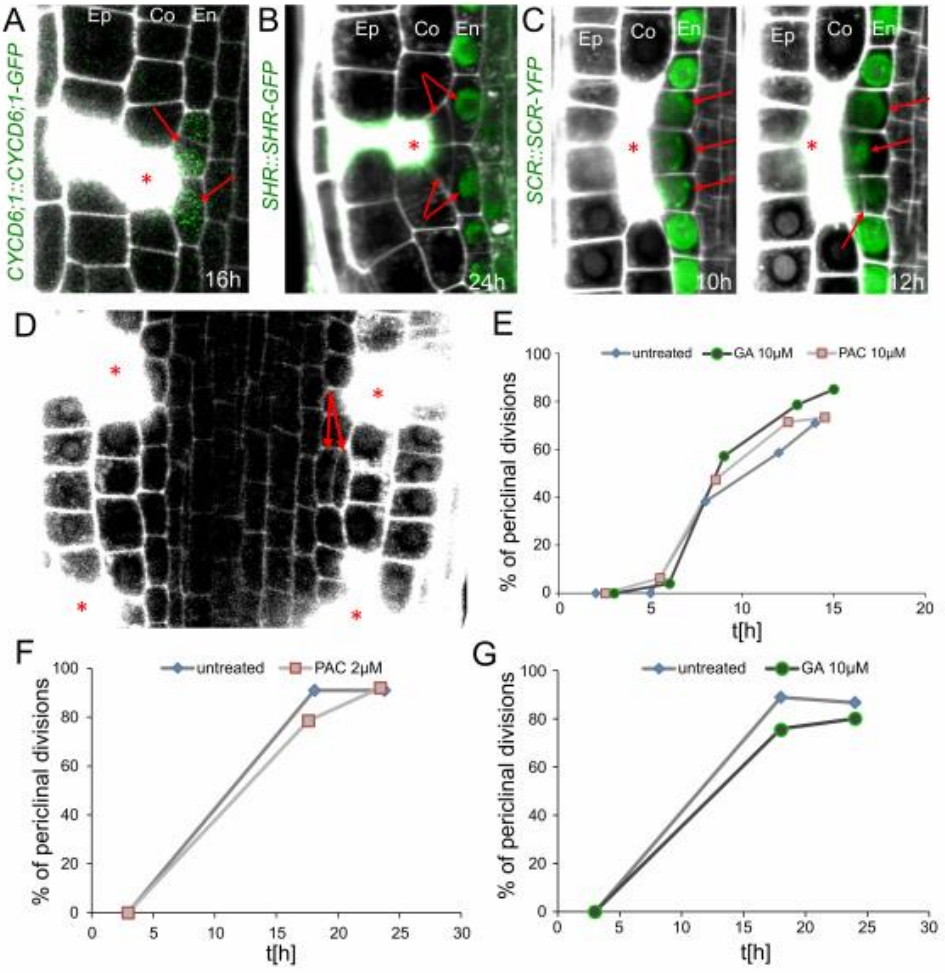

**Figure S5. Periclinal divisions in endodermis are independent of GA inducible activation of middle cortex formation, Related to Figure 5.**

**(A)** Ablation of cortex is followed by upregulation of *CYCD6;1* translational fusion before induction of periclinal division in the inner adjacent endodermis cells.

**(B** and **C)** After cortex ablation, downregulation of *SHR::SHR-GFP* is followed by induction of periclinal division in endodermis cells outside of the stem cell niche **(B)**, which is similar to downregulation of *SCR::SCR-YFP* in endodermal cells undergoing periclinal divisions **(C)**.

**(D)** Treatment of 10 µM GA resulted in ectopic inductions of periclinal divisions which are independent from cortex ablations as seen in root meristem 1 h after ablation. Note that the periclinal division is not adjacent to ablations (red arrows).

**(E-G)** Effect of GA or PAC on the rate of periclinal divisions in endodermis. For the short-term observation, 10 µM GA and PAC **(E),** for the long-term observation, 2 µM PAC **(F)** and 10 µM GA **(G)** were used. There is no influence of the treatments on the division rates in endodermis cells. Total number of ablations; n = 30-40 per treatment.

Red asterisks: sites of ablation. Roots were stained with propidium iodide.

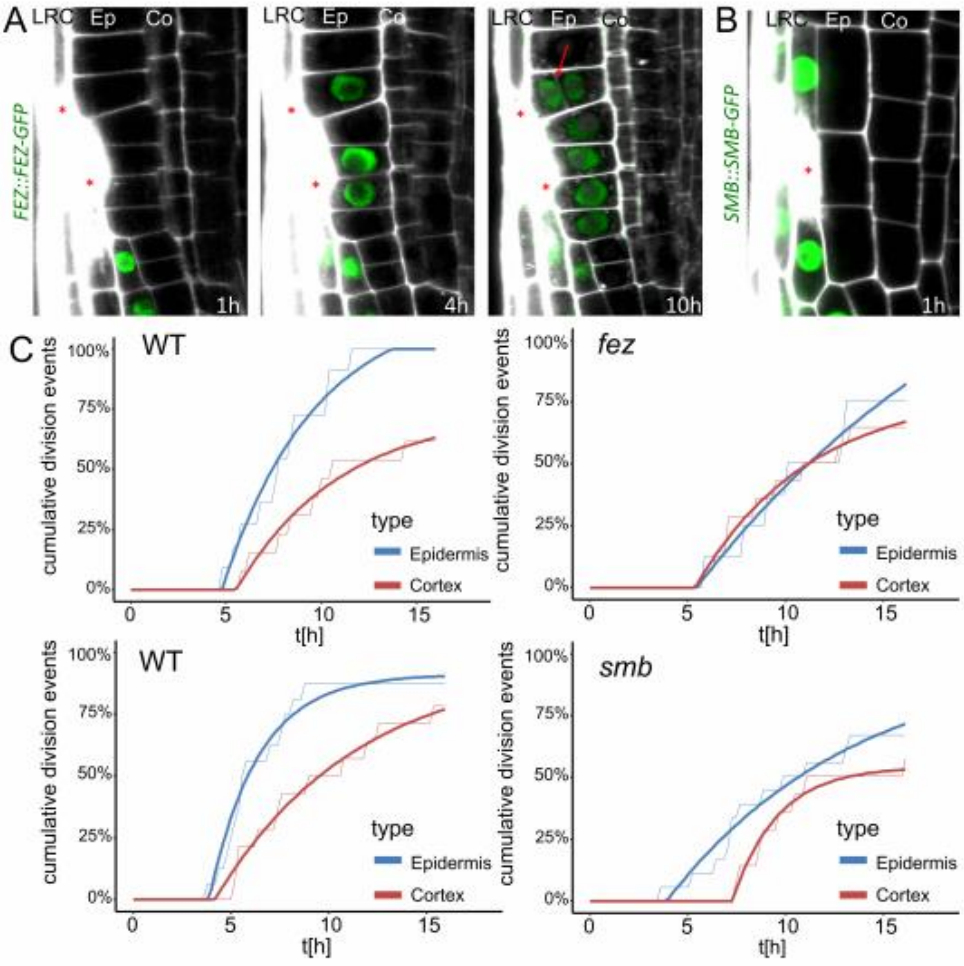

**Figure S6. Periclinal divisions in epidermis require functional FEZ/SMB module, Related to Figure 6.**

**(A** and **B)** Additional time points for the ablations shown in Figure 5B and 5C. While expression of *FEZ::FEZ-GFP* **(A)** and *SMB::SMB-GFP* **(B)** is absent from epidermis cells outside of the stem cell niche, they are upregulated in the adjacent epidermis cells after ablation of LRC cells, which gradually triggers periclinal divisions.

**(C)** Rate of periclinal division in cortex cells remains unchanged in mutants, while rates of periclinal divisions in epidermis decreased as can be seen in cumulative division events over time. Observed roots; n = 10 with 2 ablation sites per genotype; exponential curves: y=a-b*e^(c*x). Thin lines show raw data and thick lines show fitted curves calculated by least square estimates.

Red asterisks: sites of ablation. Roots were stained with propidium iodide.

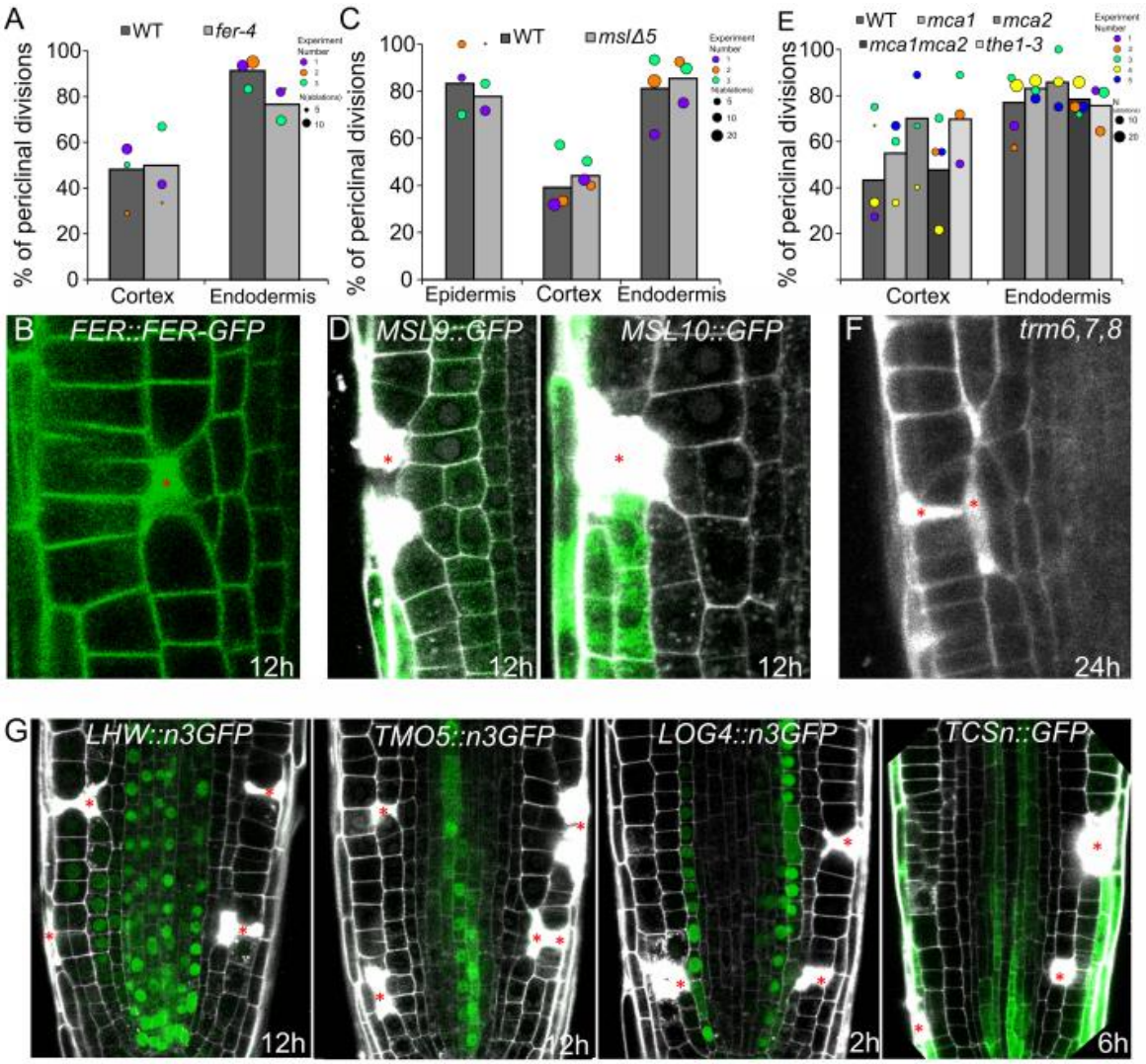


**Figure S7. Role of known components for mechanosensing, induction of periclinal division, and preprophase band during restorative divisions, Related to Figure 1.**

**(A-E)** Known mechanosensors FERONIA (FER), MECHANOSENSITIVE SMALL CONDUCTANCE-LIKE channels (MSLs), MID1-COMPLEMENTING ACTIVITY channels (MCAs) and THESEUS1 (THE1) are not involved in restorative cell divisions. **(A)** Quantification of periclinal divisions in *fer-4* mutants 12 h after ablation. Data are represented as weighted mean (bar) and individual experiments (dots, area indicates sample size). **(B)** Expression pattern of *FER::FER-GFP* during restorative division is unchanged. Autofluorescence from PI staining marks dead cells in the GFP channel. **(C)** Quantification of periclinal divisions 12 h after ablation in *mslΔ5* quintuple mutants. Data are represented as weighted mean (bar) and individual experiments (dots, area indicates sample size). **(D)** Expression of *MSL9::MSL9-GFP* (left) and *MSL10::MSL10-GFP* (right) in the *mslΔ5* background did not change during restorative divisions. **(E)** Quantification of periclinal divisions 12 h after ablation in *mca1, mca2, mca1mca2, the1-3* mutants. Data are represented as weighted mean (bar) and individual experiments (dots, area indicates sample size).

**(F)** PPB does not define the cortical division site (CDS) in restorative divisions. *trm6trm7trm8* triple mutant, which lacks the PPB, does not display defects in deposition of periclinal cell walls in long term imaging (24 h) during vertical stage experiments.

**(G)** Positive regulators of periclinal cell division LONESOME HIGHWAY (LHW), TARGET OF MONOPTEROS5 (TMO5), their downstream targets LONELY GUY4 (LOG4) and cytokinin-responsive TCS are not involved in restorative divisions in multiple cell types as can be seen in: *pLHW::n3GFP*, *pTMO5::n3GFP*, *pLOG4::n3GFP* and *pTCSn::GFP* (from left to right) at indicated time points.

Red asterisks: sites of ablation. Roots were stained with propidium iodide.

# STAR METHODS

## CONTACT FOR REAGENT AND RESOURCE SHARING

Further information and requests for resources and reagents should be directed to and will be fulfilled by the Lead contact Jiří Friml (jiri.friml@ist.ac.at).

## EXPERIMENTAL MODEL AND SUBJECT DETAILS

### Plant material

*Arabidopsis thaliana* (L.) Heynh (accession Columbia-0), *Nicotiana benthamiana, Capsella rubella* and *Oryza sativa* were used in this work. The transgenic *Arabidopsis thaliana* lines and mutant lines were described previously: *cre1-12 ahk2-2 ahk3-3* (Higuchi et al., 2004), *plt1-4* and *plt2-2* (Aida et al., 2004), *plt1plt2* (Blilou et al., 2005), *35S::PLT2-GR, PLT1::ECFP, PLT2::YFP* (Galinha et al., 2007), *HTR2::CDT1a-GFP* (Yin et al., 2014), *pCYCB1;1::GFP* line (Ubeda-Tomás et al., 2009), *KN::GFP-KN* (Reichardt et al., 2007), *SCR::SCR-YFP* and

*Co2::HYFP* (Heidstra et al., 2004), *SHR::SHR-GFP* (Nakajima et al., 2001), *J0571* (Haseloff, 1999), *WER::GFP* (Lee and Schiefelbein, 1999), *shr1* (Benfey et al., 1993b), *scr-3* (Fukaki et al., 1996), *RBR1::RBR1-GFP* and *E2FA::E2FA-GFP* (Magyar et al., 2012), *ERF115::GFP-NLS, PAT1::GFP-NLS* (Heyman et al., 2016), *ERF115-SRDX* (Heyman et al., 2013), *CYCD2;1::CYCD2;1:GFP* (Sanz et al., 2011), *WIND1::GFP, wind1wind2wind3wind4, 35S::WIND1-SRDX, 35S::WIND1* (Iwase et al., 2011) *SMB::SMB-GFP*, *FEZ::FEZ-GFP*, *fez-1* and *smb-1* (Willemsen et al., 2008), *CYCD6;1::GFP* (Sozzani et al., 2010), E4722 (http://enhancertraps.bio.upenn.edu; Gifford et al., 2008), *fer-4* (Duan et al., 2010), *msl4msl5msl6msl9msl10* (*mslΔ5*), *MSL9::GFP-GUS/mslΔ5, MSL10::GFP-GUS/mslΔ5* (Haswell et al., 2008), *mca1, mca2, mca1mca2* (Yamanaka et al., 2010), *the1-3* (Hématy et al., 2007), *FER::FER-GFP* (Li et al., 2015), *trm6trm7trm8* (Schaefer et al., 2017), *TMO5::n3GFP, LHW::n3GFP* (De Rybel et al., 2013), *LOG4::n3GFP* (De Rybel et al., 2014) *TCSn::GFP* (Zürcher et al., 2013).

**Growth conditions**

Seeds of *A. thaliana* were sown on Murashige and Skoog (1/2MS) medium (Duchefa) with 1% sucrose and 0.8% - 1% agar, stratified for 2 d and grown for 4-7 d at 21°C in a 16 h light/8 h dark cycle.

**METHOD DETAILS**

**Pharmacological treatments**

Seedlings were transferred on solid MS medium with the indicated chemicals: propidium iodide (PI, 10 µM, Sigma-Aldrich or Thermofisher), hydroxyurea (HU, final concentration 5 mM, Sigma-Aldrich) for 24 hours, gibberellic acid (GA, final concentration 10 µM, Sigma-Aldrich) for 1 hour before ablation, paclobutrazol (PAC, final concentration 2 or 10 µM as indicated, Sigma-Aldrich) for 1 hour before ablation, epibrassinolide (EBL, Sigma Aldrich, final concentration 1 µM) for 1 hour before ablation, dexamethasone (DEX, Sigma Aldrich, final concentration 5 µM) for 1 hour before ablation, 1-Naphthylacetic acid f (NAA, Sigma Aldrich, final concentration 1 µM) or 1 hour before ablation, 6-Benzylaminopurine (BAP, Sigma Aldrich, final concentration 50 nM) for 1 hour before ablation.

**Sample preparation**

Seedlings were placed on chambered cover glass (VWR, Kammerdeckgläser, Lab-Tek™, Nunc™ - eine kammer, catalog number: 734-2056) as described (Marhavý and Benková,

2015). Using the chamber, we cut out the block of solid MS media, added propidium iodide on it, let it soak, transferred 10-15 seedlings on it and put them together to a chamber.

**Confocal imaging and image processing**

Confocal imaging was performed with Zeiss LSM700/800 inverted microscopes or Leica SP5 upright microscope. Pictures were taken by 20x or 40x objectives. Fluorescence signals for GFP (excitation 488 nm, emission 507 nm), YFP (excitation 514 nm, emission 527 nm) and PI (excitation 536 nm, emission 617 nm) were detected. Samples were observed after 16 hours of ablation or at indicated time points. Images were analyzed using the ImageJ (NIH; http://rsb.info.nih.gov/ij) and Zeiss Zen 2011 software. Where necessary, images were processed using the 'sharpen' tool to produce clearer images of cellular organization.

**Vertical stage microscopy and root tracking**

Vertical stage microscopy for long-term tracking (usually 24 hours) of root meristems was performed as described (von Wangenheim et al., 2017). Roots were imaged with a vertically positioned LSM700 inverted confocal microscope and Zeiss Zen 2011 software with 20x objective and detection of PI, GFP (see above) and transmitted light. For observation of the whole root meristem, z-stacks of 42 µm were set accordingly. For the root-tracking, the TipTracker MATLAB script was used with default settings except for interval duration 720 seconds (12 minutes) and number of time points 120. The resulting images were concatenated and analysed using ImageJ.

**UV laser ablation setup**

The UV laser ablation setup is based on the layout published in ref. (Colombelli et al., 2004) and also described in ref. (Marhavý et al., 2016) that uses a passively Q-switched solid-state 355-nm UV-A laser (Powerchip, Teem Photonics) with a pulse energy of 15 µJ at a repetition rate of 1 kHZ. With a pulse length of <350 psec, a peak power of 40 kW was obtained, of which typically <5% was used to cut tissue. The power was modulated with an acousto-optic modulator (AOM; Pegasus Optik, AA.MQl l0-43-UV). The laser beam diameter matched the size of the back aperture of the objectives by means of a variable zoom beam expander (Sill Optics), enabling diffraction-limited focusing while maintaining high transmission for objectives with magnifications in the 20× to 100× range. Point scanning was realized with a pair of high-speed galvanometric mirrors (Cambridge Technology, Lightning DS). To this end, the scanning mirrors were imaged into the image plane of the rear port of a conventional

inverted microscope (Zeiss, Axio Observer Z1) with a telecentric f-θ objective (Jenoptik). To facilitate adjusting parfocality between the cutter and the spinning disk and compensate for the offset between the positions of the back planes of different objectives, the scan mirrors and the scan optics were mounted on a common translation stage. In the microscope reflector cube, a dichroic mirror reflected the UV light onto the sample but transmitted the fluorescence excitation and emission light. A UV-blocking filter in the emission path protected the camera and enabled simultaneous imaging and ablation. The AOM, the galvanometric mirrors, and a motorized stage (ASI, MS 2000) with a piezo-electric actuator on which the sample was mounted were computer controlled by custom-made software (Labview, National Instruments), enabling three-dimensional cuttings. The maximum field size for diffraction-limited cutting with little geometric distortion, high homogeneity of the intensity, and good field flatness was 300 × 300 m² for a 40× objective. The maximum depth was limited by the free-working distance of the objective used and the travel of the piezo-actuator (100 μm).

**QUANTIFICATION AND STATISTICAL SIGNIFICANCE**

For counting the PD events, at each ablation site, the occurrence of a periclinal division (marked by a division plane parallel or oblique to the growth axis) in any of the adjacent inner cells was recorded as 1/1 or 0/1 in case of only anticlinal divisions occurring.

The binary outcome “Periclinal division happened yes/no” of the ablations experiments was by definition distributed in a binomial manner, hence statistical tests for binary values are required. Based on the observation that periclinal division rates varied highly between different experiments but trends of lower division rates between mutants/treatments and controls were always visible within single experiments, we decided to opt for a statistical test that accounts for paired data sets (paired within individual experiments). Hence, the statistical significance was evaluated with conditional logistic regression (CLR) after ref. (Kleinbaum, D. G., & Klein, M., 2010). and ref. (Campbell, M. J., 2006). “Periclinal division happened” was used as binary input for each observed ablation site in the clogit function from the R package “survival”. Data was paired with experiment number as stratum. We assume that external factors such as daytime, growth medium batch and propidium iodide batch are major causes for variations between experiments.

In the case of vertical stage microscopy with root tracking, division events were counted by marking the time point at which a new cell wall (stained by propidium iodide) appeared in the first, inner adjacent cell of the ablation site. For ablations, only periclinal divisions (vertical

cell walls) were counted whereas for the virtual ablations both anticlinal and periclinal divisions were quantified. The virtual ablation sites were arbitrarily chosen similar as in the laser ablation experiments and the division events were counted on videos after registration (correct 3D drift tool in ImageJ). The percentage of cumulative division events over time was plotted using the R studio. Non-linear regression curves for each experiment were calculated using the nlsLM function of the R package "minipack.lm" assuming an asymmetric sigmoidal (y=a *e^(-b*e^(-c*x))) or exponential (y=a-b*e^(c*x)) behavior with arbitrarily chosen starting parameters. The calculated final parameters with lowest residual sum-of-squares were chosen to determine the first derivation of the fitted curves to estimate the probability of division events over time.

Asterisks illustrate the p-value: $p < 0.001$ is ***, $p < 0.01$ is ** and $p < 0.05$ is *

Number of repetitions and replicates are mentioned for each experiment in the legends.

## KEY RESOURCES TABLE

| REAGENT or RESOURCE | SOURCE | IDENTIFIER |
|---|---|---|
| Chemicals, Peptides, and Recombinant Proteins | | |
| Propidium iodide | Sigma-Aldrich | Cat#P4864 |
| Propidium iodide | Thermo Scientific | Cat#P3566 |
| Hydroxyurea | Sigma-Aldrich | Cat#H8627 |
| Gibberellic acid | Sigma-Aldrich | Cat#G7645 |
| Paclobutrazol | Sigma-Aldrich | Cat#46046 |
| Epibrassinolide | Sigma-Aldrich | Cat#E1641 |
| Dexamethasone | Sigma-Aldrich | Cat#D1756 |
| 1-Naphthylacetic acid | Sigma-Aldrich | Cat#N0640 |
| 6-Benzylaminopurine | Sigma-Aldrich | Cat#B3408 |
| Experimental Models: Organisms/Strains | | |
| *Arabidopsis:* WT Col-0 | https://www.ncbi.nlm.nih.gov/Taxonomy/Browser/wwwtax.cgi | NCBI:txid3702 |
| *Capsella rubella* | https://www.ncbi.nlm.nih.gov/Taxonomy/Browser/wwwtax.cgi | NCBI:txid81985 |
| *Nicotiana benthamiana* | https://www.ncbi.nlm.nih.gov/Taxonomy/Browser/wwwtax.cgi | NCBI:txid4100 |
| *Oryza sativa* | https://www.ncbi.nlm.nih.gov/Taxonomy/Browser/wwwtax.cgi?mode=Info&id=4530&lvl=3&lin=f&keep=1&srchmode=1&unlock | NCBI:txid4530 |
| *Arabidopsis: cre1-12 ahk2-2 ahk3-3* | Higuchi et al., 2004 | Cross between *cre1-12* (SALK_048970), *ahk2-2* and *ahk3-3* (SALK_069269) |
| *Arabidopsis: plt1-4, plt2-2* | Aida et al., 2004 | N/A |

| | | |
|---|---|---|
| *Arabidopsis: plt1plt2* | Blilou et al., 2005 | Cross between *plt1-4* and *plt2-2* |
| *Arabidopsis: wind1wind2wind3wind4* | Iwase et al., 2011 | Cross between wind1 (SALK_027272), wind2 (SALK_139727), wind3 (SALK_091212) and wind4 (SALK_099481) |
| *Arabidopsis: shr1* | Benfey et al., 1993 | NASC ID: N3997 |
| *Arabidopsis: scr-3* | Fukaki et al., 1996 | NASC ID: N3997 |
| *Arabidopsis: fez-1*, *smb-1* | Willemsen et al., 2008 | N/A |
| *Arabidopsis: fer-4* | Duan et al., 2010 | GK-106A06 |
| *Arabidopsis: msl4msl5msl6msl9msl10* (*mslΔ5*) | Haswell et al., 2008 | Cross between *msl4-1* (SALK_142497), *msl5-2* (SALK_127784), *msls6-1* (SALK_06711), *msl9-1* (SALK_114626), *msl10-1* (SALK_076254) |
| *Arabidopsis: mca1, mca2* | Yamanaka et al., 2010 | *mca1* (N/A) *mca2* (SALK_129208) |
| *Arabidopsis: mca1mca2* | Yamanaka et al., 2010 | Cross between *mca1* and *mca2* |
| *Arabidopsis: the1-3* | Hématy et al., 2007 | FLAG_201_C06 |
| *Arabidopsis: trm6trm7trm8* | Schaefer et al., 2017 | Cross between *trm6-1* (GK_048G03), *trm7-1* (SALK_074058), *trm8-1* (SALK_150274) |
| *Arabidopsis: 35S::PLT2-GR, PLT1::ECFP, PLT2::YFP* | Galinha et al., 2007 | Transgenic Col-0 |
| *Arabidopsis: HTR2::CDT1-GFP* | Yin et al., 2014 | Transgenic Col-0 |
| *Arabidopsis: CycB1;1::GFP* | Ubeda-Tomás et al., 2009 | Transgenic Col-0 |
| *Arabidopsis: KN::GFP-KN* | Reichardt et al., 2007 | Transgenic Ler/Nd |
| *Arabidopsis: SCR::SCR-YFP, Co2::HYFP* | Heidstra et al., 2004 | Transgenic N/A |
| *Arabidopsis: SHR::SHR-GFP* | Nakajima et al., 2001 | Transgenic Col-0 |
| *Arabidopsis: J0571* | Haseloff, 1999 | NASC ID: N9094 |
| *Arabidopsis: WER::GFP* | Lee and Schiefelbein, 1999 | NASC ID: N66493 |
| *Arabidopsis: RBR1::RBR1-GFP* | Magyar et al., 2012 | Transgenic Col-0 |
| *Arabidopsis: ERF115::GFP-NLS, PAT1::GFP-NLS* | Heyman et al., 2016 | Transgenic Col-0 |
| *Arabidopsis: ERF115-SRDX* | Heyman et al., 2013 | Transgenic Col-0 |
| *Arabidopsis: CYCD2;1::CYCD2;1:GFP* | Sanz et al., 2011 | Transgenic Col-0 |
| *Arabidopsis: WIND1::GFP, 35S::WIND1-SRDX, 35S::WIND1* | Iwase et al., 2011 | Transgenic Col-0 |
| *Arabidopsis: SMB::SMB-GFP*, *FEZ::FEZ-GFP* | Willemsen et al., 2008 | Transgenic Col-0 |
| *Arabidopsis: CYCD6;1::GFP* | Sozzani et al., 2010 | Transgenic Col-0 |
| *Arabidopsis: E4722* | Gifford et al., 2008 | NASC ID: N70265 |
| *Arabidopsis:MSL9::GFP-GUS/mslΔ5, MSL10::GFP-GUS/mslΔ5* | Haswell et al., 2008 | Transgenic Col-0 |
| *Arabidopsis: FER::FER-GFP/fer-4* | Li et al., 2015 | Transgenic Col-0 |
| *Arabidopsis: TMO5::n3GFP, LHW::n3GFP* | De Rybel et al., 2013 | Transgenic Col-0 |
| *Arabidopsis: LOG4::n3GFP* | De Rybel et al., 2014 | Transgenic Col-0 |
| *Arabidopsis: TCSn::GFP* | Zürcher et al., 2013 | NASC ID: N69180 |
| Software and Algorithms | | |
| imageJ | https://imagej.net/ | RRID:SCR_003070 |
| Zeiss Zen 2011 | www.zeiss.com | N/A |

| | | |
|---|---|---|
| R project | http://www.r-project.org/ | RRID:SCR_001905 |
| R-studio | http://www.rstudio.com/ | RRID:SCR_000432 |
| ggplot2 | http://ggplot2.org/ | RRID:SCR_014601 |
| survival | https://cran.r-project.org/web/packages/survival/survival.pdf | N/A |
| minipack.lm | https://www.rdocumentation.org/packages/minpack.lm/versions/1.2-1/topics/nlsLM | N/A |
| TipTracker | https://doi.org/10.7554/eLife.26792.022 | N/A |

# Chapter 3:

## Wounding-induced changes in cellular pressure and localized auxin signalling spatially coordinate restorative divisions in roots

Lukas Hoermayer[1], Juan Carlos Montesinos[1], Petra Marhava[1,2], Eva Benková[1], Saiko Yoshida[1,3] and Jiří Friml[1]

1 Institute of Science and Technology Austria, 3400 Klosterneuburg, Austria

2 Current address: University of Lausanne, DBMV, CH-1015 Lausanne, Switzerland

3 Current address: Max Planck Institute for Plant Breeding Research, 50829 Carl-von-Linné Weg 10, Cologne, Germany

Published in

Proc Natl Acad Sci U S A. 2020 Jun 30; 117(26): 15322–15331.

**Abstract**

Wound healing in plant tissues, consisting of rigid cell wall-encapsulated cells, represents a considerable challenge and occurs through largely unknown mechanisms distinctive from animals. Owing to their migration inability, plant cells rely on targeted cell division and expansion to regenerate wounds. Strict coordination of these wound-induced responses is essential to ensure efficient, spatially restricted wound healing. Single cell tracking by live imaging allowed us to gain mechanistic insights into the wound perception and coordination of wound-responses after laser-based wounding in *Arabidopsis* root. We revealed a crucial contribution of the collapse of damaged cells in wound perception and detected an auxin increase specific to cells immediately adjacent to the wound. This localized auxin increase balances wound-induced cell expansion and restorative division rates in a dose-dependent manner, leading to tumorous overproliferation when the canonical TIR1 auxin signalling is disrupted. Auxin and wound-induced turgor pressure changes together also spatially define the activation of key components of regeneration, as the transcription regulator ERF115. Our observations, hence suggest that the wound signalling involves the sensing of collapse of damaged cells and a local auxin signalling activation to coordinate the downstream transcriptional responses in the immediate wound vicinity.

**Significance Statement**

Plants are sessile organisms that cannot evade wounding or pathogen attack and their cells are encapsulated within cell walls making it impossible to use cell migration for wound healing like animals. Hence, regeneration in plants largely relies on the coordination of targeted cell expansion and oriented cell division. Here we show in the root that the major growth hormone auxin is specifically activated in wound-adjacent cells, regulating cell expansion, cell division rates and the regeneration-involved transcription factor ERF115. These wound responses depend on cell collapse of the eliminated cells presumably perceived by the cell damage-induced changes in cellular pressure. This largely broadens our understanding how wound responses are coordinated on a cellular level to mediate wound healing and prevent overproliferation.

## Introduction

Plant cells are encapsulated by their rigid cell walls; hence, tissue regeneration in plants relies mainly on oriented cell divisions, directional cell elongation and acquisition of new cell fates (1–4). Recently, we have shown that ablation of small groups of cells in the root meristem can be used to study wounding responses and regeneration *in vivo* and on a single cell level (5). These studies revealed that wounding triggers restorative cell divisions predominately in cells at the inner adjacent side of the eliminated cells. The accelerated divisions deposit new cell walls parallel to the wound area (usually in a periclinal orientation) and the newly generated daughter cells subsequently acquire the cell fate of the removed cells as they fill the wound. This process depends on the re-activation of stem cell components and division plane switch in these cells. Other recent studies utilizing the single cell ablation method investigated early wound responses in the root implicating calcium signalling, immune peptide activation, jasmonate and ethylene signalling (6–8).

A key component of the wound response is the transcription factor ETHYLEN-RESPONSIVE 115 (ERF115), which is usually not expressed in the root meristem but its expression is activated after wounding in close vicinity to the damaged tissue. ERF115 heterodimeric binding to different transcription factors induces downstream transcriptional reprograming leading to dedifferentiation and proliferation (9, 10). Activation of ERF115 expression has been linked in different contexts to multiple signals including brassinosteroids, jasmonic acid, auxin and reactive oxygen species (6, 9, 11, 12). Although many of these upstream regulations have been implied, what defines the strict ERF115 spatial and temporal expression pattern remain elusive.

Auxin, a classical phytohormone, besides its key role in many aspects of plant growth and development has been also proposed to be important in tissue and organ restoration during regeneration as it accumulates after amputation of the root tip above the wound and crucially contributes to the regeneration processes (13, 14). Also during undisturbed development, auxin is involved in orienting cell division planes, in cell fate (re)specification and the maintenance of the root stem cell niche (15–17); all processes essential for tissue regeneration. Despite these indications, a specific role for auxin in wound healing and local tissue restoration has not been shown.

Here we show a local increase of auxin signalling specifically in wound-adjacent cells later undergoing restorative divisions. We have identified a dual mode of action for auxin in wound-responsive cell division and expansion rates. Auxin, via its canonical, nuclear

signalling, regulates cell division and ERF115 expression, both promoting and inhibiting the wound-responses in a dose-dependent manner. Finally, we show that ERF115 expression and wound-responsive cell division are linked spatially and temporary through the perception of damaged cell collapse, indicating to a crucial role of turgor pressure and cell wall integrity perception in wound signalling.

**Results:**

**Local auxin accumulation in cells undergoing restorative division**

To observe potential changes in auxin signalling after single cell ablation, we used an auxin signalling marker, R2D2, which consists of an auxin-degradable RPS5::DII-Venus component and the stable RPS5::mDII-Tdtomato, allowing detection of increased auxin signalling (18). We used vertical growth confocal imaging coupled with live tracking (19, 20) to follow cells during regeneration over prolonged time (16 – 32 hours). We observed a downregulation of DII-Venus indicative of auxin signalling increase in wound-adjacent cells approx. 3 hours before the first division (Fig. 1; SI Appendix, Movie S1). These changes in DII were absent from neighbouring cells not adjacent to the wound in the same roots. Notably, after the first division, daughter cells that were still adjacent to the wound retained the high auxin signalling activity, while the non-adjacent daughter cells quickly regained normal auxin signalling levels (Fig. 1A, C). These dynamics were not due to any possible bleaching effects of the ablation or propidium iodide staining (SI Appendix, Fig. S1A-S1E, Movie S2&S3), and at least ~ 50% of all wound-adjacent cortex and ~20% of all wound-adjacent endodermis cells exhibited this downregulation of DII-Venus (SI Appendix, Figure S1G); altogether suggesting increased auxin signalling in cells activated by wounding.

To elucidate the source of this increased auxin signalling in the wound-adjacent cells, we performed long-term imaging of roots treated with the auxin biosynthesis inhibitors Kynurenine and Yucasin as well as the polar auxin transport inhibitor NPA (21–23). Notwithstanding the overall auxin accumulation throughout the root tip after NPA treatment, we still observed consistently DII signal downregulation specifically in the wound-adjacent cells as compared to their direct neighbours (SI Appendix, Fig. S1F, Movie S4). Wounding-induced, local increase in auxin signalling also occurred after inhibition of auxin biosynthesis (SI Appendix, Fig. S1H, Movie S5). Despite some role of these processes cannot be completely ruled out, these pharmacological manipulations suggest that auxin biosynthesis or polar transport are not major contributors to the local increase in auxin signalling during

regeneration. Other, so far unidentified auxin homeostasis processes, such as release of free auxin from conjugates may play a role.

In summary, our observation detected a local increase of auxin signalling in wound-adjacent cells; specifically those, which contribute to the regeneration process by later restorative divisions and expansion. The underlying mechanism for this elevated auxin signalling remains elusive, but it appears to be independent of both on-site auxin biosynthesis and polar auxin transport.

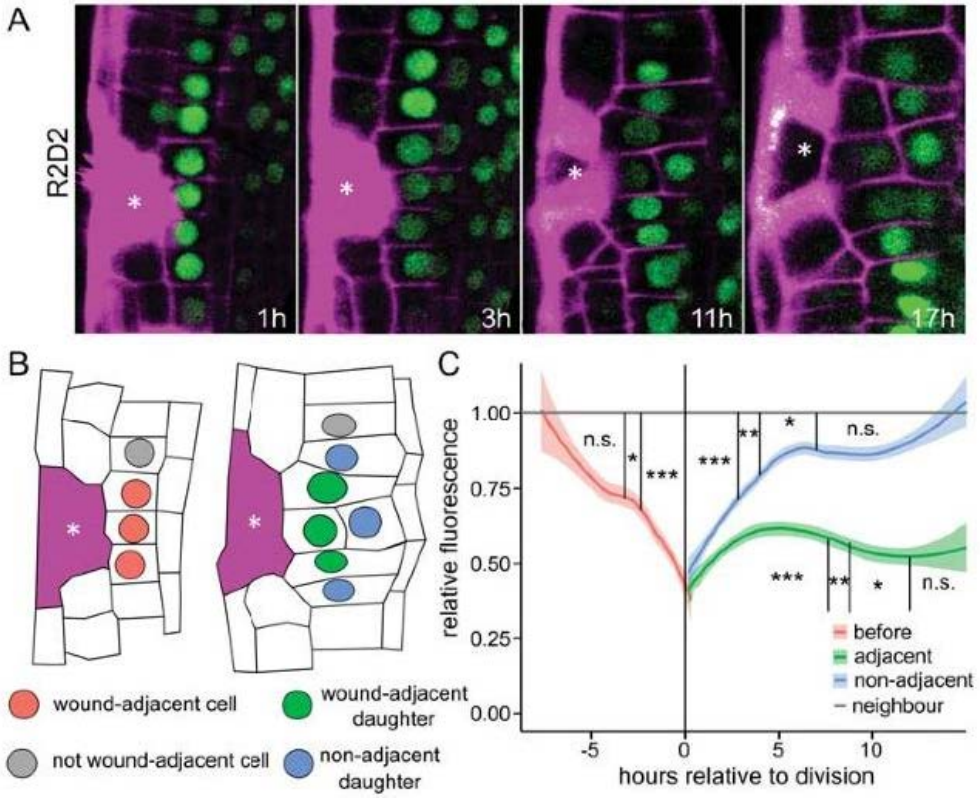


**Figure 1. Auxin signalling in wound-adjacent cells**

**(A-B)** Wound-adjacent cells exhibit increased auxin signalling compared to neighbouring cells. **(A)** DII-Venus (green) expression (of R2D2 negative auxin marker line) in cells next/adjacent to ablated cell (marked with asterisk) during 1, 3, 11 and 17 hours after cell ablation. Notice that lower DII-Venus signal indicates higher auxin signalling. Cell walls and dead cells are stained with PI (pink). **(B)** Schematic representation of wound-adjacent cells at different stages of regeneration. Ablated cell is in pink with an asterisk. **(C)** Quantification of DII-Venus fluorescence signal over time from wound-adjacent cells before (red), or after cell division (wound-adjacent in green; non-wound adjacent in blue). Data are represented as DII-Venus fluorescence in observed cells relative to neighbouring, not-adjacent cells. Time "0 h" represents time of restorative cell division. Thick lines

represent the smoothed mean and lighter background represents smoothed standard error from n=18 cells each. Statistical significance was computed from a one-sample Wilcoxon test.

---

**Dual auxin effect on regeneration efficiency**

The local increase in auxin signalling after wounding implies a role for auxin in restorative patterning. Auxin might accelerate the cell cycle progression, determine the cell division plane or the stem cell fate acquisition, the cell expansion towards the wound, or a combination of those. As reported previously (5), cortex and endodermis exhibit different rates of restorative, periclinal cell divisions after 12 hours; endodermis cells divide rapidly while cortex cells are usually slower. However, after sufficient time (over 32 hours), all ablated cells are replaced by restorative divisions of wound-adjacent cells.

To test for an auxin effect in wound regeneration, we applied synthetic auxin (1-Napthylacetic acid; NAA) 1 hour before the ablation, imaged the wounded roots 12 hours after ablation and quantified how many ablation sites triggered periclinal cell divisions in the inner adjacent cell types. These experiments revealed that NAA application increased the division rates at concentrations up to 1 µM (Fig. 2A; SI Appendix, Fig. S2A), particularly in cortex cells, which usually possess a relatively low regeneration rate in the first 12 hours. On the other hand, the already fast regeneration rate of the endodermis cells (~75%; SI Appendix, Fig. S2A) was not much further increased by auxin. To examine effects of decreased auxin levels, we treated roots with 10 µM Kynurenine and observed that roots with lower auxin levels exhibited decreased restorative division rates in all cell types, indicating again a positive auxin effect on restorative cell divisions (SI Appendix, Fig. S2C).

Nonetheless, at higher concentrations, NAA caused a decrease in division rates with 1 µM NAA representing apparently a breaking point, where two populations of auxin-treated roots were observed: (i) roots with fast and efficient regeneration similar to 250 – 500 nM treated plants or (ii) roots with strongly inhibited regeneration. The inhibitory auxin effect became more pronounced at 2 µM NAA and at 5 -10 µM NAA no regeneration occurred any more (Fig. 2A; SI Appendix, Fig. S2A). This concentration-dependent auxin effect on restorative division rates suggests a dual, both positive and negative mode of action for auxin during tissue regeneration.

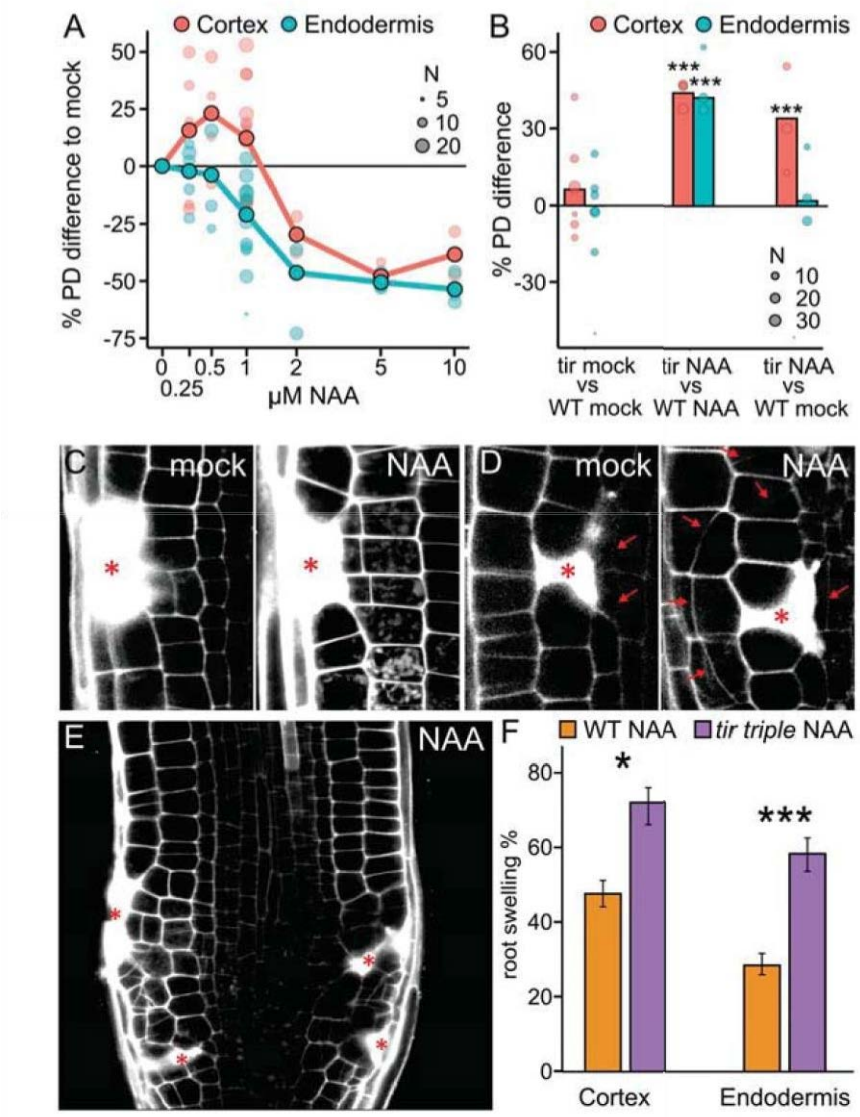


**Figure 2. Auxin effect on regeneration capacity**

**(A)** Auxin increases division rates until 1 µM and decreases wound response at higher concentrations. Quantification of restorative periclinal division rates (in %) of endodermal (blue) and cortex (red) cells, after different auxin (NAA, from 0 to 10 µM) concentration application compared to mock. Big dots represent weighted mean and lighter dots represent individual experiments (area indicates sample size).

**(B)** Auxin treated *tir triple* mutant plants have higher division rates than Wt plants. Quantification of relative restorative periclinal divisions rate (in %) of endodermal (blue) and cortex (red) cells, comparing *tir triple* mutant with Wt plants on mock, *tir triple* mutant with Wt plants upon 1 µM NAA treatment, or 1 µM NAA treated *tir triple* with Wt plants on mock. Data are represented as weighted mean difference (bar) and difference in individual experiments (dots, area indicates sample size).

**(C-D)** Auxin expands zone of wound-responsive divisions. **(C)** Restorative cortex divisions on mock (left) or upon 1 µM NAA treatment (right) after epidermal cell ablation (asterisk). **(D)** Restorative cell

divisions in outer epidermis cells on mock (left) or upon 1 μM NAA treatment (right) after cortex cell ablation (asterisk). Red arrows indicate new, oblique-periclinal cell plates.
**(E)** Restorative cell divisions after cell ablations (marked with asterisk) in Wt roots supplemented with 1 μM NAA. Notice that the increment of restorative cell divisions in these conditions induce root swelling.
**(F)** Quantification of root swelling (in %) after restorative cortex or endodermal cells division in 1 μM NAA treated Wt (orange bars) or *tir triple* (purple bars) background plants. Data are represented as ratios (bars) with error bars indicating upper and lower quartiles. Statistical significance was computed from a Chi-square test.

---

**TIR1 auxin signalling-mediated, wound-induced cell proliferation**

To investigate the signalling mechanism underlying this auxin effect, we tested NAA application on the *tir1-1 afb2-1 afb3-3* (*tir triple*) mutant, defective in auxin receptors (24, 25). Untreated *tir triple* mutants showed regeneration capacity not much different from the Wt (Fig. 2B; SI Appendix, Fig. S2B). However, treatment with 1 μM NAA, which in Wt normally inhibited divisions, in the *tir triple* it increased the restorative division rate of endodermis and cortex cells to almost maximum speed (Fig. 2B; SI Appendix, Fig. S2B); we even observed repeated divisions within 12 hours (SI Appendix, Fig. S2H). This suggests that the dual-phase effect of auxin can be differentiated into (i) an activating and (ii) an inhibitory effect on restorative divisions with at least the latter one depending on the activity of the TIR1 auxin receptors.

Besides its overall effect on the rate of restorative cell divisions, auxin also influenced the direct response of the each involved cell towards wounding. Usually, wounds of 1 -2 cells size are filled by 1 - 3 adjacent cells at the inner side of the wound, which initiate periclinal divisions (5). Auxin treatment, however, increased the area of activated cells to nearly all wound-adjacent cells. On some occasions, 4 or more cells responded to the wound by inducing restorative divisions (Fig. 2C; SI Appendix, Fig. S2D-E). Auxin also triggered ectopic periclinal cell divisions at the outer wound side, or in adjacent upper and lower cells. Usually, these cells undergo normal anticlinal divisions and do not contribute greatly to the wound healing (Marhava et al., 2019, Fig. 2D; SI Appendix, S2F-G). This auxin effect on activating more adjacent cells and at all sides also occurred in the *tir triple* mutant and are hence, likely a component of the activating auxin effect that is less dependent on TIR1/AFB-mediated auxin perception.

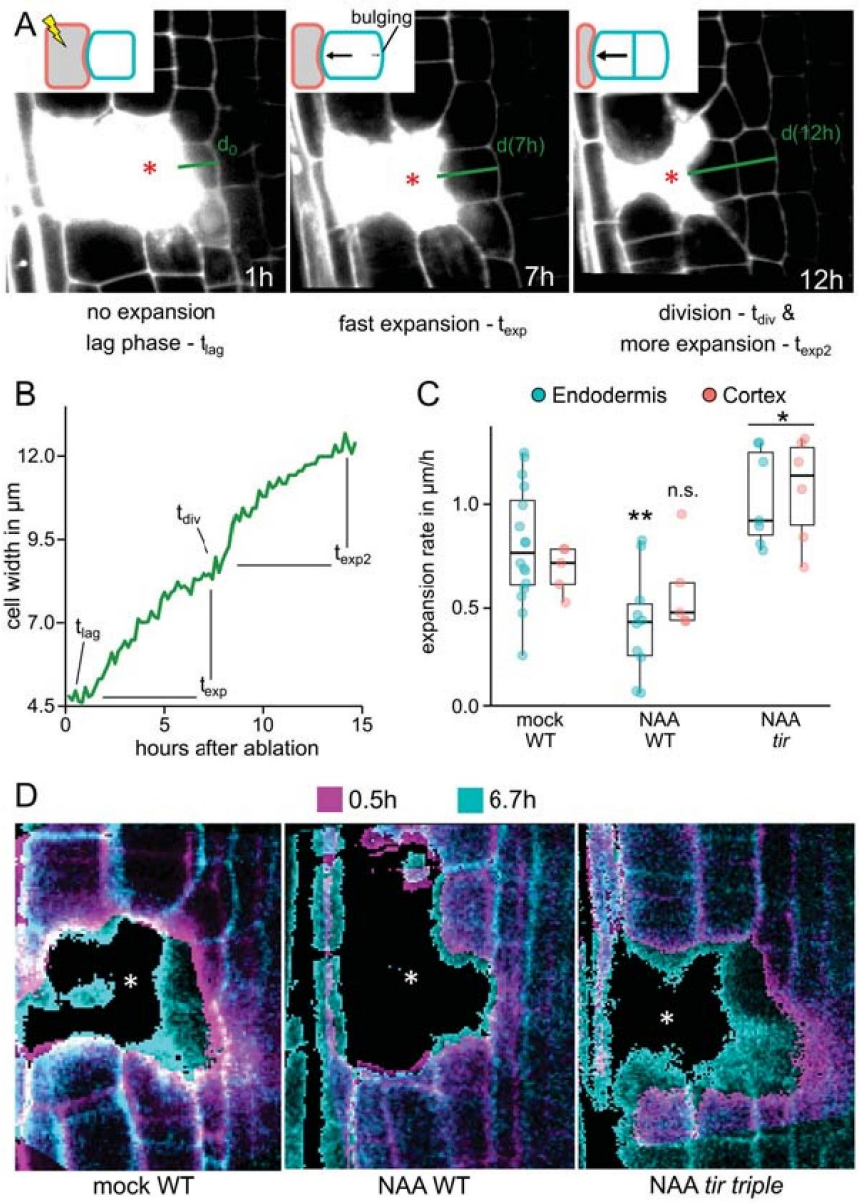


**Figure 3. Cell expansion during wound-responsive divisions**

**(A-B)** Wound-adjacent cells undergoing restorative divisions are actively expanding towards the wound before the onset of division. **(A)** Cell expansion dynamics of an endodermal cell during wounding (cortex cell ablated, asterisk). Wound-induced cell expansion in endodermis 1 hour after cell ablation (left panel), after 7 hours (middle panel) or after cell division (12 hours, right panel). **(B)** Representation of the cell width (in µm) of one representative endodermis cell during the restorative cell division stages (in hours after ablation). $t_{lag}$:0-1 hours; $t_{exp}$:1-7 hours; $t_{div}$:7-8 hours; $t_{exp2}$:8-15 hours.

**(C-D)** Pre-mitotic cell expansion during auxin treatment is decreased in Wt roots and increased in *tir triple* roots. **(C)** Representation of endodermal (blue) or cortex (red) cell expansion rate (µm/h) during restorative cell division in Wt (mock or 1 µM NAA) or in *tir triple* roots upon 1 µM NAA treatment. Data are represented as pre-mitotic expansion rates and dots indicating values from individual cells.

Statistical significance was computed from a Student's t-test. **(D)** Overlay of wound-adjacent cell width at two different time points (0.5 hours in magenta, and 6.7 hours in cyan) after ablation in Wt roots on mock (left panel) or upon 1 μM NAA treatment (middle panel), or in 1 μM NAA treated *tir* triple roots (right panel). Asterisk marks ablated cell.

---

These auxin effects on: (i) the increase in restorative division rates, (ii) the spreading of wound responses to all adjacent cells and (iii) the ectopic division plane switch from anticlinal to periclinal, manifested regularly in an overproliferation of the whole wounded area. Roots treated with 1 μM NAA sometimes contained wound-responsive cells that did not stop the periclinal cell divisions and continuously divided and expanded to overfill the induced wounds with new daughter cells. This caused a strong swelling of the root meristem (Figure 2G), which occurred in ~20-50% of Wt plants. However, in the *tir triple* mutant, most ablation sites (60-70%) triggered this strong overproliferation phenotype, likely because the TIR1 signalling-mediated, inhibitory auxin effect was reduced (Fig. 2E-F; SI Appendix, Fig. S2I).

To further test the involvement of TIR1 in this regulation, we used the synthetic CCV-TIR1 – CVX-IAA pair, where a modified auxin ligand, CVX-IAA, can only bind to a mutated form of TIR1 receptor, CCV-TIR1, but not to Wt-TIR1 (26). CVX-IAA triggered swelling only in the *CCV-TIR1* plant, but not in the Wt plants (SI Appendix, Fig. S2J).

This causally links the auxin effect on wound regeneration to the TIR1/AFB pathway and suggests that both, inhibiting and activating auxin effects are mediated by this pathway. In this view, the reduction of the inhibitory effect in the *tir triple* mutant can be explained by the overall shift in sensitivity towards higher auxin concentration due to lack of some of the TIR1/AFB auxin receptors.

**Auxin-induced cell expansion in wound regeneration**

The over-proliferated, swollen roots observed after auxin treatment are the consequence of an increased number of restorative cell division and their consequent cell expansion. Given that auxin has a well-established role in growth both in roots and shoots (27–30), we analysed cell expansion changes during wound regeneration. We performed long-term imaging experiments, in which we quantified the width of wound-adjacent cells as a proxy for cell expansion. After ablation, the size of the inner adjacent cells remained constant for a short "lag phase" ($t_{lag}$) of 0 – 4 hours, followed by a phase of rapid expansion ($t_{exp}$), for usually 10 hours in which the cells continuously grew towards the wound and bulged towards the inner

intact neighbour suggesting increased turgor pressure. The expansion paused shortly during the time of division ($t_{div}$) and continued directly afterwards ($t_{exp2}$) (Fig. 3A-B; SI Appendix, Fig. S3A-C, F, Movie S6).

Auxin treatment reduced the expansion rate in Wt endodermis cells strongly from 0.80 ± 0.3 µm/h to 0.42 ± 0.3µm/h and slightly also in cortex cells from 0.68 ± 0.1 µm/h to 0.58 ± 0.2µm/h (Fig. 3C-D; SI Appendix, Fig. S3D, S4A-C). The decreased expansion rates lead to a delay in cell size increase, which correlated with the decreased speed of restorative division induction (SI Appendix, Fig. S3E). In contrast, auxin treatment in the *tir triple* mutant strongly increased expansion in both endodermis (1.0 ± 0.2µm/h) and cortex (1.1 ± 0.3µm/h) (Fig. 3C-D; SI Appendix, Fig. S3D, S4B-D) again correlating with higher rate of regeneration in these conditions. These observations collectively suggest that cell expansion is an important component of regeneration after wounding correlating this process.

Notably, wound-adjacent cells in untreated Wt plants exhibited stable cell expansion rates, which decreased only during mitosis. In contrast, cell expansion in auxin treated *tir triple* cells strongly fluctuated: phases of extremely high expansion (2 µm/h) were followed by a complete collapse (< 0.5 µm/h) far before onset of mitosis (SI Appendix, Fig. S4E). Steady cell expansion usually requires coordination of cell wall properties and turgor pressure, suggesting that this may be uncoupled in the case of *tir triple* on 1 µM NAA.

In summary, we observed that cell expansion correlates strongly with induction of regenerative divisions. Auxin has a similar dual effect on both cell expansion and regenerative division presumably balancing turgor pressure and cell wall properties to regulate a steady growth towards the wound and permit accelerated periclinal divisions.

**Auxin and wounding in activation of ERF115 expression**

ERF115 is a wound-responsive transcription factor and so far, the prime candidate for mediating regeneration in plant roots. It is typically not expressed in the undisturbed root meristems but is highly upregulated after removal of the root tip and required for its restoration (5, 6, 10). After single cell ablation, its expression is induced only in those 1 – 3 wound-adjacent endodermis or stele cells that later undergo wound-responsive divisions (Fig. 4A). In contrast, auxin (1 µM NAA) treatment, while having no effect in non-wounded roots, strongly induced *ERF115::GFP* expression around the wound (Fig. 4A-B) spreading to all adjacent cells including cortex cells and those above and below the ablation. Notably, ERF115 expression expanded also to cells non-adjacent to the wound, which normally do not

undergo wound-responsive cell expansion and cell division. Overall, auxin induced approx. 8-fold increment of the *ERF115::GFP* expression after wounding (Fig. 4C).

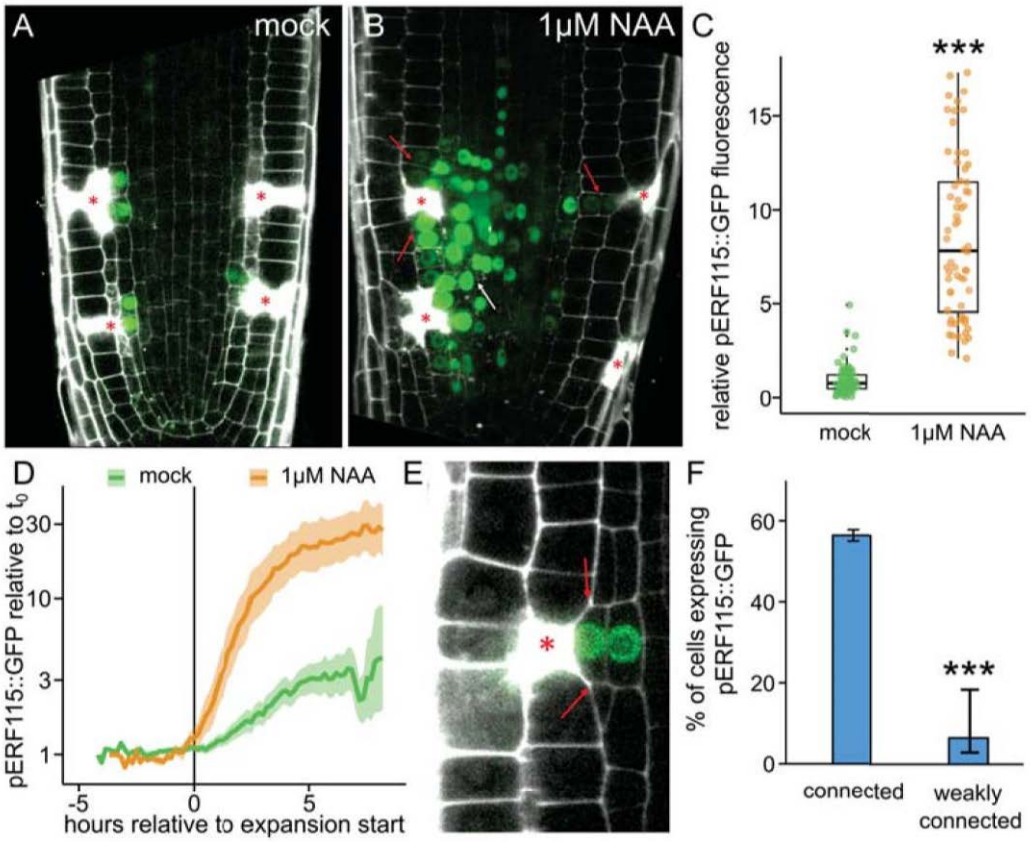


**Figure 4. ERF115 expression is connected to auxin and expansion**

**(A-C)** Auxin application massively increases ERF115 expression around wounds. *ERF115::GFP* (green) expression on wound-adjacent cells in mock **(A)** upon 1 μM NAA treatment **(B)**. Asterisks mark ablated cells. Red arrows indicate *ERF115::GFP* expression expansion to wound-adjacent cortex cells and white arrow indicates *ERF115::GFP* expression expansion to non-wound adjacent endodermis and stele cells. **(C)** Quantification of the relative *ERF115::GFP* fluorescence in wound-adjacent cells (normalized to the *ERF115::GFP* mean intensity on mock conditions), on mock conditions (green dots) or upon μM NAA treatment. Data are represented as relative fluorescence intensities of individual cells. Statistical significance was computed from a two-sample Wilcoxon test. **(D-F)** *ERF115::GFP* expression correlates with pre-mitotic expansion. **(D)** Quantification of *ERF115::GFP* relative gene expression (compared to $t_0$) of wound-adjacent cells before and after the expansion onset - $t_{lag}$ (= 0 hours) - on mock (green line) or upon 1 μM NAA treatment (orange line). Lighter background represents standard error. **(E)** Expression of *ERF115::GFP* in wound-adjacent cells after restorative cell division. Red arrows indicate to junctions where the cell is not fully

connected to the wounded-cell (asterisk). **(F)** Quantification of the percentage of cells expressing *ERF115::GFP*, grouped by grade of connection (connected or non-fully connected to the wound). Data are represented as ratios (bars) with error bars indicating upper and lower quartiles. Statistical significance was computed from a Chi-square test.

---

Next, we evaluated the *ERF115::GFP* expression using different auxin concentrations. We observed that the minimum concentration of NAA required to enhance ERF115 was 100 nM NAA, which significantly increased the GFP intensity in the few cells undergoing restorative cell divisions. In contrast, the expression domain expanded only at higher concentrations like 1 µM NAA (SI Appendix, Fig. S5A). To test the involvement of the canonical TIR1 pathway, we evaluated the *ERF115::GFP* expression after wounding in *tir triple* root tips or in *CCV-TIR1* background. Both genetic tools confirmed the involvement of TIR1/AFB signalling (SI Appendix, Fig. S5B-C). Notably, *ERF115::GFP* expression was absent also in the untreated *tir triple* mutant (SI Appendix, Fig. S5C) suggesting an involvement of TIR1/AFB auxin signalling in activation of ERF115 expression by endogenous auxin levels.

The ERF115 expression has also been proposed to be regulated by other signals such as MeJA, $H_2O_2$ or brassinosteroids (6, 11, 12); nonetheless, unlike in case of auxin, none of these other signals showed a pronounced effect on wound-responsive *ERF115::GFP* expression (SI Appendix, Fig. S6A-E, K-L). Ethylene, a wound-responsive hormone recently connected to innate immune system in the Arabidopsis root after wounding and single cell ablation (7, 31), did not influence the ERF115 expression (SI Appendix, Fig. S6F-H; Heyman et al., 2013) and only slightly decreased the amount of restorative divisions in the meristem (SI Appendix, Fig. S6I). Application of other hormones related with cell wound response, including SA and ABA also did not change the *ERF115::GFP* expression after wounding (SI Appendix, Fig. S6J, M). These results suggest that auxin is rather a specific signal regulating the *ERF115::GFP* expression after wounding, albeit not the primary trigger for its activation.

**Auxin-regulated cell expansion and activation of ERF115 expression**

Since auxin regulates both cell expansion and ERF115 expression after wounding, we performed long-term, live observations to investigate possible correlation between these processes. Indeed, even in absence of auxin treatment, we found that cells with higher expansion rates showed also increased *ERF115::GFP* signals (SI Appendix, Fig. S7E). Additionally, we observed that *ERF115::GFP* expression was absent from those cells that

were only weakly connected to the wound and hence did not trigger cell expansion (Fig. 4E-F).

Given this strong spatial connection between ERF115 expression and wound-responsive expansion, we investigated their time dynamics to gain insight into their interdependency. ERF115 expression was detectable only after the onset of expansion (Fig. 4D), ruling out ERF115 as a major activator of wound-responsive expansion. However, after treatment with auxin, ERF115 expression coincided or preceded the onset of expansion (Fig. 4D). Considering the temporal dynamics of upstream transcriptional regulation and GFP maturation, this also ruled out that ERF115 expression is a direct consequence of cell expansion.

In conclusion, wound-responsive activation of ERF115 expression and cell expansion strongly correlated spatially and temporary, but did not directly depend on each other, suggesting so far unknown, wound-induced upstream signal activating both.

**Tissue integrity and turgor in wound regeneration**

Given the here identified importance of cell expansion for both the regenerative divisions and ERF115 expression, we hypothesised that rapid, non-genetic factors such as collapse of injured cells, changes in turgor or cell wall tensions may be important early cues for inducing regeneration processes. Therefore, we investigated more closely the immediate responses of the targeted cell and its surrounding neighbours during ablation-induced injury. Following ablation, the cellular content of the killed cells was released to the environment resulting in a pressure drop, which was visible as a strong bulging of the neighbouring cells towards the wound (SI Appendix, Fig. S7A, Movie S7). In those neighbouring cells, we observed a quick displacement of nuclei (SI Appendix, Fig. S7C) and a slow reduction of the initial bulging (SI Appendix, Fig. S7B, Movie S7) suggesting a loss of cell volume in the neighbouring cells. Over longer time (> 60s), pressure built up again in the neighbouring cells and they bulged again towards the wound (SI Appendix, Fig. S7A). Notably, the release of cellular content and the quick pressure changes as quantified by instant nucleus displacements were absent from roots during a hyperosmotic, 0.5 M Mannitol treatment (SI Appendix, Fig S7D, G). This suggests that the collapse of killed cells causes a strong turgor pressure shock in the neighbouring cells influencing the cell expansion and ERF115 expression.

In support of this notion, treatment with Mannitol strongly decreased wound-induced cell expansion and wound-triggered periclinal divisions (Fig. 5A-B). Notably, the normally occurring, anticlinal (non-restorative, proliferative) divisions were still ongoing under these

hyperosmotic conditions (SI Appendix, Fig S7F). Additionally, the bulging of cell walls towards the inner neighbours, indicative of changes in turgor pressure, was significantly reduced during mannitol treatment (SI Appendix, Fig. S7G-H). This implies that turgor changes are specifically required for regenerative but not proliferative divisions.

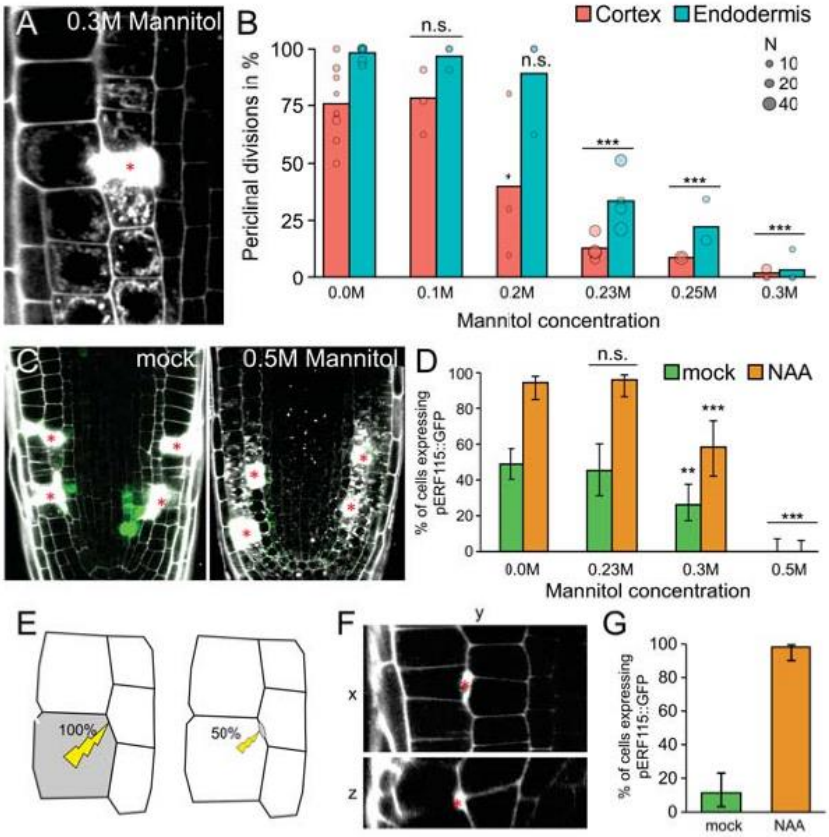


**Figure 5. ERF115 expression correlates with expansion induction**

**(A-B)** Hyperosmotic treatment inhibits restorative periclinal divisions. **(A)** Cortex cell ablation 12 hours after ablation during 0.3 M Mannitol treatment. **(B)** Quantification of restorative periclinal division rates (in %) of endodermal (blue) and cortex (red) cells, after different Mannitol (from 0 to 0.3 M) treatments. Bars represent weighted means and dots represent individual experiments (area indicates sample size). Statistical significance was computed from conditional logistic regression. **(C-D)** Hyperosmotic treatment reduces ERF115 induction. **(C)** *ERF115::GFP* (green) expression on root tips after cell ablation (wounding) in mock conditions (left) or in media supplemented with 0.5 M Mannitol (right). **(D)** Quantification of wound-adjacent cells expressing *ERF115::GFP* on mock (green bars) or upon auxin treatment (NAA, orange bars) in media supplemented with different Mannitol concentrations (from 0 to 0.3 M). Data are represented as ratios (bars) and error bars indicate upper and lower quartiles. Statistical significance was computed from a Chi-Square test **(E-G)** Harming only the cell envelope does not trigger ERF115 induction. **(E)** Schematic representation of cell wounding after application of 100 or 50% laser power during laser cell ablation.

**(F)** Harmed cell region after using 50% laser power presented as vertical section (XY, upper panel) and horizontal projection (ZY, lower panel). Cell harming is stained by a strictly confined PI accumulation (in white, red asterisk). **(G)** Quantification of the percentage of wound-adjacent cells expressing *ERF115::GFP* after using 50% laser power in root tips on mock or upon 1 μM NAA treatment. Data are represented as ratios (bars) and error bars indicate upper and lower quartiles.

---

Next, we evaluated the effect of hyperosmotic treatment on *ERF115::GFP* expression by application of different concentrations of Mannitol to locally injured roots. In contrast to cell expansion, we observed that at concentrations of 0.23 M and 0.3 M Mannitol the ERF115 expression was only slightly reduced after wounding in both, mock and auxin (1μM NAA) treatment. Notably, only hyperosmotic treatment with 0.5 M Mannitol inhibited *ERF115::GFP* expression in the wounded root tips (Fig. 5C-D) suggesting that cell collapse after wounding, which is absent at 0.5 M Mannitol treatment (see above) is crucial for triggering ERF115 expression.

This prompted us to test the importance of the collapse of the ablated cells for cell expansion, ERF115 expression and regeneration. To this end, we modified the UV ablation technique by reducing the laser power to 50%. We regularly managed to harm the cell envelope between two cells rather than the whole cells (Fig. 5E-F). These harmed cells usually did not induce ERF115 expression (Fig. 5G). However, in rare cases these cells specifically triggered ERF115 induction, which was strongly enhanced by auxin treatment (Fig. 5G; SI Appendix, S7I). They also induced periclinal cell divisions accompanied by minor cell expansion on rare occasions (Fig. SJ), suggesting minor wound signalling without cell collapse through cell wall integrity sensing or minor pressure changes after cell envelope harming.

This suggests that cellular collapse after wounding is crucial for ERF115 expression and wound-responsive cell expansion. Furthermore, turgor pressure stress after ablation is a component of the wound response and might influence together with the local increase in auxin signalling fast and efficient regeneration.

**Discussion**

In this work we addressed the question how plants can effectively regulate the coordination of wound-responses on a cellular level to mediate tissue regeneration. We found that local induction of auxin signalling in concert with wound-induced non-genetic mechanisms such as local expansion of cells in wound vicinity play major roles in this process. In summary, our

data shows how strictly localized auxin signalling coordinates the wound responses by regulating (i) cell division rates, (ii) cell expansion rates and (iii) the transduction of the wound signal through activation of the ERF115 transcription factor (SI Appendix, Fig. S8).

Our data also shows that turgor-driven swelling of the wound-adjacent cells is crucial for the initiation of restorative divisions and subsequent regeneration. This shows interesting similarities/parallels to the initiation of lateral root primordia, where pericycle cells swell before induction of asymmetric divisions (32). This process requires the overlying endodermis cells to shrink or collapse, which can be imitated by local ablation of endodermis cells in the elongation zone (33). The capacity to divide after ablation in the pericycle is independent of auxin signalling; however, local auxin signalling is essential in this context for the induction of a formative and asymmetric first division leading to the proper formation of lateral root primordia (33, 34). We have observed a similar phenomenon; local auxin increase in cells adjacent to the wound regulates both their expansion and division during regeneration. An accumulation of auxin could have many sources; e.g. release from conjugates or a production from less known, alternative biosynthetic pathways, altered auxin importer activities or a general release from the plasmodesmata-associated ER as consequence of the disrupted connection to the ablated neighbour. Since such processes are difficult to study, the origin remains elusive; however, daughters of wound-adjacent cells also exhibit increased auxin signalling activity implying an active process working throughout the duration of regeneration.

Auxin has a well-established role in expansion on a cellular level, through cell wall remodelling (35), and on a tissue level, through hydraulic pressure regulation (36). The biphasic mode of auxin in cell wall remodelling (27) shares similarities with our observed dual auxin effect of promoting and inhibiting cell expansion and restorative divisions; hence, suggesting a negative feedback loop, where prolonged auxin signalling would inhibit wound-responsive division and expansion at the end of the regeneration process. The overproliferation of cells and the tissue swelling after wounding is similar to defects in LRP initiation during disturbed auxin signalling (37), suggesting that accurate auxin signalling is crucial for the regulation of wound-responsive cell expansion and divisions.

The turgor pressure - or osmotic - stress in the adjacent cells following the wounding might be a key component in the wound signalling mechanism as suggested from other tissues (38, 39). Recently, a similar, locally restricted induction of wound responses in the root - the activation of immune signalling - has been proposed to be caused by local pressure changes (31). Notably, the wound-responsive expression of ERF115 is also inducible by

osmotic stress (40) and a direct target of ERF115 includes one member of the expansin family (9); cell wall remodelling proteins expressed during osmotic stress to maintain steady growth even during reduced turgor pressure (41). This suggests that ERF115 is a key component of a hydraulic/osmotic stress response after wounding and might be involved in integrating auxin signalling and pressure stress to define the zone of wound response and to both induce and spatially restrict regeneration processes.

Further investigation of the induction of ERF115 expression, as a marker for restorative patterning and involvement of other components suggested in wounding responses in the root could help revealing upstream regulators of such local yet distinctive regeneration processes of inducing cell expansion and targeted, restorative cell divisions.

**Acknowledgements**

We are thankful to Ben Scheres, Dolf Weijers, Keiko Torii, Lieven De Veylder, Mark Estelle and Moritz Nowak for sharing published material. We thank the Bioimaging and Life Science Facilities at IST Austria for providing invaluable assistance. The research leading to these results has received funding from the European Research Council under the European Union's Seventh Framework Programme (FP7/2007-2013) / ERC grant agreement n° 742985 and from the FWF under the stand-alone grant P29988.

**Author contributions**

L.H. and J.F. initiated the project. L.H., J.C.M., P.M., S.Y. and J.F. designed experiments. L.H., P.M. and S.Y. performed experiments and analyzed data. L.H., J.C.M. and J.F. wrote the manuscript. P.M., E.B. and S.Y. edited the manuscript. J.F. acquired funding.

## METHODS

### Plant material

*Arabidopsis thaliana* (L.) Heynh (accession Columbia-0) was used in this work (Wt). The following transgenic *Arabidopsis thaliana* lines and mutant lines were described previously: *RPS5A::mDII-ntdTomato - RPS5A::DII-n3Venus* (R2D2, Liao et al., 2015), *HTR5::NLS-GFP* (42), *tir1-1 afb2-1 afb3-1* (*tir triple*, Dharmasiri et al., 2005), *CCV-TIR1 tir1-1 afb2-1* (26), *ERF115::NLS-GFP-GUS* (*ERF115::GFP*, (10), *ERF115::NLS-GFP-GUS coi1-2* (6) *35S::MAP4-GFP* (43). *ERF115::NLS-GFP-GUS* was introduced into the *tir1-1 afb2-1 afb3-1* and *CCV-TIR1* backgrounds by genetic crossing. *tir1-1 afb2-1 afb3-1* seedlings were identified by PCR-cased genotyping (Dharmasiri et al., 2005) in F2 and F3 generations *ERF115::NLS-GFP-GUS* and *CCV-TIR1* carrying plants were identified in F2, F3 and F4 generations by kanamycin and basta resistance, respectively.

### Growth conditions

Seeds of *A. thaliana* were sown on Murashige and Skoog (1/2MS) medium (Duchefa) with 1% sucrose and 1% agar, stratified for 1-2 d and grown for 3-5 d at 21°C in a 16 h light/8 h dark cycle.

### Pharmacological treatments

Seedlings were transferred on solid MS medium containing the indicated chemicals: propidium iodide (PI, 10 µM, Sigma-Aldrich or Thermofisher), Naphthylacetic acid (NAA, Duchefa Biochemie, final concentration as indicated - if nothing indicated: 1 µM), Naphthylphthalamic acid (NPA, final concentration 10 µM), Yucasin (Wako Chemicals GmbH, final concentration 100µM), L-Kynurenine (Kyn, Sigma-Aldrich, final concentration 10 or 50 µM, as indicated), convex IAA (CVX-IAA, TCI - Tokyo Chemical Industry Co., final concentration 250 nM), Methyl Jasmonate (MeJA, Sigma-Aldrich, final concentration 50 µM), Hydrogen peroxide ($H_2O_2$, Sigma-Aldrich, final concentration 200 µM), (±)-Abscisic acid (ABA, Sigma-Aldrich, final concentration 25 µM), Epibrassinolide (EBL, Sigma-Aldrich, final concentration 1 µM), Brassinazole (Bz, Sigma-Aldrich, final concentration 1µM), Salicylic acid (SA, Sigma-Aldrich, final concentration 40 µM), Mannitol (Sigma-Aldrich, final concentration 0.1 - 0.5 M, as indicated).

### Sample preparation

Seedlings were placed on chambered cover glass (VWR, Kammerdeckgläser, Lab-Tek™, Nunc™ - eine kammer, catalog number: 734-2056) as described (Marhavý & Benková, 2015). With the chamber, a block of solid MS media was cut out and propidium iodide solution was added. After the liquid soaked in, 10-15 seedlings were transferred to the agar and the block was inserted into the chamber.

**Confocal imaging and image processing**

Confocal imaging was performed with Zeiss LSM700/800 inverted microscopes using 20x or 40x objectives or a Spinning disk imaging system. Detection of fluorescence signals was carried out for GFP (excitation 488 nm, emission 507 nm), YFP (excitation 514 nm, emission 527 nm) and PI (excitation 536 nm, emission 617 nm). For fixed time point measurements, samples were observed 12 hours after ablation or at indicated time points. Images were analyzed using the ImageJ (NIH; http://rsb.info.nih.gov/ij) and Zeiss Zen 2.3 "Black" or "Blue" software. Where necessary, images were processed by adjusting contrast and lightness.

**Spinning disk imaging**

For the observation of immediate effects during/after ablation, an Andor spinning disk microscopy (CSU X-1, camera iXon 897 [back-thinned EMCCD], FRAPPA unit and motorized piezo stage) 63× water immersion objective was used. Videos were acquired with 1 focal plane, every 0.2 seconds, for 1-10 min. All images in a single experiment were captured with the same settings.

**Vertical stage microscopy, root tracking and image processing**

Vertical stage microscopy for long-term tracking of root meristems was performed as described (5, 19). Roots were imaged with a vertically positioned LSM700 or LSM800 inverted confocal microscope and Zeiss Zen 2.3 "Black" or "Blue" software, respectively, with 20x objective and detection of PI, GFP (see above) and transmitted light. Z-stacks of 30-42 µm were set accordingly to image each cell at least once. For the root-tracking, the TipTracker MATLAB script (Zen Black) or the TipTracker internal macro (Zen Blue) were used; interval duration was set between 600 s (10 min) and 720 s (12 min). The resulting images were concatenated and analysed using ImageJ. For registration, ImageJ macros "correct 3D drift", "StackReg" or "MultiStackReg" were used. Kymographs were generated using the "Reslice" tool and restacked in case of non-registered videos.

**UV laser ablation setup**

The UV laser ablation was performed as described in ref. (5, 33) which are based on the layout published in ref. (45). For the cell envelope harming, we used 50% of the laser power needed for the elimination of a full cell. The laser was applied in the upper corner of the outer neighbouring cell of the cell of interest (Fig. 5C).

**Quantification and statistical significance**

Asterisks illustrate the p-value: $p < 0.001$ is ***, $p < 0.01$ is ** and $p < 0.05$ is *

**Periclinal divisions**

For counting the (absolute) amount of periclinal divisions after ablation, the amount of ablations with and without periclinal divisions (division plane parallel or oblique to the growth axis) in any of the adjacent cells (if nothing else indicated: only inner cells) were recorded and the ratio of positive to all events was calculated. For the differences, the ratios for each sample experiments were subtracted from the respective control experiment (untreated Wt). The mean of these differences from multiple experiments was weighted based on the sample size.

As in ref. (5) the binary data was analysed using conditional logistic regression (46, 47), pairing the data within individual experiments. The statistical significance was computed using the clogit function from the R package “survival”.

**Fluorescence intensity in time series experiments**

Signal intensity of each observed nucleus from multi-stack (3D) videos in the green (or for mDII-ntdTomato: red) channel was quantified using ImageJ and recorded for each available time frame. Similarly, data from reference nuclei (neighbouring, non-adjacent cells) was recorded and the ratio of sample to reference value was calculated for each single time point. For *ERF115::GFP*, the ratio of each time frame to the first time frame was calculated.

Statistical significance was calculated on the ratios using a one-sample Wilcoxon test (based on the non-normal distribution of the data) using wilcox.test() in R with mu=1 (reference cell).

**Cell expansion**

Cell expansion was approximated by the cell width, which was quantified as the distance between the midpoint of the cell wall segment touching the ablation site and the midpoint of the opposite cell wall at every time point using ImageJ. Expansion rates were calculated between the onset of expansion (end of lag phase) and the initiation of cell division (nuclear

envelope breakdown). Statistical significance between samples was calculated using a Student's t-test using t.test() in R. For calculating the point of expansion collapse (SI Appendix, Fig. S4E), expansion rates at each time point were calculated from cell width expansion throughout the previous 5 time frames (50 minutes). The point of expansion collapse was determined as the first time point in which the expansion rate dropped below 1 µm/h.

**Cell wall bulging**

The distance between (i) the midpoint of a straight line connecting the two cell corners facing the inner adjacent cell and (ii) the midpoint of the cell wall facing the inner adjacent neighbour was calculated as inner cell wall bulging. The obtained values from wound-adjacent cells were subtracted from the closest, non-adjacent cells of the same cell type (usually the direct neighbour).

The statistical significance was calculated using a two-sample Wilcoxon test between the mock and the Mannitol treatment values with wilcox.test() from R.

**Nucleus displacement**

The distance of nucleus movement/displacement directly after ablation was measured until maximum 5 seconds after ablation from videos obtained from a spinning disk imaging system (1 frame per 0.2 seconds). The statistical significance was calculated using a two-sample Wilcoxon test between the mock and the Mannitol treatment values with wilcox.test() from R.

**Fluorescence intensity in fixed time point experiments**

For quantitative measurements, the signal intensity of all wound adjacent (inner) cells within one focal plane was measured using ImageJ in the green channel. Each obtained value from one experiment/repetition was divided by the mean fluorescence intensity in the reference sample (untreated Wt) to obtain (comparable) relative fluorescence intensities.

The statistical significance was calculated using a two-sample Wilcoxon test between the reference and the sample values with wilcox.test() from R.

For qualitative data, the amount of cells with and without a visible GFP accumulation in the nucleus was counted and the ratio of positive to all observed events was computed. For the error bars, the borders of the upper and lower quartiles were calculated assuming a beta distribution of the binary values with qbeta() from R.

The statistical significance was computed with a Qui-Square test for binary data using the chisq.test() function in R.

**Data Availability**

The R code to compute statistical significance for binary data using a conditional logistic regression can be found in the SI Appendix, Code S1. Raw data in the form of microscope images and compiled videos is available and can be accessed at http://idr.openmicroscopy.org/tissue/.

**References**


1. C. van den Berg, V. Willemsen, W. Hage, P. Weisbeek, B. Scheres, Cell fate in the Arabidopsis root meristem determined by directional signalling. *Nature* **378**, 62–65 (1995).
2. F. Berger, J. Haseloff, J. Schiefelbein, L. Dolan, Positional information in root epidermis is defined during embryogenesis and acts in domains with strict boundaries. *Curr. Biol.* **8**, 421–430 (1998).
3. M. Ikeuchi, *et al.*, Molecular Mechanisms of Plant Regeneration. *Annu. Rev. Plant Biol.* **70**, 377–406 (2019).
4. L. Hoermayer, J. Friml, Targeted cell ablation-based insights into wound healing and restorative patterning. *Curr. Opin. Plant Biol.* **52**, 124–130 (2019).
5. P. Marhava, *et al.*, Re-activation of Stem Cell Pathways for Pattern Restoration in Plant Wound Healing. *Cell* **177**, 957-969.e13 (2019).
6. W. Zhou, *et al.*, A Jasmonate Signaling Network Activates Root Stem Cells and Promotes Regeneration. *Cell* **177**, 942-956.e14 (2019).
7. P. Marhavý, *et al.*, Single-cell damage elicits regional, nematode-restricting ethylene responses in roots. *EMBO J.* **38**, e100972 (2019).
8. T. Hander, *et al.*, Damage on plants activates Ca2+-dependent metacaspases for release of immunomodulatory peptides. *Science* **363**, eaar7486 (2019).
9. J. Heyman, *et al.*, ERF115 Controls Root Quiescent Center Cell Division and Stem Cell Replenishment. *Science (80-. ).* **342**, 860–863 (2013).
10. J. Heyman, *et al.*, The heterodimeric transcription factor complex ERF115–PAT1 grants regeneration competence. *Nat. Plants* **2**, 16165 (2016).
11. H.-S. Lee, *et al.*, Brassinazole resistant 1 (BZR1)-dependent brassinosteroid signalling pathway leads to ectopic activation of quiescent cell division and suppresses columella stem cell differentiation. *J. Exp. Bot.* **66**, 4835–49 (2015).
12. X. Kong, *et al.*, PHB3 Maintains Root Stem Cell Niche Identity through ROS-Responsive AP2/ERF Transcription Factors in Arabidopsis. *Cell Rep.* **22**, 1350–1363 (2018).
13. D. Xu, *et al.*, YUCCA9-Mediated Auxin Biosynthesis and Polar Auxin Transport Synergistically Regulate Regeneration of Root Systems Following Root Cutting. *Plant Cell Physiol.* **58**, 1710–1723 (2017).
14. I. Efroni, *et al.*, Root Regeneration Triggers an Embryo-like Sequence Guided by

Hormonal Interactions. *Cell* **165**, 1721–1733 (2016).

15. Z. Ding, J. Friml, Auxin regulates distal stem cell differentiation in Arabidopsis roots. *Proc. Natl. Acad. Sci. U. S. A.* **107**, 12046–12051 (2010).
16. J. Xu, *et al.*, A molecular framework for plant regeneration. *Science (80-. ).* **311**, 385–388 (2006).
17. S. Yoshida, *et al.*, Genetic control of plant development by overriding a geometric division rule. *Dev. Cell* **29**, 75–87 (2014).
18. C. Y. Liao, *et al.*, Reporters for sensitive and quantitative measurement of auxin response. *Nat. Methods* **12**, 207–210 (2015).
19. D. von Wangenheim, *et al.*, Live tracking of moving samples in confocal microscopy for vertically grown roots. *Elife* **6** (2017).
20. M. Glanc, M. Fendrych, J. Friml, Mechanistic framework for cell-intrinsic re-establishment of PIN2 polarity after cell division. *Nat. Plants* **4**, 1082–1088 (2018).
21. T. Nishimura, *et al.*, Yucasin is a potent inhibitor of YUCCA, a key enzyme in auxin biosynthesis. *Plant J.* **77**, 352–366 (2014).
22. W. He, *et al.*, A small-molecule screen identifies L-Kynurenine as a competitive inhibitor of TAA1/TAR activity in Ethylene-Directed Auxin Biosynthesis and root growth in Arabidopsis. *Plant Cell* **23**, 3944–3960 (2011).
23. J. Zhu, *et al.*, TWISTED DWARF1 Mediates the Action of Auxin Transport Inhibitors on Actin Cytoskeleton Dynamics. *Plant Cell* **28**, 930–948 (2016).
24. N. Dharmasiri, *et al.*, Plant development is regulated by a family of auxin receptor F box proteins. *Dev. Cell* **9**, 109–119 (2005).
25. M. J. Prigge, N. Kadakia, K. Greenham, M. Estelle, Members of the Arabidopsis auxin receptor gene family are essential early in embryogenesis and have broadly overlapping functions. *bioRxiv*, 529248 (2019).
26. N. Uchida, *et al.*, Chemical hijacking of auxin signaling with an engineered auxin-TIR1 pair. *Nat. Chem. Biol.* **14**, 299–305 (2018).
27. E. Barbez, K. Dünser, A. Gaidora, T. Lendl, W. Busch, Auxin steers root cell expansion via apoplastic pH regulation in Arabidopsis thaliana. *Proc. Natl. Acad. Sci. U. S. A.* **114**, E4884–E4893 (2017).
28. M. Fendrych, *et al.*, Rapid and reversible root growth inhibition by TIR1 auxin signalling. *Nat. Plants* **4**, 453–459 (2018).
29. M. Fendrych, J. Leung, J. Friml, Tir1/AFB-Aux/IAA auxin perception mediates rapid cell wall acidification and growth of Arabidopsis hypocotyls. *Elife* **5** (2016).

30. H. Ren, W. M. Gray, SAUR Proteins as Effectors of Hormonal and Environmental Signals in Plant Growth. *Mol. Plant* **8**, 1153–1164 (2015).
31. A. Feng Zhou, *et al.*, Co-incidence of Damage and Microbial Patterns Controls Localized Immune Responses in Roots Article Co-incidence of Damage and Microbial Patterns Controls Localized Immune Responses in Roots. *Cell* **180**, 440–453 (2020).
32. J. E. M. Vermeer, *et al.*, A spatial accommodation by neighboring cells is required for organ initiation in arabidopsis. *Science (80-. ).* **343**, 178–183 (2014).
33. P. Marhavý, *et al.*, Targeted cell elimination reveals an auxin-guided biphasic mode of lateral root initiation. *Genes Dev.* **30**, 471–483 (2016).
34. P. Marhavý, *et al.*, Auxin reflux between the endodermis and pericycle promotes lateral root initiation. *EMBO J.* **32**, 149–158 (2013).
35. M. Majda, S. Robert, The role of auxin in cell wall expansion. *Int. J. Mol. Sci.* **19** (2018).
36. B. Péret, *et al.*, Auxin regulates aquaporin function to facilitate lateral root emergence. *Nat. Cell Biol.* **14**, 991–998 (2012).
37. J. G. Dubrovsky, *et al.*, Auxin minimum defines a developmental window for lateral root initiation. *New Phytol.* **191**, 970–983 (2011).
38. P. Reymond, H. Weber, M. Damond, E. E. Farmer, Differential gene expression in response to mechanical wounding and insect feeding in Arabidopsis. *Plant Cell* **12**, 707–719 (2000).
39. M. Denekamp, S. C. Smeekens, Integration of wounding and osmotic stress signals determines the expression of the AtMYB102 transcription factor gene. *Plant Physiol.* **132**, 1415–1423 (2003).
40. P. Krishnamurthy, *et al.*, Transcriptomics analysis of salt stress tolerance in the roots of the mangrove Avicennia officinalis. *Sci. Rep.* **7** (2017).
41. R. Tenhaken, Cell wall remodeling under abiotic stress. *Front. Plant Sci.* **5**, 771 (2015).
42. M. Ingouff, *et al.*, Live-cell analysis of DNA methylation during sexual reproduction in arabidopsis reveals context and sex-specific dynamics controlled by noncanonical RdDM. *Genes Dev.* **31**, 72–83 (2017).
43. J. Marc, *et al.*, A GFP-MAP4 reporter gene for visualizing cortical microtubule rearrangements in living epidermal cells. *Plant Cell* **10**, 1927–1939 (1998).
44. P. Marhavý, E. Benková, Real-time Analysis of Lateral Root Organogenesis in Arabidopsis. *BIO-PROTOCOL* **5** (2015).

45. J. Colombelli, S. W. Grill, E. H. K. Stelzer, Ultraviolet diffraction limited nanosurgery of live biological tissues. *Rev. Sci. Instrum.* **75**, 472–478 (2004).
46. M. J. Campbell, *Statistics at Square Two Understanding Modern Statistical Applications in Medicine* (John Wiley & Sons, 2013).
47. D. G. Kleinbaum, M. Klein, *Logistic Regression A Self Learning Text Third Edition* (2010) (February 14, 2020).

## SUPPLEMENTARY INFORMATION

### Supplementary Figures

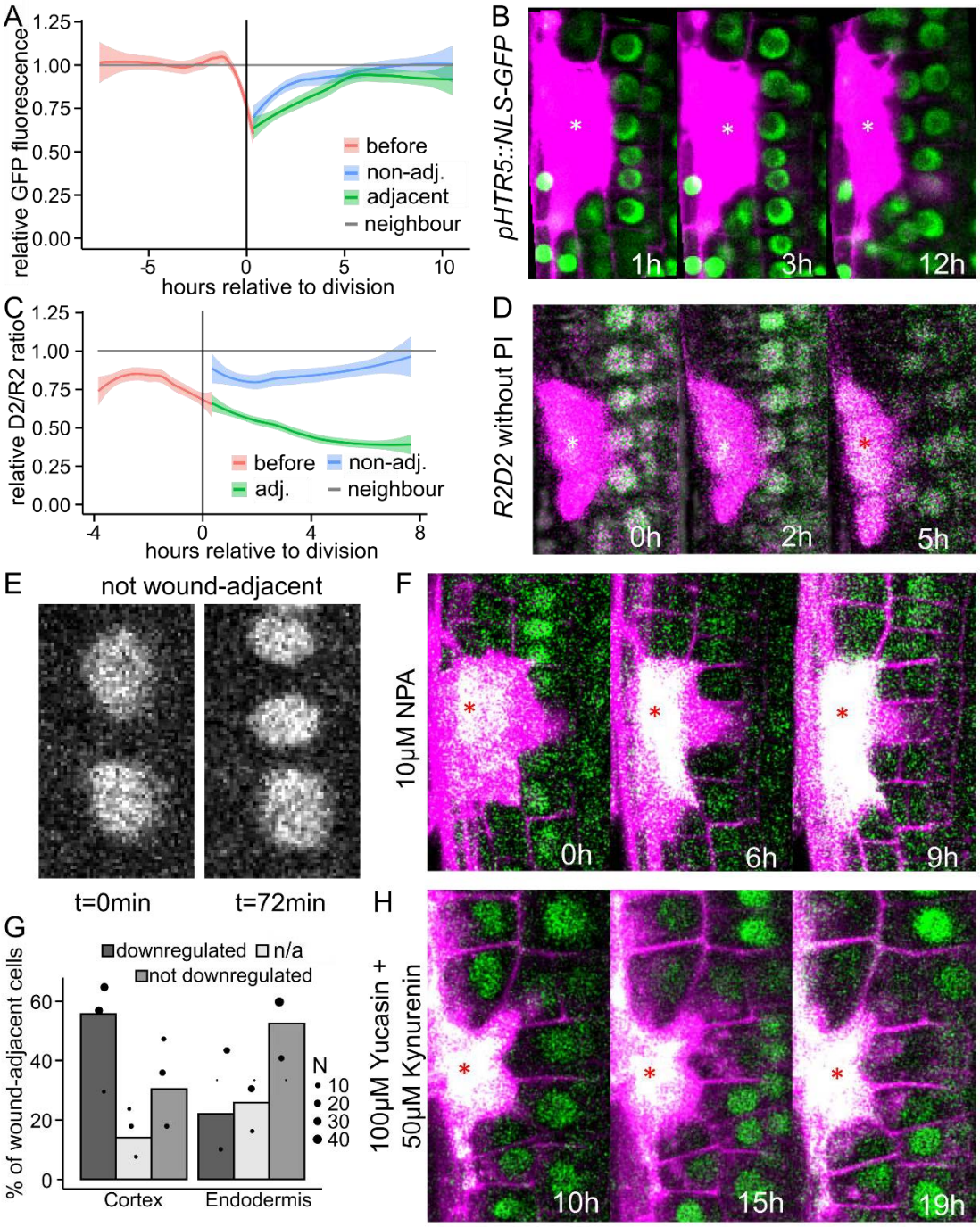


**Figure S1. Downregulation of DII-Venus is specific and occurs only in wound-adjacent cells**

**(A-B)** The ubiquitously expressed *HTR5::NLS-GFP* is not downregulated in wound-adjacent cells.

**(A)** Quantification of the relative GFP fluorescence (of *HTR5::NLS-GFP*) over time of wound-

adjacent cells before (red), or after cell division (wound-adjacent in green; non-wound adjacent in blue). Data are represented as GFP fluorescence in observed cells relative to neighbouring, not-adjacent cells. Time 0 hours represents time of wound-adjacent cell division. Thick lines represent the smoothed mean and lighter background represents smoothed standard error from n=7 cells each. **(B)** Cells expressing *HTR5::NLS-GFP* (green) in cells next/adjacent to ablated cell (marked with asterisk) at three different times (1, 3 and 12 hours). Notice that intensity is not affected during the progress of regeneration or after the first division.

**(C-D)** Downregulation in wound-adjacent cells is specific to DII-Venus compared to mDII-ntdTomato. **(C)** Quantification of the relative DII/mDII (= D2/R2) ratio over time of wound-adjacent cells before (red), or after cell division (wound-adjacent in green; non-wound adjacent in blue). Data are represented as DII/mDII fluorescence intensity ratio in observed cells relative to neighbouring, not-adjacent cells. Time 0 hours represents time of wound-adjacent cell division. Thick lines represent the smoothed mean and lighter background represents smoothed standard error from n=5 cells each.

**(D)** Cells expressing R2D2 marker (green) without PI staining, in cells next/adjacent to ablated cell (asterisk) at three different times after ablation (0, 2 and 5 hours). Notice the downregulation of DII-Venus (green) in wound-adjacent cells before and after the first division.

**(E)** Non-wounding adjacent cells expressing DII-Venus before (left) and after (right) anticlinal (normal) divisions.

**(G)** Quantification of percentage of wound-adjacent cortex or endodermal cells with downregulation (black bars), n/a (not measurable; grey bars) or non-downregulation (dark grey bars) of DII-Venus expression during long-term imaging. Data are represented as weighted mean from 3 experiments (bars) and individual values (dots, area indicates sample size).

**(F, H)** Transport or local synthesis of auxin are not determinant for controlling the upregulation of auxin signalling in the wounding-adjacent cell. DII-Venus (green) expression (of R2D2 negative auxin marker line) in cells around/next/adjacent to ablated cell (marked with asterisk) between 0-19 hours after cell ablation in media supplemented with 10 μM NPA **(F)** or 100 μM + 50 μM Kynurenine **(H)**. Ablated cells are marked with asterisk.

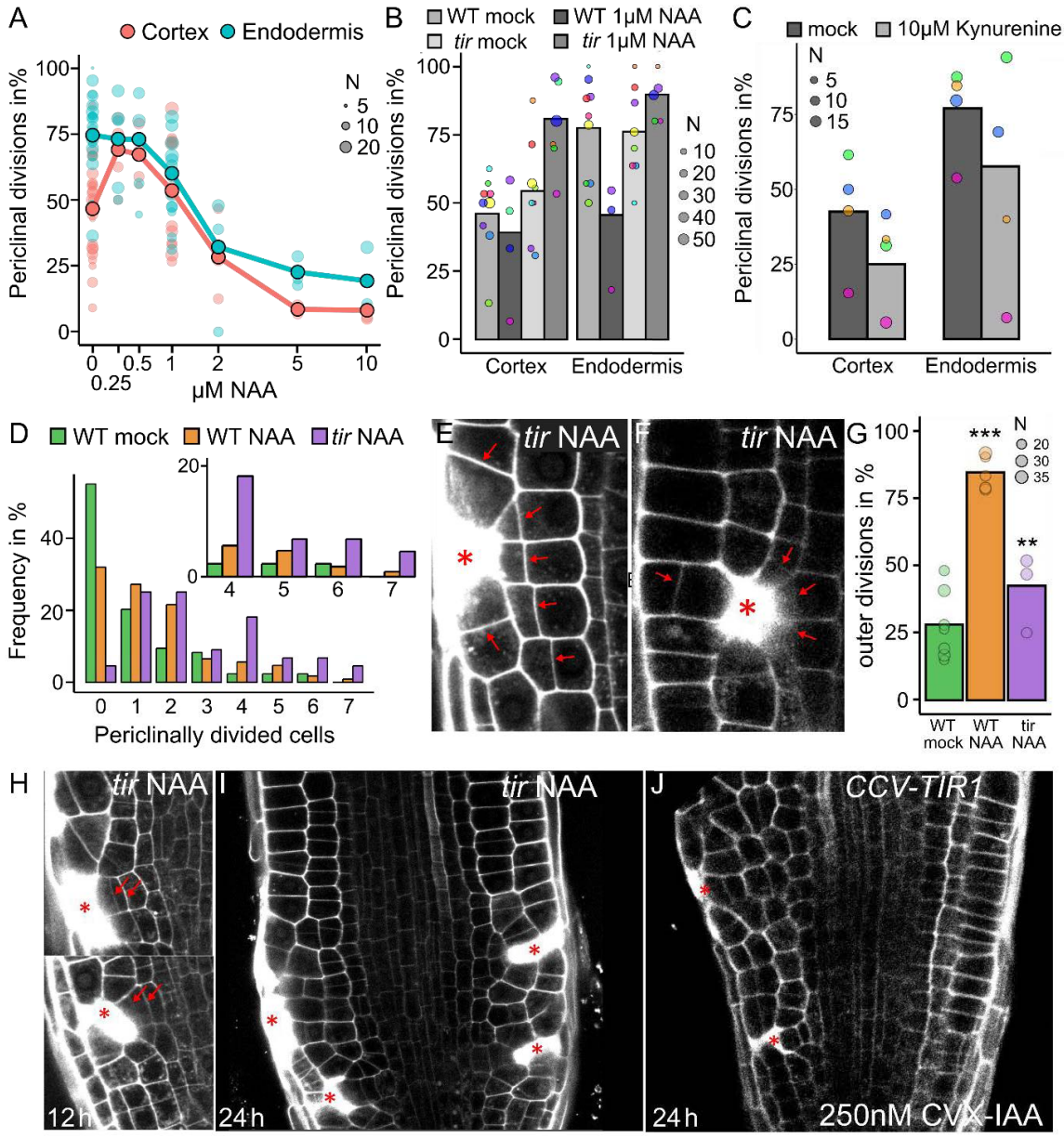


**Figure S2. Auxin effect on restorative divisions and dependency on TIR1 activity**

**(A-B)** Representation of the absolute division rates from Fig. 2A and 2B as number of periclinal divisions 12 hours after ablation. **(A)** Restorative periclinal division rates (in %) of endodermal (blue) and cortex (red) cells, after different auxin (NAA, from 0 to 10 µM) concentration application. Big dots represent weighted mean and lighter dots represent individual experiments (area indicates sample size). **(B)** Restorative periclinal divisions rate (in %) of cortex and endodermal cells of Wt and *tir triple* mutant plants on mock and upon 1 µM NAA treatments. Data are represented as weighted mean (bar) and individual experiments (dots, area indicates sample size).

**(C)** Restorative periclinal divisions rate (in %) of cortex and endodermal cells during mock and 10

µM Kynurenine treatments. Data are represented as weighted mean (bar) and individual experiments (dots, area indicates sample size).

**(D-G)** Auxin expands zone of wound-responsive divisions in Wt and *tir triple* plants. **(D)** Quantification of the number of inner adjacent cells undergoing periclinal divisions from Wt mock treated (green), Wt 1µM NAA treated (orange) and *tir triple* 1µM NAA treated (violet) plants. Data are represented as frequency of the respective amount of divisions. **(E)** Restorative cortex divisions in 1 µM NAA treated *tir triple* plants after epidermal cell ablation (asterisk). **(F)** Restorative cell divisions in outer epidermis cells in 1 µM NAA treated *tir triple* plants after epidermal cell ablation (asterisk). **(G)** Quantification of the number of outer adjacent cells undergoing periclinal divisions from Wt mock treated (green) Wt 1µM NAA treated (orange) and *tir triple* 1 µM NAA treated (violet) plants. Data are represented as weighted mean (bar) and individual experiments (dots, area indicates sample size).

**(H)** Double restorative divisions in 1 µM NAA treated *tir triple* plants 12 hours after ablation.

**(I-J)** Root-swelling inducing restorative cell divisions in 1 µM NAA treated *tir triple* plants **(I)** and in 250 nM CVX-IAA treated *CCV-TIR1* plants **(J)** 24 hours after ablation.

Red arrows indicate new, oblique-periclinal cell plates.

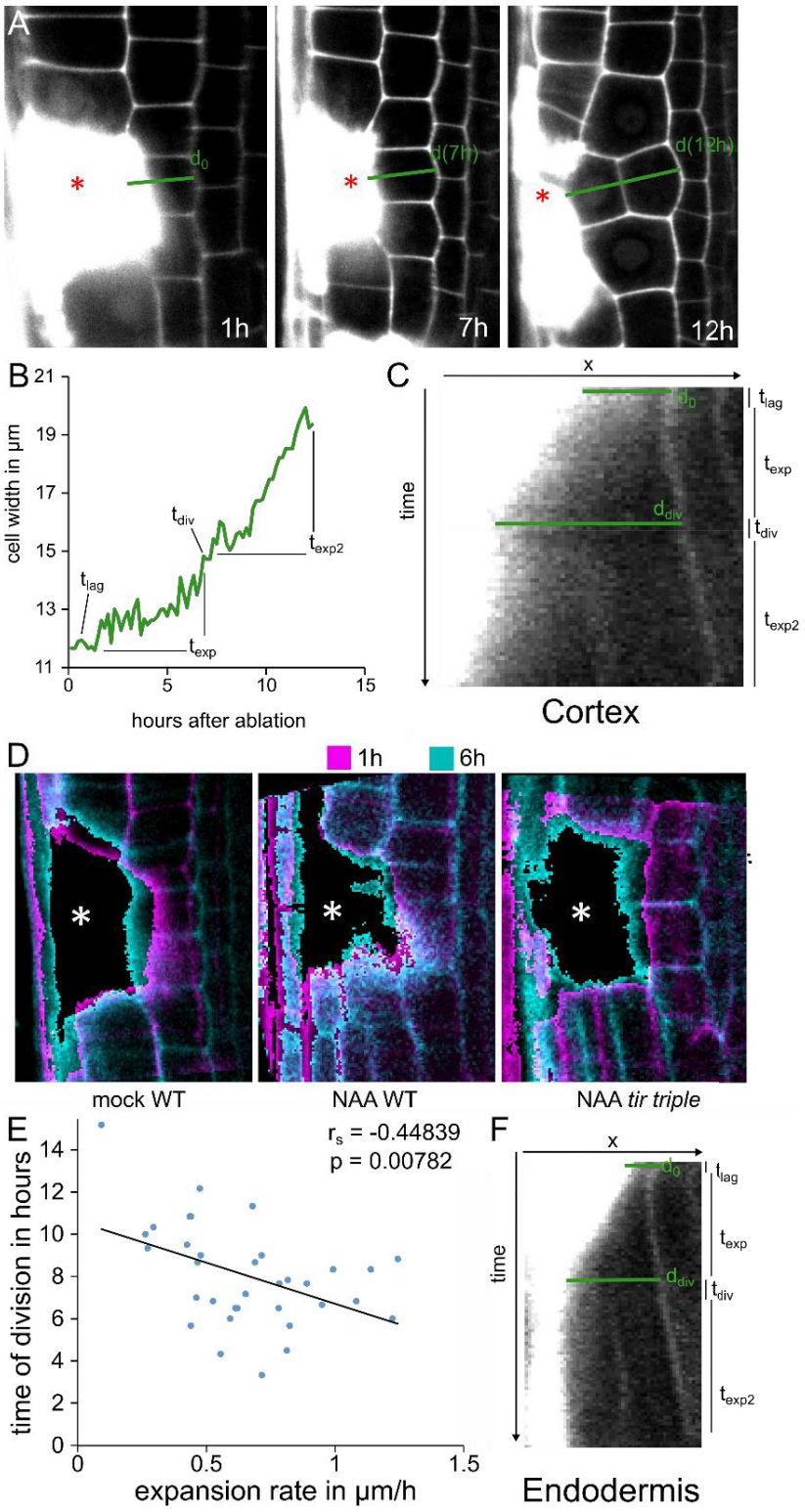


**Figure S3. Wound-responsive cell expansion in cortex cells**

**(A-D)** Pre-mitotic expansion in cortex cells similar to endodermal cells (Fig. 3). **(A)** Cell expansion dynamics of a cortex cell during wounding (epidermis cell ablated, asterisk). Wound-induced cell expansion in cortex 1 hour after cell ablation (left panel), after 7 hours (middle panel) or after cell division (12 hours, right panel). **(B)** Representation of the cell width (in µm) of one representative cortex cell during the restorative cell division stages (in hours after ablation). **(C)** Kymograph of the expansion of the cortex cell from Fig. S3B. The cell width is represented as the distance between the ablated epidermis cell (white area on the left) and the inner neighbour (grey line on the right). The duration of the lag, expansion, division and second expansion phase are indicated on the right. **(D)** Overlay of wound-adjacent cell width of cortex cells at two different time points (1 hour in magenta, and 6 hours in cyan) after ablation in Wt roots on mock (left panel) or upon 1 µM NAA treatment (middle panel), or in 1 µM NAA treated *tir* triple roots (right panel). Asterisk marks ablated cell.
**(E)** Representation of the correlation between pre-mitotic expansion rates and the time required for restorative divisions. The Spearman correlation ($r_s$) and the statistical significance (p-value) are indicated in the top right corner.
**(F)** Kymograph of the expansion of the endodermal cell from Fig. 3B. The cell width is represented as the distance between the ablated cortex cell (white area on the left) and the inner neighbour (grey line on the right). The duration of the lag, expansion, division and second expansion phase are indicated on the right.

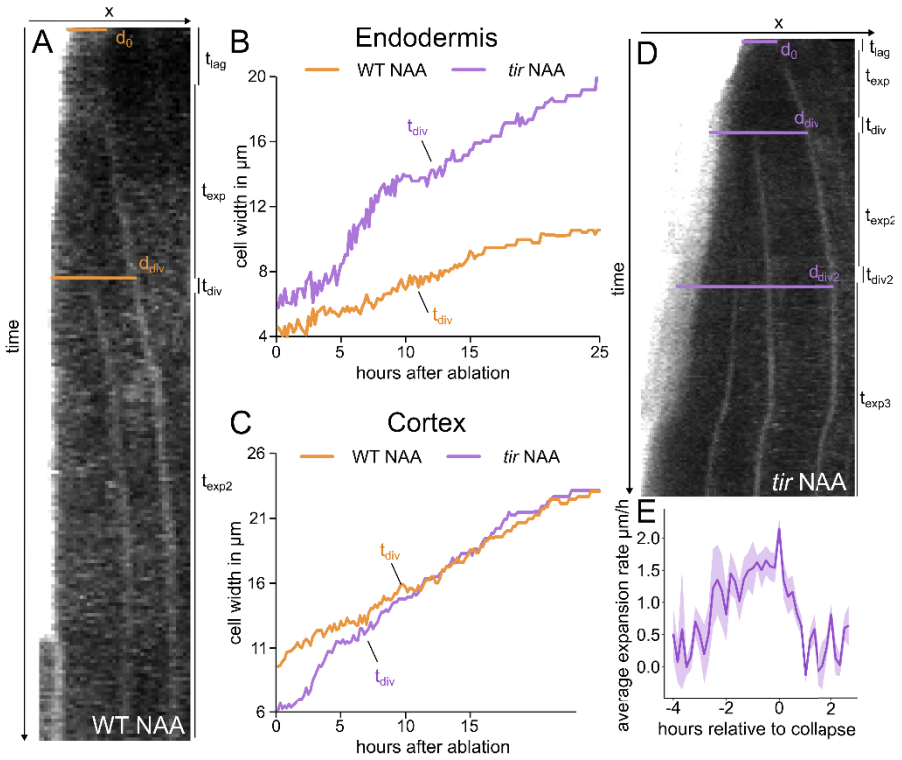


**Figure S4. Wound-responsive cell expansion during auxin treatment**

**(A-D)** Auxin promotes cell expansion in *tir triple* plants and inhibits in Wt plants. **(A)** Kymograph of the 1 µM NAA treated Wt endodermal cell in Fig. S4B. The cell width is represented as the distance between the ablated cortex cell (white area on the left) and the inner neighbour (grey line on the right). Note that the cell width increase and first division are significantly delayed. **(B-C)** Representation of the cell width (in µm) over time in Wt NAA (orange) and *tir triple* NAA (violet) samples from representative endodermal (B) and cortex (C) cells. **(D)** Kymograph of the 1 µM NAA treated *tir triple* cortex cell in Fig. S4C. Note that cell expansion and first division are significantly accelerated resulting in a second division and a third expansion phase.
**(E)** Representation of the cell expansion collapse in 1 µM NAA treated *tir triple* plants. Expansion rates are plotted as mean of N=5 cells (thick line) with standard error (light background). Note that fast expansion followed by collapse can be observed also in violet lines of Fig. S4B and C.

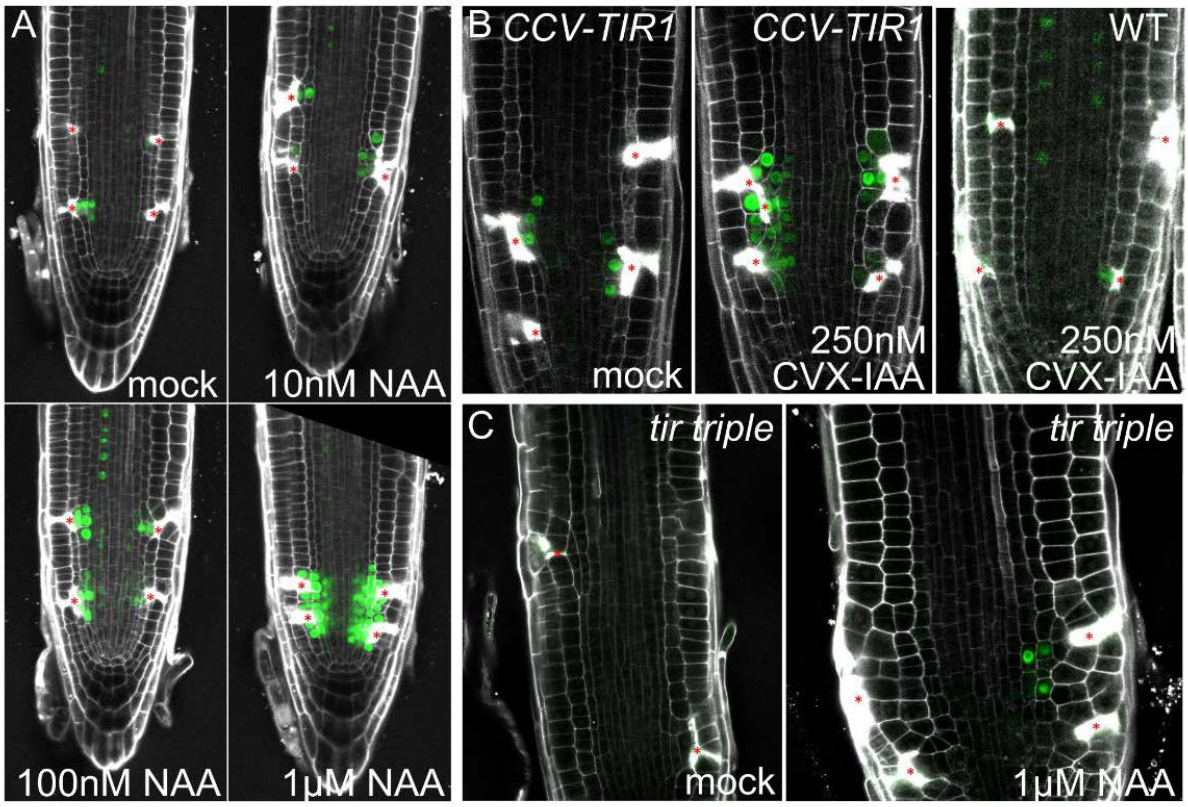


**Figure S5. ERF115 expression depends on auxin concentration and TIR1 activity.**
**(A)** *ERF115::GFP* (green) expression on wound-adjacent cells on mock or upon 10 nM, 100 nM or1 µM NAA treatments 12 hours after ablation.

**(B)** *ERF115::GFP* (green) expression on wound-adjacent cells in the *CCV-TIR* background with mock (left) or 250 nM CVX-IAA treatment (middle) compared to CVX-IAA treated Wt plants (right) 12 hours after ablation.
**(C)** *ERF115::GFP* (green) expression on wound-adjacent cells in mock (left) and 1 μM NAA treated (right) *tir triple* samples 24 hours after ablation.

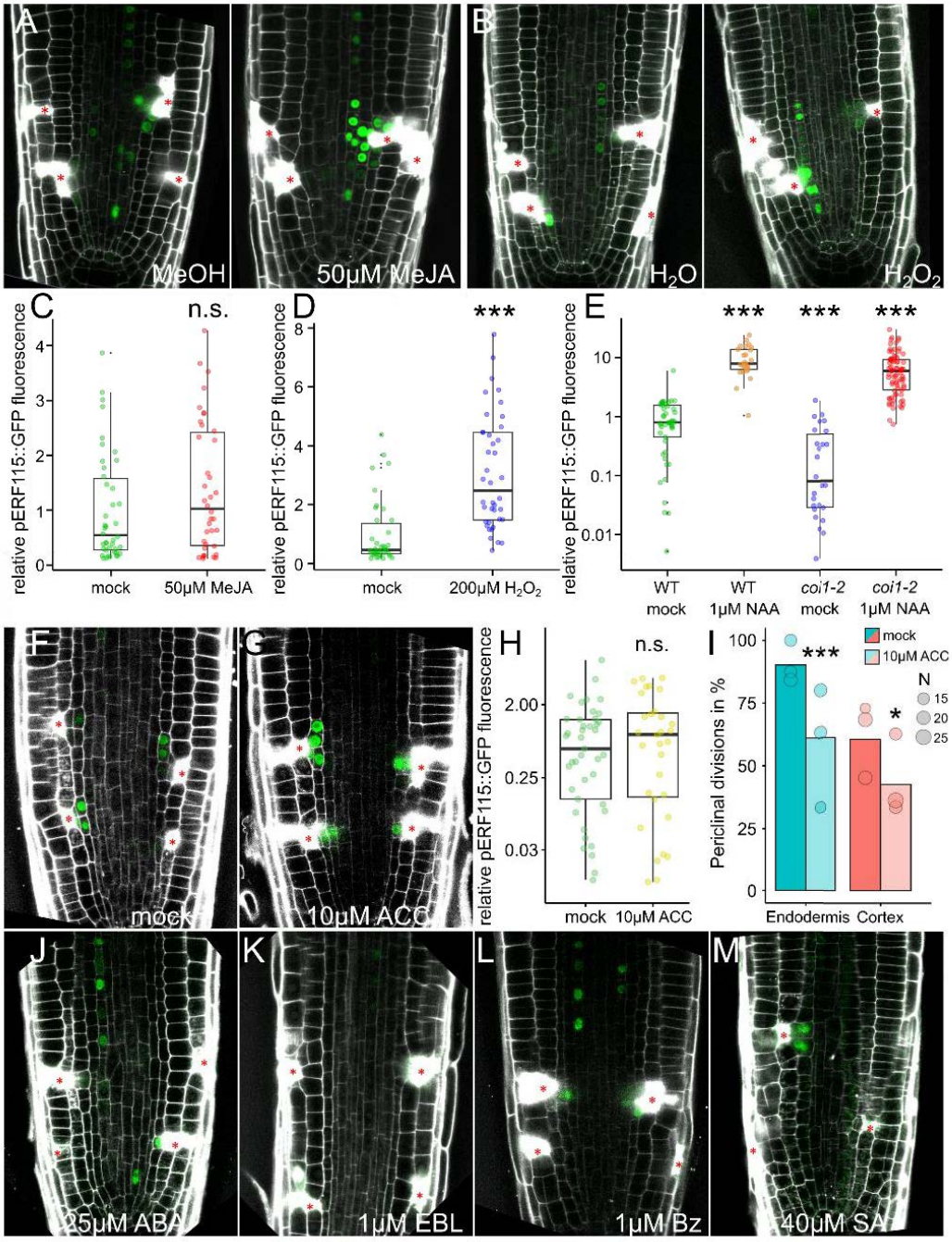


**Figure S6. Effects of known regulators and wound hormones on ERF115 expression**

**(A, C)** MeJA treatment slightly increases ERF115 expression after wounding. **(A)** *ERF115::GFP* (green) expression on wound-adjacent cells in mock (MeOH) and 50 µM MeJA treated plants 12 hours after ablation. **(C)** Quantification of the relative *ERF115::GFP* fluorescence in wound-adjacent cells (normalized to the *ERF115::GFP* mean intensity on mock conditions), on mock conditions (green dots) or upon 50 µM MeJA treatment (red dots). Data are represented as relative fluorescence intensities of individual cells. Statistical significance was computed from a two-sample Wilcoxon test.

**(B, D)** $H_2O_2$ treatment increases ERF115 expression after wounding. **(B)** *ERF115::GFP* (green) expression on wound-adjacent cells in mock ($H_2O$) and 200 µM $H_2O_2$ treated plants 12 hours after ablation. **(D)** Quantification of the relative *ERF115::GFP* fluorescence in wound-adjacent cells (normalized to the *ERF115::GFP* mean intensity on mock conditions), on mock conditions (green dots) or upon 200 µM $H_2O_2$ treatment (blue dots). Data are represented as relative fluorescence intensities of individual cells. Statistical significance was computed from a two-sample Wilcoxon test. **(E)** Quantification of the relative *ERF115::GFP* fluorescence in wound-adjacent cells (normalized to the *ERF115::GFP* mean intensity on mock conditions), in Wt on mock conditions (green dots) and upon 1 µM NAA treatment (orange dots) or in *coi1-2* mutant plants (blue and red dots, respectively). Data are represented as relative fluorescence intensities of individual cells on a logarithmic scale. Statistical significance was computed from a two-sample Wilcoxon test.
**(F-I)** Ethylene does not enhance ERF115 expression or restorative division rates. *ERF115::GFP* (green) expression in wound-adjacent cells upon mock **(F)** and 10µM ethylene precursor ACC **(G)**. **(H)** Quantification of the relative *ERF115::GFP* fluorescence in wound-adjacent cells (normalized to the *ERF115::GFP* mean intensity on mock conditions), on mock conditions (green dots) or upon 10 µM ACC treatment (yellow dots). Data are represented as relative fluorescence intensities of individual cells. Statistical significance was computed from a two-sample Wilcoxon test. **(C)** Restorative periclinal divisions rate (in %) of cortex and endodermal cells during mock and 10 µM ACC treatments. Data are represented as weighted mean (bar) and individual experiments (dots, area indicates sample size). Statistical significance was computed conditional logistic regression.
**(J-M)** *ERF115::GFP* (green) expression in wound-adjacent cells upon 25 µM ABA **(J)**, 1 µM EBL **(K)**, 1 µM Bz **(L)** or 40 µM SA treatment **(M)** 12 hours after ablation.

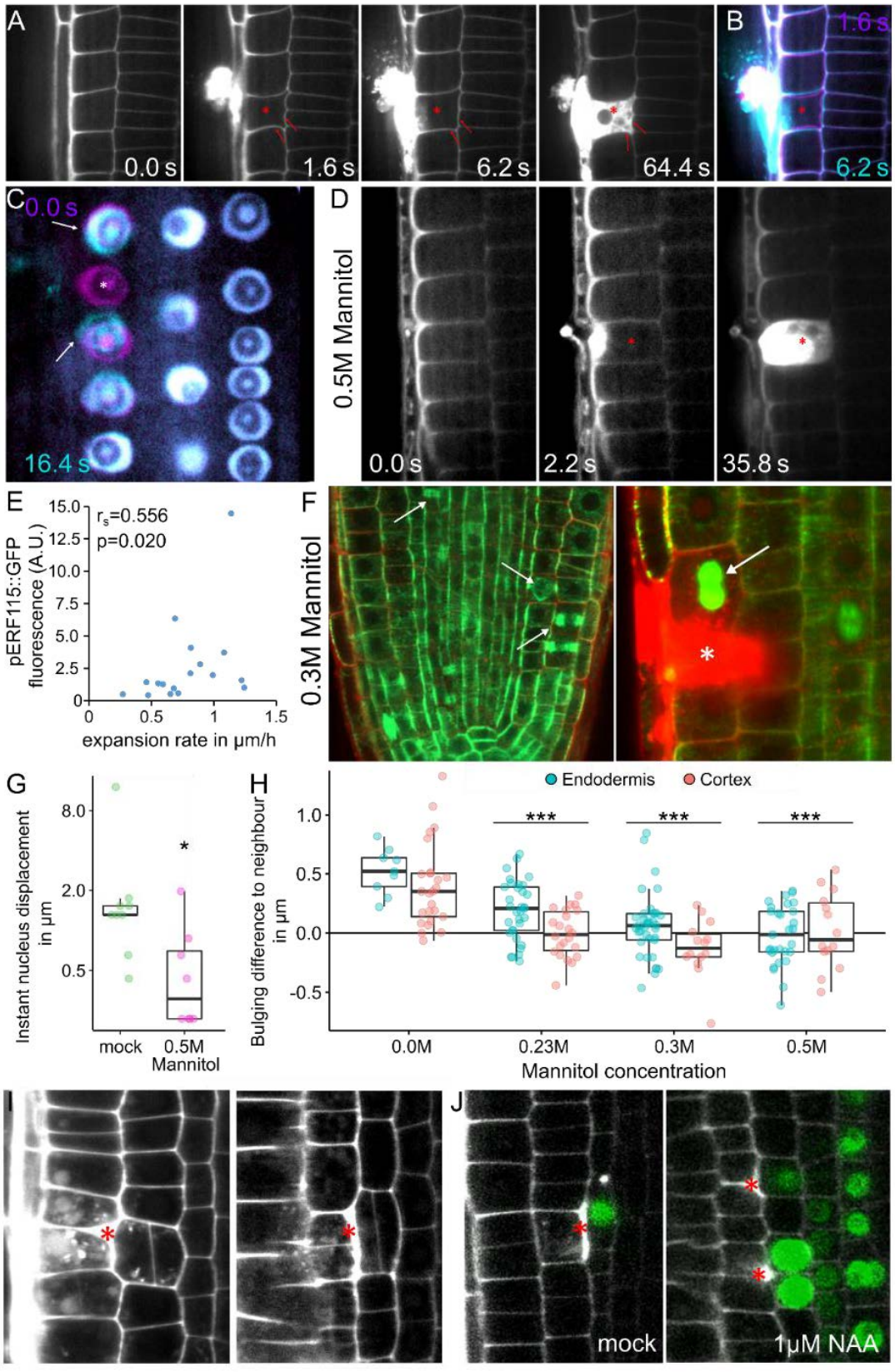


**Figure S7. Wound-triggered changes in tissue pressure**

**(A-B)** Ablation of a single cell causes release of cellular content and a reduction of turgor pressure in neighbouring cells. **(A)** Short term responses of ablated cells (asterisk) and their neighbours before ablation (0.0 s) and directly afterwards (1.6 s, 6.2 s and 64.4 s, from left to right). Released cellular content after ablation can be seen in white and red arrows mark neighbouring cell wall. Note that neighboring cell walls bulge immediately after ablation, retract afterwards and become bulged again after later time. **(B)** Overlay of two time points (1.6 s in magenta, and 6.2 s in cyan) after ablation (asterisk) showing the retraction of bulging of the neighbouring cells.
**(C)** Overlay of two time points (0 s in magenta, and 16.4 s in cyan) showing the displacement of nuclei in neighbouring cells (white arrows) after ablation of a single cell (asterisk).
**(D)** Short term responses of ablated cells (asterisk) and their neighbours before ablation (0.0 s) and directly afterwards (2.2 s, and 35.8 s, from left to right) upon 0.5 M Mannitol treatment. Note that release of cellular content and bulging are absent.
**(E)** Representation of the correlation between pre-mitotic expansion rates and *ERF115::GFP* fluorescence at the time of division. The Spearman correlation ($r_s$) and the statistical significance (p-value) are indicated in the top left corner.
**(F)** Anticlinal divisions are marked by *35S::MAP4-GFP* (green) stained spindles (white arrows) during hyperosmotic treatment (0.3 M Mannitol) in PI stained (red), undisturbed (left) and wound-adjacent cells (right, asterisk marks ablation).
**(G)** Representation of nucleus displacement immediately (max. 5 seconds) after ablation in cells upon mock (green) or 0.5M Mannitol treatment (purple). Note that nucleus displacement, i.e. cellular burst and collapse are merely absent from Mannitol treated samples. Statistical significance was computed from a two-sample Wilcoxon test.
**(H)** Turgor pressure driven bulging in wound adjacent cells is reduced upon Mannitol treatment. **(H)** Representation of the difference between bulging in wound adjacent to non-adjacent cells in endodermis (blue) and cortex cells (red) upon different mannitol concentration treatments. The distance of the bulging from inner neighbours (red) is subtracted from reference, non-adjacent cells (grey), resulting in positive (more bulging than in neighbours) or negative values (less bulging than neighbours). Statistical significance between 0.0M (mock) and the respective mannitol treatment was calculated from a two-sample Wilcoxon test.
**(I)** Periclinal cell divisions after harming the cell envelope between epidermis and cortex (left) or cortex and endodermis (right).
**(J)** *ERF115::GFP* expression after harming the cell envelope between cortex and endodermis in untreated (left) but or in 1 µM NAA treated plants (right)

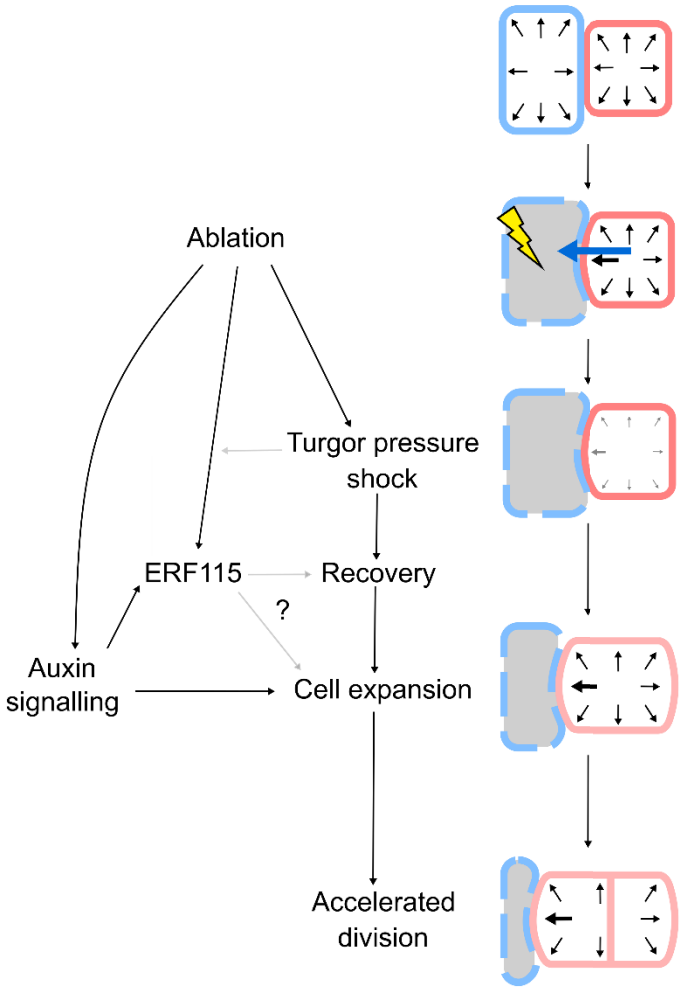


**Figure S8. Schematic summary of auxin effects on cell expansion, ERF115 expression and division rates**

Black arrows indicate turgor pressure driven forces on the cell wall, while a blue arrow indicates the loss of cellular content. A lighter colour of the cell wall indicates a presumable modification of the cell wall properties. The timeline of events runs from top to bottom.

**Supplementary Codes**

**Code S1. Statistical evaluation of binary data with Conditional Logistic Regression**

```
>library(survival)
>library(readxl)


>#provide data in df_test as in the following format:
># header: sample|exp|PD|ablated|type
># rows: name of sample (e.g.:"mock")|No. of repetition|No. of positive events (periclinal divisions)|No. of observed events (ablations)


>typ="endodermis" #type in cell type you want to observe
>test="treatment" #your test sample
>ctrl="mock" #your control sample

>#building of a dataframe with each observed event (each ablation, here called "cell") as a separate row (with incrementing numbers)
>df_test_test=df_test[df_test$sample == ctrl | df_test$sample == test,]
>df_test_test=df_test_test[df_test_test$type ==typ,]

>data1=as.data.frame(1:sum(df_test_test$ablated))
>colnames(data1)="cell"

>#each event gets assigned its respective repetition ("exp")
>exp=NULL
>for (i in 1:max(df_test$exp)) {
> exp=c(exp, rep(i,sum(df_test_test[df_test_test$exp==i,]$ablated)))
>}
>data1=cbind(data1,exp=exp)

>#each event gets assigned a binary value whether it triggered a positive (1, here a "PD") or a negative (0, here "no PD") event
>PD=NULL
>for (i in 1:max(df_test$exp)) {
>  PD=c(PD, rep(1,df_test_test[df_test_test$exp==i & df_test_test$sample==test ,]$PD), rep(0,df_test_test[df_test_test$exp==i & df_test_test$sample==test ,]$ablated-df_test_test[df_test_test$exp==i & df_test_test$sample==test ,]$PD),rep(1,df_test_test[df_test_test$exp==i & df_test_test$sample==ctrl ,]$PD), rep(0,df_test_test[df_test_test$exp==i & df_test_test$sample==ctrl ,]$ablated-df_test_test[df_test_test$exp==i & df_test_test$sample==ctrl ,]$PD))
```

```
>}
>data1=cbind(data1,PD=PD)

>#each event gets assigned a binary value whether it is a control sample (0, here" "not mut")
or test sample (1, here a "mut" for mutant)
>mut=NULL
>for (i in 1:max(df_test$exp)) {
>  mut=c(mut, rep(1,df_test_test[df_test_test$exp==i & df_test_test$sample==test
,]$ablated), rep(0,df_test_test[df_test_test$exp==i & df_test_test$sample==ctrl ,]$ablated))
>}
>data1=cbind(data1,mut=mut)

>#calculation considering each experiment individually (conditional)
>model <- clogit(data=data1, PD ~ mut + strata(exp))
>summary(model)
```

# Chapter 4

## Towards understanding the wound-responsive upstream signalling of ERF115 transcription factor

Lukas Hoermayer[1], Nicola Cavallari[1], Leonhard Spona[1], Eva Benkova[1] and Jiří Friml[1]

[1]Institute of Science and Technology Austria, 3400 Klosterneuburg, Austria

**Abstract**

Plants cannot evade uninhabitable growth conditions; hence rely on stress response signalling and adaption mechanisms. Wounding is a special threat to plants with their rigid body structures. Recently, our understanding of the underlying stress signalling mechanisms increased by the discovery of ERF115, a transcription factor specifically expressed in wound-responding cells. It functions in downstream stem cell replenishment to mediate tissue regeneration. However, how ERF115 expression is linked to wound perception remains elusive. In this study, we show how ROS signalling is crucial for the activation of ERF115. We identify ARF transcription factors facilitating the auxin-mediated enhancement of ERF115 expression and suggest PEPR receptor signalling as a novel regulatory pathway of ERF115. The here identified pathways are enhancers of the ERF115 expression, but likely do not participate in the direct wound perception. While the nature of the wound perception remains mysterious, our results suggest a complex signalling mechanism depending on histone-mediated transcription regulation and pathogen responses.

**Introduction**

Plant cells are restricted in movement and mobility by their cell wall. Hence, to organize in a tissue, plants developed specific mechanisms to position themselves via cell divisions (Dolan *et al.*, 1993; van den Berg *et al.*, 1995). A special form of this is the restorative division, which is induced after tissue damage or wounding and requires cell cycle progression and stem cell-like gene expression (Marhava *et al.*, 2019; Hoermayer *et al.*, 2020). Cells undergoing these restorative divisions specifically express ETHYLEN RESPONSE FACTOR 115 (ERF115) a wound-responsive transcription factor (TF) (Heyman *et al.*, 2013, 2016; Zhou *et al.*, 2019; Canher *et al.*, 2020; Hoermayer *et al.*, 2020). Known downstream targets of ERF115 include cell cycle progressing phytosulfokines and cell-expansion mediating expansins. It has a crucial role in quiescent centre (stem cell) replenishment and hence is supposed to act as a mediating factor between wound response and stem cell activity (Heyman *et al.*, 2013).

ERF115 belongs to a class of six homologues AP2/ERF transcription factors, of which ERF113 and ERF114, its closest homologues are also involved in cell cycle regulation and regeneration. ERF109, ERF110 and ERF111 play roles in stress responses and are partly responsible for stress recovery and development. Generally, those TFs seem to have

overlapping function, while their tissue and developmental context expression pattern is thought to be more specific to the individual genes (Heyman *et al.*, 2018). Hence, studying their function and expression regulation will provide novel insights into stress adaption and regeneration mechanisms in plants.

Here we identified multiple transcriptional enhancer pathways for the expression of ERF115. We show that ROS signalling, albeit being a secondary effector, is crucial for the activation of ERF115. We identify auxin response factors (ARFs) as the main component of the auxin-mediated enhancement of ERF115 expression and suggest a novel regulatory pathway of ERF115 expression, mediated by PEPR receptor signalling.

## Results

### ERF115 expression as a marker for wound signalling activity

ERF115 expression is extremely specific to wound-adjacent cells undergoing restorative divisions and the dominant negative *35S::ERF115-SRDX* line shows significantly reduced divisions upon wounding (Heyman *et al.*, 2016; Marhava *et al.*, 2019). Known downstream targets include PSK5, a mitogen triggering G1/S phase transitions, possibly mediating the division induction after ablation (Heyman *et al.*, 2013). To investigate this role of ERF115, we analysed periclinal division rates in the *erf115* single mutant. Notably, the mutant displayed no significant phenotype of division reduction (Fig. 1A). We investigated the mitotic status of cells in the same conditions and found that without ablation, 80% of cortex or endodermis cells express *HTR2::CDT1a-GFP* (Yin *et al.*, 2014), indicating S-Phase (Fig. 1B). Furthermore, multiple homologues of ERF115 (the closest being ERF114 and ERF113), have been proposed to act in similar or redundant functions (Heyman *et al.*, 2018). This implies that ERF115 is not crucial to the induction of restorative divisions, albeit being highly specific to wound-adjacent cells. Hence, studying its expression may reveal so-far unknown wound signalling components but might be limited in understanding restorative divisions.

ERF115 expression is induced upon ROS signalling (Kong *et al.*, 2018). We also have shown that $H_2O_2$ treatment enhances ERF115 activation after ablation (Hoermayer *et al.*, 2020). To further investigate the role of ROS signalling during activation of ERF115, we used a fluorescent dye, BES-$H_2O_2$-Ac (Maeda *et al.*, 2004), to stain for intracellular $H_2O_2$ accumulations. We found strong upregulation of the dye around wounds starting from couple of minutes (Fig. 1C). Hence, we investigated the effect of a $H_2O_2$ quencher – DMTU (Parker

*et al.*, 1985) – on ERF115 induction. We found a significant reduction of ERF115 expression in roots treated with 10 mM $H_2O_2$ (Fig. 1D & E). This suggests that $H_2O_2$ mediated ROS signalling is crucial for the activation of ERF115; however, exogenous application cannot trigger any wound-independent expression. This would suggest that ERF115 activation is facilitated by active ROS signalling, while the actual upstream components cannot be activated by $H_2O_2$ application alone.

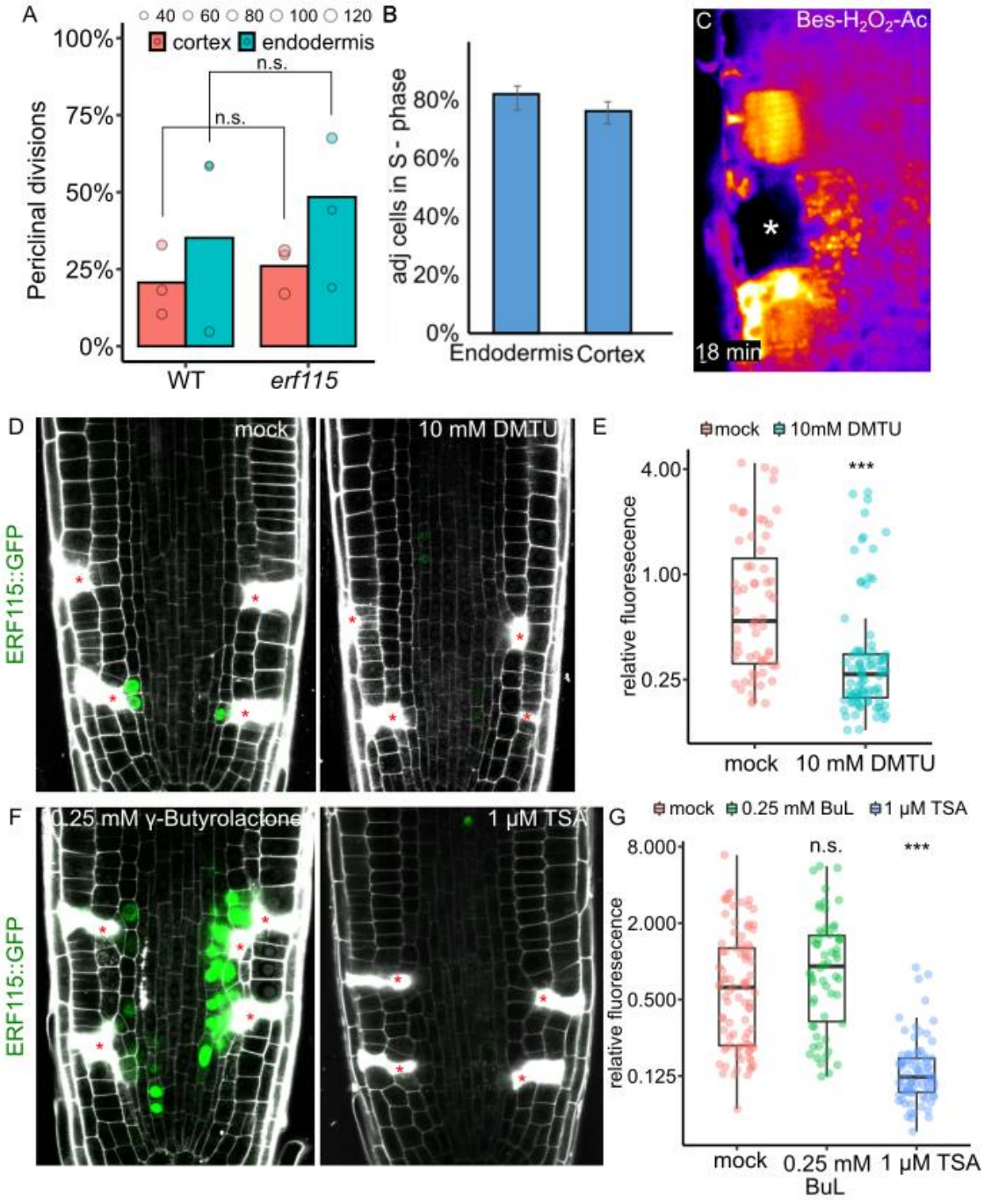

**Fig. 1 - ERF115 expression as a model for studying the wound signal**

**(A)** Quantification of relative restorative periclinal divisions rate (in %) of endodermal (blue) and cortex (red) cells, comparing *erf115* mutant with WT. Bars represent weighted means and dots represent individual experiments (area indicates sample size). Statistical significance was computed from conditional logistic regression. **(B)** Quantification relative amount of S-Phase cells (in %) in the Arabidopsis root meristem from *HTR2::CDT1a-GFP* seedlings. Data are represented as ratios (bars) and error bars indicate upper and lower quartiles.

**(C-E)** ERF115 expression is mediated by ablation-induced ROS. **(C)** Induction of fluorescent dye BES-$H_2O_2$-AC staining intracellular $H_2O_2$ 18min after ablation of epidermis cells. Note the strongest induction in direct wound-adjacent cells. (D) *ERF115::GFP* (green) expression in wound-adjacent cells in mock (left) and upon 10 mM DMTU treatment (right). Asterisks mark ablated cells. **(E)** Quantification of the relative *ERF115::GFP* fluorescence in wound-adjacent cells (normalized to the *ERF115::GFP* mean intensity on mock conditions), on mock conditions (red dots) or upon 10 mM DMTU treatment (blue dots). Data are represented as relative fluorescence intensities of individual cells on a log2 scale. Statistical significance was computed from a two-sample Wilcoxon test. **(F)** *ERF115::GFP* (green) expression in wound-adjacent cells upon 0.25 mM γ-Butyrolactone (left) and upon 1 µM TSA treatment (right). Asterisks mark ablated cells. **(G)** Quantification of the relative *ERF115::GFP* fluorescence in wound-adjacent cells (normalized to the *ERF115::GFP* mean intensity on mock conditions), on mock conditions (red dots), 0.25 mM γ-Butyrolactone (green dots) or upon 1 µM TSA treatment (blue dots). Data are represented as relative fluorescence intensities of individual cells on a log2 scale. Statistical significance was computed from a two-sample Wilcoxon test: BuL: p-value: 0.07, TSA: 2.2e-16.

---

These results suggest a more complex activation mechanism for ERF115. Recently, histone acetylation and methylation profiles after wounding in the root meristem have been published (Rymen *et al.*, 2019). Histones in the ERF115 promoter were shown to be specifically demethylated (de-repressed) and acetylated (activated) during wounding. Hence, we wanted to investigate the role of histone acetylation during ablation induced ERF115 expression. We used two chemical inhibitors: γ-Butyrolactone (BuL), an inhibitor of histone acetyl transferases (expression activators) (Biel *et al.*, 2004) and Trichostatin A (TSA), an inhibitor of histone deacetylases (expression inhibitors) (Yoshida *et al.*, 1990). Notably, BuL treatment during ablation showed a trend of increased expression of ERF115, while TSA treatment showed a significant decrease of ERF115 expression (Fig. 1F & G). These expression profiles are opposite to their primary function, which would imply that the chemicals are affecting an upstream component of ERF115. This component might be a more complex

mechanism of repression, which needs to be inhibited by histone deacetylation to allow ERF115 expression.

**Investigation of the ERF115 regulon**

Our results suggest a complex regulation system for the activation of ERF115 expression, based on histone acetylation and deacetylation, and might include a strong repressor gene. To investigate possible upstream regulators of ERF115, we analysed the promoter sequence with a bioinformatics tool called JASPAR (Fornes *et al.*, 2020). This tool predicts TF binding sites based on commonly known motifs in any DNA sequence. When we scanned the whole 2 kB promoter, we found a repetition of TF-cassettes in the sequence: The most predominant repetition was a certain hormone-regulated element (Fig. 2A) with jasmonate (JA)-related TFs (MYC2, MYC3, MYC4) (Carroll *et al.*, 2018), abscissic acid (ABA)-related TFs (ABF2, ABF3, ABI5, AIB) (Zhang *et al.*, 2019) and brassinosteroid (BL)-related TFs (BZR1, BZR2, BIM1/2/3, BEE1/2) (Gruszka, 2018). MYC2 and BZR1/2 binding sites in the ERF115 promoter have been found experimentally (Lee *et al.*, 2015; Zhou *et al.*, 2019). However, our previous results suggest that neither JA nor BL signalling alone are sufficient for ERF115 activation in the root meristem.

We identified another repetitive motif in the promoter with auxin-responsive elements (AuxREs) – binding sites for auxin-responsive ARF transcription factors (Fig. 2A). These four binding sites (one of them in the 5' untranslated region (UTR)) might facilitate the strong upregulation of ERF115 upon auxin treatment. Finally, we found a motif of accumulated binding sites for WRKY-TFs (called W-box) with ~25 possible TFs per W-box. This motif occurred 3 times in the promoter 1500 bp and more upstream of the transcriptional start site (TSS) (Fig. 2A). WRKY-TFs are components of stress, wound and pathogen signalling and might be key components of the upstream wound signalling (Chen *et al.*, 2019).

**Investigation of the ERF115 co-expression transcriptome**

ERF115 is component of both, wound signalling and salt stress response (Heyman *et al.*, 2016; Ikeuchi *et al.*, 2016; Krishnamurthy *et al.*, 2017). To understand this possible link and to investigate which genes accompany the specific induction of ERF115, we analysed microarray datasets with the Genevestigator bioinformatics tool (Hruz *et al.*, 2008). We found five "perturbation" conditions in which ERF115 and its closest homologues are specifically

upregulated: two salt studies, one osmotic, one draught, and one Pep2 treatment study (Fig. 2B). We analysed which genes are commonly upregulated in all five conditions and found a list of 39 genes (Fig. 2C). The list consists of 2/3 known genes, including ERF113, a homologue of ERF115 (Heyman *et al.*, 2018). GO analysis via pantherdb (Fig. 2D) (Mi *et al.*, 2021) shows this gene list is highly enriched for auxin biosynthesis genes, defence response genes (especially oomycete defence) and ROS detoxification genes. This confirms our previous observation that ROS signalling is a crucial component of ERF115 activation. Further, it would suggest again the involvement of WRKY TFs in the wound signalling after laser ablation. Finally, auxin biosynthesis appears to be tightly linked with ERF115 expression, in accordance with our observation of increased auxin accumulation during restorative divisions and the strong interconnection of auxin and ERF115 expression (Canher *et al.*, 2020; Hoermayer *et al.*, 2020).

A

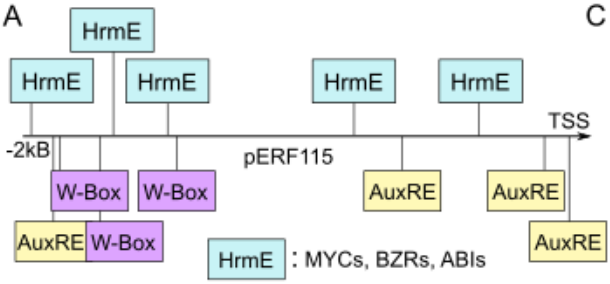


B

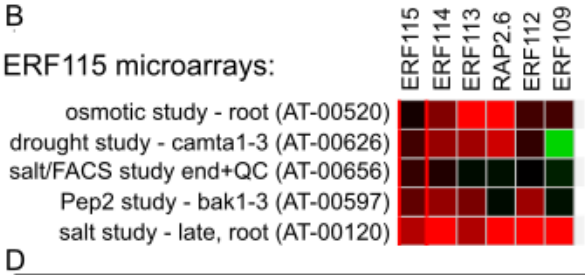


C

| | | |
|---|---|---|
| ERF113 | ASA1 | AT2G39050 |
| MYB112 | ASB1 | AT1G24807 |
| WRKY28 | ASB2 | AT1G24909 |
| WRKY45 | CYP81F2 | AT1G25083 |
| ZIFL1 | CYP79B2 | AT1G25155 |
| LECRK57 | UGT87A2 | AT1G74360 |
| LECRK58 | UGT73C7 | AT2G04400 |
| PLC1 | GSTU4 | AT3G16530 |
| GSTF7 | SSL11 | AT2G15760 |
| GSTF6 | SSL7 | AT1G60730 |
| PER54 | BGLU24 | AT2G39980 |
| STR18 | GLIP1 | ATJRG21 |
| ABCG16 | STP13 | ATTI1 |

D

| GO biological process complete | raw p-value |
|---|---|
| regulation of auxin biosynthetic process (GO:0010600) | 2.09E-04 |
| defense response by callose deposition in cell wall (GO:0052544) | 2.66E-04 |
| defense response by cell wall thickening (GO:0052482) | 2.97E-04 |
| induced systemic resistance (GO:0009682) | 1.42E-05 |
| toxin catabolic process (GO:0009407) | 7.48E-09 |
| tryptophan biosynthetic process (GO:0000162) | 4.76E-08 |
| lateral root formation (GO:0010311) | 6.57E-05 |
| defense response by callose deposition (GO:0052542) | 6.05E-04 |
| defense response to oomycetes (GO:0002229) | 1.53E-04 |
| glutathione metabolic process (GO:0006749) | 8.43E-08 |

**Fig. 2 – Investigation of the ERF115 regulon**
**(A)** Transcription factor motifs within the ERF115 promoter. JASPAR analysed TF binding sites for WRKY transcription factors (pink), ARF transcription factors (yellow) and other hormonal regulators (brassinosteroid-related transcription factors, jasmonate-related transcription factors, ABA-related transcription factors, blue).
**(B-D)** Co-expression data set for ERF115 and homologues. **(B)** Microarray experiments with strongest upregulation of ERF115 and its closest homologues as identified from Genevestigator. **(C)** List of all genes commonly upregulated within the ERF115 microarrays. **(D)** Gene Ontology results from the list of commonly expressed genes as calculated by pantherdb.org

---

## ERF115 expression is mediated by ARFs and PEPR receptors

Our results suggest that the auxin effect on ERF115 expression is mediated by ARF transcription factors via the binding of AuxREs. To test this, we mutated the ERF115 promoter at the position of the predicted AuxREs (with poly-adenine substitution) and analysed the ERF115 expression. Notably we found that the strong induction of ERF115 upon auxin treatment was abolished and that the ERF115 expression was generally reduced (Fig. 3A & B). In accordance with our previous results, this links ERF115 expression directly to the canonical TIR1/AFB mediated auxin perception and ARF-dependent transcription (Dharmasiri *et al.*, 2005; Lavy and Estelle, 2016) and rules out the dependency on other, auxin-activated, upstream signalling components. This finally shows that auxin signalling acts as a (major) enhancer of ERF115 signalling but is not involved in the primary perception of the wound signal.

To identify the wound signal, we chose to work with the *pepr1 pepr2* (*pepr1;2*) double mutant, which is deficient in triggering defence responses after ablation-induced $Ca^{2+}$ waves (Hander *et al.*, 2019). We crossed ERF115::GFP with the *pepr1;2* double mutant and observed expression strength after ablation. We found a significantly reduced ERF115 expression in the mutant compared to WT (Fig. 3C & D). However, expression was not completely abolished. Again, this implies that PEPR signalling is not the primary wound signal.

These results suggest that ERF115 expression relies on a plethora of enhancer components, mainly auxin signalling, JA and BL signalling. Additionally, we have identified a novel component: PEPR-mediated signalling (Fig. 3E).

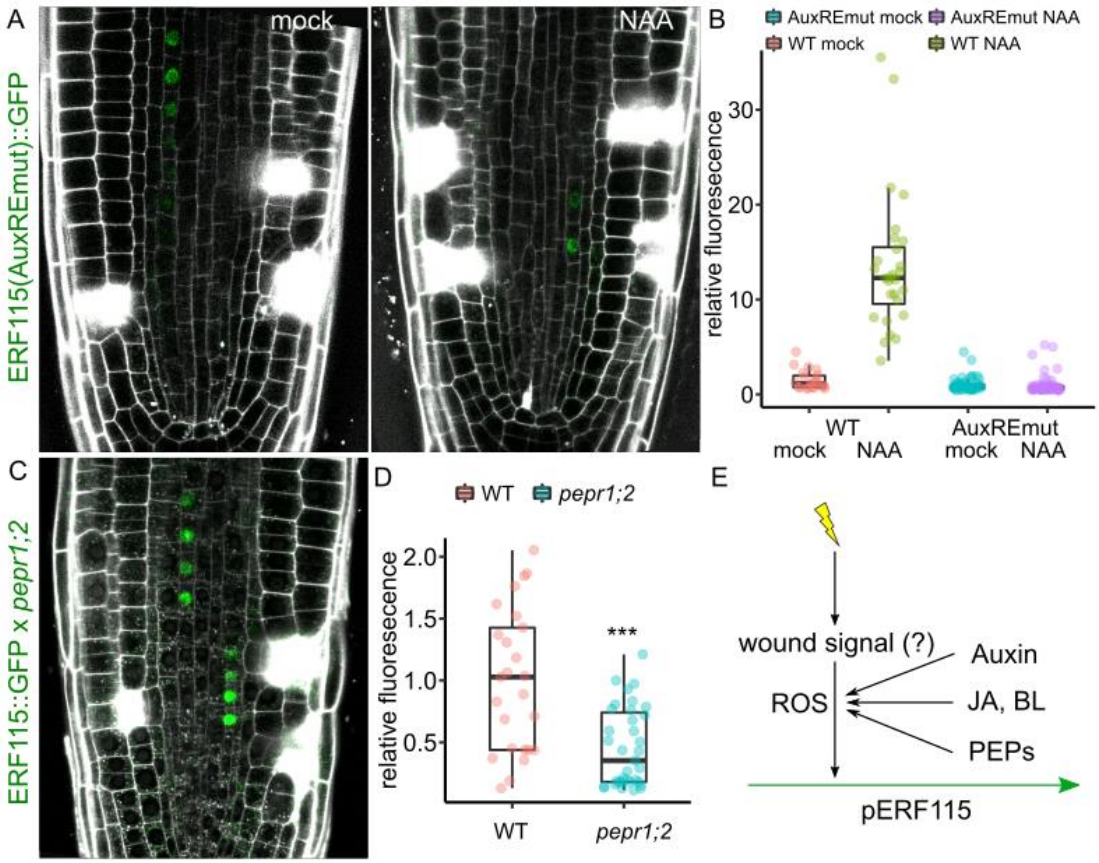


**Fig. 3 – Upstream regulators of ERF115 expression**

**(A-B)** ERF115 expression is mediated by auxin via ARF transcription factors. **(A)** *ERF115(mutAuxRE)::GFP* (green) expression in wound-adjacent cells in mock (left) and upon 1 µM NAA treatment (right). Asterisks mark ablated cells. **(B)** Quantification of the relative *GFP* fluorescence in wound-adjacent cells (normalized to the *ERF115(mutAuxRE)::GFP* mean intensity on mock conditions), in *ERF115(WT)::GFP* on mock (red dots) and 1 µM NAA (green) conditions or in *ERF115(mutAuxRE)::GFP* on mock (blue) and 1 µM NAA (violet) conditions. Data are represented as relative fluorescence intensities of individual cells.

**(C-D)** ERF115 expression depends on PEPR signalling. **(C)** *ERF115::GFP* (green) expression in wound-adjacent cells in *pepr1;2* double mutant. Asterisks mark ablated cells. **(D)** Quantification of the relative *GFP* fluorescence in wound-adjacent cells (normalized to the *ERF115::GFP* mean intensity in WT), in WT (red dots) and *pepr1;2* double mutant (blue dots). Data are represented as relative fluorescence intensities of individual cells on a log2 scale.

**(E)** Scheme of the activation of ERF115 expression. The wound signal, which triggers the expression remains unknown, while enhancers like auxin, brassinosteroids (BL), jasmonate (JA) and PEPs increase the expression after wounding.

**Discussion**

In this study, we analysed the activation mechanism of ERF115 to increase our knowledge about the primary wounding signal. We found a strong connection of ERF115 expression with $H_2O_2$ accumulations after wounding, auxin signalling and PEPR-mediated signalling. While the underlying mechanism for activation of ERF115 remains elusive, our results provide some initial insights.

Expression analysis after TSA treatment suggests the existence of a repressor complex, which needs to be downregulated transcriptionally by histone deacetylation. Alternatively, the strong downregulation upon TSA treatment could be a result of off-target effects, e.g. on DNA-damage components, ROS signalling or interference with cell cycle transitions (Zhang *et al.*, 2007; Rosa *et al.*, 2014; Wójcikowska *et al.*, 2018). However, in plants TSA treatment showed increased auxin and ROS accumulation - two activators of ERF115 - suggesting a rather direct effect of TSA on ERF115 inhibition.

The co-expression data of oomycete defence genes with ERF115 and its homologues suggest a so-far undiscovered pathway of wound signalling. Oomycete defence is possibly activated by perception of endogenous plant-derived patterns (Raaymakers and Van Den Ackerveken, 2016). These include extracellular ATP, and Peps perceived by PEPR receptors. While there is little genetic material available to study ATP perception, we have identified PEPRs as enhancer components for ERF115 expression. Another enriched process in ERF115 co-expression data was auxin biosynthesis. Notably, these were ASA1, ASB1 and CYP79B2; genes involved in tryptophan biosynthesis and IAOx synthesis, respectively (Ruiz Rosquete, Barbez and Kleine-Vehn, 2012; Crane *et al.*, 2019). Notably, CYP79B2 is also part of the oomycete defence response and its product IAOx is a precursor for defence related compounds (Schlaeppi *et al.*, 2010). This suggests that after wounding, auxin production including precursors and side metabolites, might be triggered by defence mechanisms similar to pathogen-induced responses.

In conclusion, our results suggest a pathogen derived stress response as the main trigger for ERF115 expression. Hence, further investigation of ERF115 expression with genetic and pharmacological perturbation of pathogen responses will reveal new upstream mechanisms for wound signalling. Finally, forward genetic screens with the ERF115 marker line and single cell

sequencing or single cell ChIP experiments might give even broader insight into the wound-responsive signalling and perception mechanisms.

**References:**

van den Berg, C. *et al.* (1995) 'Cell fate in the Arabidopsis root meristem determined by directional signalling', *Nature*. Nature Publishing Group, 378(6552), pp. 62–65. doi: 10.1038/378062a0.

Biel, M. *et al.* (2004) 'Design, Synthesis, and Biological Evaluation of a Small-Molecule Inhibitor of the Histone Acetyltransferase Gcn5', *Angewandte Chemie International Edition*. John Wiley & Sons, Ltd, 43(30), pp. 3974–3976. doi: 10.1002/ANIE.200453879.

Canher, B. *et al.* (2020) 'Rocks in the auxin stream: Wound-induced auxin accumulation and ERF115 expression synergistically drive stem cell regeneration', *Proceedings of the National Academy of Sciences*. National Academy of Sciences, 117(28), pp. 16667–16677. doi: 10.1073/PNAS.2006620117.

Carroll, P. A. *et al.* (2018) 'The MYC transcription factor network: balancing metabolism, proliferation and oncogenesis', *Frontiers of Medicine 2018 12:4*. Springer, 12(4), pp. 412–425. doi: 10.1007/S11684-018-0650-Z.

Chen, X. *et al.* (2019) 'WRKY transcription factors: evolution, binding, and action', *Phytopathology Research 2019 1:1*. BioMed Central, 1(1), pp. 1–15. doi: 10.1186/S42483-019-0022-X.

Crane, R. A. *et al.* (2019) 'Negative Regulation of Age-Related Developmental Leaf Senescence by the IAOx Pathway, PEN1, and PEN3', *Frontiers in Plant Science*. Frontiers Media S.A., 10. doi: 10.3389/FPLS.2019.01202.

Dharmasiri, N. *et al.* (2005) 'Plant development is regulated by a family of auxin receptor F box proteins', *Developmental Cell*, 9(1), pp. 109–119. doi: 10.1016/j.devcel.2005.05.014.

Dolan, L. *et al.* (1993) 'Cellular organisation of the Arabidopsis thaliana root', *Development*, 119(1), pp. 71–84.

Fornes, O. *et al.* (2020) 'JASPAR 2020: update of the open-access database of transcription factor binding profiles', *Nucleic Acids Research*. Oxford Academic, 48(D1), pp. D87–D92. doi: 10.1093/NAR/GKZ1001.

Gruszka, D. (2018) ‘Crosstalk of the Brassinosteroid Signalosome with Phytohormonal and Stress Signaling Components Maintains a Balance between the Processes of Growth and Stress Tolerance’, *International Journal of Molecular Sciences 2018, Vol. 19, Page 2675*. Multidisciplinary Digital Publishing Institute, 19(9), p. 2675. doi: 10.3390/IJMS19092675.

Hander, T. *et al.* (2019) ‘Damage on plants activates Ca2+-dependent metacaspases for release of immunomodulatory peptides.’, *Science (New York, N.Y.)*. American Association for the Advancement of Science, 363(6433), p. eaar7486. doi: 10.1126/science.aar7486.

Heyman, J. *et al.* (2013) ‘ERF115 Controls Root Quiescent Center Cell Division and Stem Cell Replenishment’, *Science*. American Association for the Advancement of Science, 342(6160), pp. 860–863. doi: 10.1126/SCIENCE.1240667.

Heyman, J. *et al.* (2016) ‘The heterodimeric transcription factor complex ERF115–PAT1 grants regeneration competence’, *Nature Plants*, 2(11), p. 16165. doi: 10.1038/nplants.2016.165.

Heyman, J. *et al.* (2018) ‘Emerging role of the plant ERF transcription factors in coordinating wound defense responses and repair’. doi: 10.1242/jcs.208215.

Hoermayer, L. *et al.* (2020) ‘Wounding-induced changes in cellular pressure and localized auxin signalling spatially coordinate restorative divisions in roots’, *Proceedings of the National Academy of Sciences*. National Academy of Sciences, 117(26), pp. 15322–15331. doi: 10.1073/PNAS.2003346117.

Hruz, T. *et al.* (2008) ‘Resource Review Genevestigator V3: A Reference Expression Database for the Meta-Analysis of Transcriptomes’, *Advances in Bioinformatics*. Hindawi Publishing Corporation. doi: 10.1155/2008/420747.

Ikeuchi, M. *et al.* (2016) ‘Plant regeneration: Cellular origins and molecular mechanisms’, *Development (Cambridge)*. Company of Biologists Ltd, pp. 1442–1451. doi: 10.1242/dev.134668.

Kong, X. *et al.* (2018) ‘PHB3 Maintains Root Stem Cell Niche Identity through ROS-Responsive AP2/ERF Transcription Factors in Arabidopsis’, *Cell Reports*. Elsevier, 22(5), pp. 1350–1363. doi: 10.1016/J.CELREP.2017.12.105.

Krishnamurthy, P. *et al.* (2017) 'Transcriptomics analysis of salt stress tolerance in the roots of the mangrove Avicennia officinalis', *Scientific Reports*. Nature Publishing Group, 7(1). doi: 10.1038/s41598-017-10730-2.

Lavy, M. and Estelle, M. (2016) 'Mechanisms of auxin signaling', *Development (Cambridge)*. Company of Biologists Ltd, 143(18), pp. 3226–3229. doi: 10.1242/dev.131870.

Lee, H.-S. *et al.* (2015) 'Brassinazole resistant 1 (BZR1)-dependent brassinosteroid signalling pathway leads to ectopic activation of quiescent cell division and suppresses columella stem cell differentiation.', *Journal of experimental botany*. Oxford University Press, 66(15), pp. 4835–49. doi: 10.1093/jxb/erv316.

Maeda, H. *et al.* (2004) 'Fluorescent Probes for Hydrogen Peroxide Based on a Non-Oxidative Mechanism', *Angewandte Chemie International Edition*. John Wiley & Sons, Ltd, 43(18), pp. 2389–2391. doi: 10.1002/ANIE.200452381.

Marhava, P. *et al.* (2019) 'Re-activation of Stem Cell Pathways for Pattern Restoration in Plant Wound Healing', *Cell*. Cell Press, 177(4), pp. 957-969.e13. doi: 10.1016/j.cell.2019.04.015.

Mi, H. *et al.* (2021) 'PANTHER version 16: a revised family classification, tree-based classification tool, enhancer regions and extensive API', *Nucleic Acids Research*. Oxford Academic, 49(D1), pp. D394–D403. doi: 10.1093/NAR/GKAA1106.

Parker, N. B. *et al.* (1985) 'Hydrogen peroxide causes dimethylthiourea consumption while hydroxyl radical causes dimethyl sulfoxide consumption in vitro', *Journal of Free Radicals in Biology & Medicine*. Pergamon, 1(5–6), pp. 415–419. doi: 10.1016/0748-5514(85)90155-2.

Raaymakers, T. M. and Van Den Ackerveken, G. (2016) 'Extracellular recognition of oomycetes during biotrophic infection of plants', *Frontiers in Plant Science*. Frontiers Research Foundation, 7, p. 906. doi: 10.3389/fpls.2016.00906.

Rosa, S. *et al.* (2014) 'Cell differentiation and development In Arabidopsis are associated with changes in histone dynamics at the single-cell level', *Plant Cell*. American Society of Plant Biologists, 26(12), pp. 4821–4833. doi: 10.1105/TPC.114.133793.

Ruiz Rosquete, M., Barbez, E. and Kleine-Vehn, J. (2012) 'Cellular auxin homeostasis: Gatekeeping is housekeeping', *Molecular Plant*. Oxford University Press, 5(4), pp. 772–786.

doi: 10.1093/MP/SSR109.

Rymen, B. *et al.* (2019) ‘Histone acetylation orchestrates wound-induced transcriptional activation and cellular reprogramming in Arabidopsis’, *Communications Biology 2019 2:1*. Nature Publishing Group, 2(1), pp. 1–15. doi: 10.1038/s42003-019-0646-5.

Schlaeppi, K. *et al.* (2010) ‘Disease resistance of Arabidopsis to Phytophthora brassicae is established by the sequential action of indole glucosinolates and camalexin’, *Plant Journal*. Plant J, 62(5), pp. 840–851. doi: 10.1111/j.1365-313X.2010.04197.x.

Wójcikowska, B. *et al.* (2018) ‘Trichostatin a triggers an embryogenic transition in arabidopsis explants via an auxin-related pathway’, *Frontiers in Plant Science*. Frontiers Media S.A., 9, p. 1353. doi: 10.3389/fpls.2018.01353.

Yin, K. *et al.* (2014) ‘A dual-color marker system for in vivo visualization of cell cycle progression in Arabidopsis’, *The Plant Journal*. John Wiley & Sons, Ltd, 80(3), pp. 541–552. doi: 10.1111/TPJ.12652.

Yoshida, M. *et al.* (1990) ‘Potent and specific inhibition of mammalian histone deacetylase both in vivo and in vitro by trichostatin A.’, *Journal of Biological Chemistry*. Elsevier, 265(28), pp. 17174–17179. doi: 10.1016/S0021-9258(17)44885-X.

Zhang, J. *et al.* (2019) ‘Precise control of ABA signaling through post-translational protein modification’, *Plant Growth Regulation 2019 88:2*. Springer, 88(2), pp. 99–111. doi: 10.1007/S10725-019-00492-4.

Zhang, Y. *et al.* (2007) ‘Attenuated DNA damage repair by trichostatin a through BRCA1 suppression’, *Radiation Research*. Radiat Res, 168(1), pp. 115–124. doi: 10.1667/RR0811.1.

Zhou, W. *et al.* (2019) ‘A Jasmonate Signaling Network Activates Root Stem Cells and Promotes Regeneration’, *Cell*. Cell Press, 177(4), pp. 942-956.e14. doi: 10.1016/J.CELL.2019.03.006.

## METHODS

### Plant material

*Arabidopsis thaliana* (L.) Heynh (accession Columbia-0) was used in this work (Wt). The following transgenic *Arabidopsis thaliana* lines and mutant lines were described previously: *ERF115::NLS-GFP-GUS* (*ERF115::GFP*, (Heyman et al. 2016)), *pepr1 pepr2* (Hander et al. 2019). *ERF115::NLS-GFP-GUS* was introduced into the *pepr1;2* background by genetic crossing. *pepr1 pepr2* seedlings were identified by PCR-cased genotyping in F2 and F3 generations *ERF115::NLS-GFP-GUS* carrying plants were identified in F2, F3 and F4 generations by kanamycin resistance.

### Molecular cloning

For the *ERF115(mutAuxRE)::GFP* reporter construct, the 2,000 bp promoter upstream of ERF115 (Heyman et al. 2013) was synthesized by invitrogen with mutated AuxREs: multiple adenines were introduced instead of the WT base sequence at positions -1911bp (9xA), -679bp (8xA), -174bp (5xA) and -51bp (10xA) upstream of the transcriptional start site. The so generated promoter was inserted into the pMK7S*NFm14GW plasmid through Gateway recombination and subsequently introduced into *A. thaliana* plants through *Agrobacterium tumefaciens*-mediated transformation. Positive transformants were selected by kanamycin resistance and confirmed by PCR-based genotyping and sequencing.

### Growth conditions

Seeds of *A. thaliana* were sown on Murashige and Skoog (1/2MS) medium (Duchefa) with 1% sucrose and 1% agar, stratified for 1-2 d and grown for 3-5 d at 21°C in a 16 h light/8 h dark cycle.

### Pharmacological treatments

Seedlings were transferred on solid MS medium containing the indicated chemicals: propidium iodide (PI, 10 μM, Sigma-Aldrich or Thermofisher), Naphthylacetic acid (NAA, Duchefa Biochemie, final concentration as indicated - if nothing indicated: 1 μM), Dimethyl thiourea

(DMTU, Sigma-Aldrich, final concentration: 10 mM), γ-Butyrolactone (BuL, Sigma Aldrich, final concentration 0.25 mM), Trichostatin A, (TSA, Sigma Aldrich, final concentration: 1 µM), BES-$H_2O_2$-Ac (Fujifilm Wako, final concentration: 40µM).

**Sample preparation**

Seedlings were placed on chambered cover glass (VWR, Kammerdeckgläser, Lab-Tek™, Nunc™ - eine kammer, catalog number: 734-2056) as described (Marhavý and Benková 2015). With the chamber, a block of solid MS media was cut out and propidium iodide solution was added. After the liquid soaked in, 10-15 seedlings were transferred to the agar and the block was inserted into the chamber.

**Confocal imaging and image processing**

Confocal imaging was performed with Zeiss LSM700/800 inverted microscopes using 20x or 40x objectives or a Spinning disk imaging system. Detection of fluorescence signals was carried out for GFP (excitation 488 nm, emission 507 nm), YFP (excitation 514 nm, emission 527 nm) and PI (excitation 536 nm, emission 617 nm). For fixed time point measurements, samples were observed 12 hours after ablation or at indicated time points. Images were analyzed using the ImageJ (NIH; http://rsb.info.nih.gov/ij) and Zeiss Zen 2.3 "Black" or "Blue" software. Where necessary, images were processed by adjusting contrast and lightness.

**Spinning disk imaging**

For the observation of immediate effects during/after ablation, an Andor spinning disk microscopy (CSU X-1, camera iXon 897 [back-thinned EMCCD], FRAPPA unit and motorized piezo stage) 63× water immersion objective was used. Videos were acquired with 1 focal plane, every 1 second, for <30 min. All images in a single experiment were captured with the same settings.

**UV laser ablation setup**

The UV laser ablation was performed as described in ref. (Marhava et al. 2019; Marhavý et al. 2016) which are based on the layout published in ref. (Colombelli, Grill, and Stelzer 2004).

**Prediction of transcription factor binding sites**

TF binding sites in the ERF115 promoter were analysed using JASPAR (Fornes et al. 2020). The 2kB promoter region of ERF115 was analysed using the "Scan" tool selecting all available TF motifs from *Arabidopsis thaliana*. A threshold of 85% confidence was applied, the number of all TF binding motifs was counted and motifs that occurred equally or less often than in the promoter of a random reference gene (At4g02980) were removed. Visual examination of the remaining motifs showed spots of increased binding for 3 different sets of TFs which were then mapped on the whole promoter.

**Analysis of microarrays**

Expression of ERF115 and homologues was analysed with Genevestigator (Hruz et al. 2008) using the "Hierarchical Clustering" tool. The 5 microarrays with to strongest upregulation in most of the homologues have been chosen for further analysis. Using the "Gene search – Perturbations" tool, genes commonly upregulated between those sets have been identified. The set of resulting genes was analysed using pantherdb.org (Mi et al. 2021) gene ontology search and the 10 most specific, independent GO terms have been chosen for representation.

**Quantification and statistical significance**

Asterisks illustrate the p-value: $p < 0.001$ is ***, $p < 0.01$ is ** and $p < 0.05$ is *

**Periclinal divisions**

For counting the (absolute) amount of periclinal divisions after ablation, the amount of cells with and without periclinal divisions (division plane parallel or oblique to the growth axis) adjacent to ablaitons were recorded and the ratio of positive to all events was calculated.

As in ref. (Marhava et al. 2019) the binary data was analysed using conditional logistic regression (Campbell 2013; Kleinbaum and Klein 2010), pairing the data within individual experiments. The statistical significance was computed using the clogit function from the R package "survival".

**Fluorescence intensity in fixed time point experiments**

For quantitative measurements of ERF115::GFP expression, the signal intensity of all wound adjacent (inner) cells within one focal plane was measured using ImageJ in the green channel. Each obtained value from one experiment/repetition was divided by the mean fluorescence intensity in the reference sample (untreated WT) to obtain relative fluorescence intensities.
The statistical significance was calculated using a two-sample Wilcoxon test between the reference and the sample values with wilcox.test() from R.

For qualitative data of S-phase ratio, the amount of cells with and without a visible *HTR2::CDT1a-GFP* accumulation in the nucleus was counted and the ratio of positive to all observed events was computed. For the error bars, the borders of the upper and lower quartiles were calculated assuming a beta distribution of the binary values with qbeta() from R.

# Chapter 5

## Cell expansion driven stretching defines division orientation through Microtubule arrays in the Arabidopsis root meristem

Lukas Hoermayer[1], Saiko Yoshida[1,3], Juan Carlos Montesinos[1], Eva Benková[1], Petra Marhava[1,2] and Jiří Friml[1]

[1]Institute of Science and Technology Austria, 3400 Klosterneuburg, Austria

[2]Current address: University of Lausanne, DBMV, CH-1015 Lausanne, Switzerland

[3]Current address: Max Planck Institute for Plant Breeding Research, 50829 Carl-von-Linné - Weg 10, Cologne, Germany

**Abstract**

Unlike animals, plants do not have mobile cells to heal wounds. Hence, they have evolved regeneration mechanisms that rely mainly on directional cell expansion and oriented cell divisions. However, what drives the exact positioning and execution of these programs is not understood. To unravel these events, we coupled UV-laser ablation in the root meristem with high-resolution 3D visualisation and long-term imaging at the vertical stage microscopy. By this, we revealed that division plane selection is independent of wound-adjacency and occurs through tissue stretching and expansion. Furthermore, we showed instant tissue deformation after ablation, mainly in inner-lying cells. We also show that expansion is crucial for microtubule array formation and reveal transient microtubule reorientation during restorative divisions. Finally, using a micropipette aspiration assay, we demonstrate that fast stretching of cells induces microtubule bundle formation quickly and reversibly. In conclusion, our results suggest that altered stretching of cells because of wounding changes microtubule stability and subsequently division planes. While the effect of mechanical tension on microtubules remains elusive, our data reveals novel insights in microtubule stability and orientation in the root meristem, a tissue with a yet undefined set of mechanical forces.

## Introduction

Plant cells are fixed in their position within a tissue because they are surrounded by a cell wall matrix that limits cell expansion and glues them towards their neighbours. Hence, wound healing in plants tissues relies on oriented cell expansion and subsequent division to achieve fast and efficient closure of the wound (Bloch, 1941; Hoermayer and Friml, 2019; Ikeuchi *et al.*, 2019). Recently, we introduced a system of cell ablation in the root meristem, which mimics wound responses and allows the investigation of tissue restoration on a cellular level, in situ and in real time (Marhava *et al.*, 2019; Hoermayer *et al.*, 2020). These studies revealed a phenomenon called restorative divisions, where cells predominately at the inner adjacent side of the wound change division planes to invade and replace the removed cells through subsequent cell expansion and cell fate acquisition. Furthermore, cells directly adjacent to ablated cells undergo certain wound responses: accumulation of auxin and expression of the wound-responsive transcription factor ERF115 (Heyman *et al.*, 2013, 2016; Zhou *et al.*, 2019;

Canher *et al.*, 2020; Hoermayer *et al.*, 2020). Both the regeneration capacity and the wound responses are highly linked to turgor pressure regulation and controlling of cell expansion followed by the wounding. However, how the cells around the wound trigger division plane switches and how this is connected to cell expansion is not understood.

Division plane establishment in plants is a crucial process involved in all developmental stages starting from embryogenesis to final differentiation of leaves and flowers (Abrash and Bergmann, 2009; Rasmussen and Bellinger, 2018). Owing to their immobility, plant cells will receive different positional information depending on where they are placed, linking division plane selection with tissue development and cell type specification (Dolan *et al.*, 1993; van den Berg *et al.*, 1995). During mitosis the new cell wall that forms between the two daughters is deposited at a pre-defined position, called the cortical division zone (CDZ) (Damme, Vanstraelen and Geelen, 2007). In G2 phase of the cell cycle, the CDZ is decorated by tight bundles of microtubules called the pre-prophase band (PPB) (Rasmussen, Humphries and Smith, 2011). While the importance of the PPB for robust positioning of the new cell wall is evident, its role in defining the CDZ is disputed (Schaefer *et al.*, 2017). Many factors for the establishment of the CDZ have been presented, including hormones like auxin (Rybel *et al.*, 2014; Yoshida *et al.*, 2014; Shao and Dong, 2016), transcription factors (Koizumi, Hayashi and Gallagher, 2012; De Rybel *et al.*, 2013) or simple cell geometry (Besson and Dumais, 2011; Louveaux and Hamant, 2013). Recently, studies emerged linking division plane selection with mechanical tissue tension and subsequent microtubule orientation (Hamant *et al.*, 2008, 2019; Louveaux *et al.*, 2016). In the shoot apical meristem, the dome shape impedes certain mechanical tensions on the cells in the upper layer. The microtubule pattern follows the predicted stress pattern. Local changes in the dome-shape derived tension through ablations or pharmacological treatments lead to a shift of microtubule patterns accordingly. However, how cells can sense those mechanical signals remains mysterious.

Here we show that the division plane orientation follows strictly the direction of cell expansion. Furthermore, we show that the whole tissue deforms upon wounding, which is transmitted into division plane switches further away from the wound area. We also show an asymmetry of inner vs. outer cells deformations after ablation. We also observe an effect of auxin on inhibiting cell expansion in the root meristem and henceforth destabilizing microtubules. During restorative divisions, we describe that transverse microtubule arrays disappear and newly form in perpendicular direction at the same time. Finally, we show that stretching - as occurring during the wounding or externally applied through a micropipette –

induces microtubule bundle formation. This suggests that cell expansion and subsequent stretching forces are required for establishing division plane orientations in the root meristem.

**Results:**

**Division plane cannot be re-positioned after PPB establishment**

The division plane switch during restorative divisions can be triggered in any cell type, with or without the induction of stem-cell like properties (Marhava *et al.*, 2019; Hoermayer *et al.*, 2020). This suggests that the underlying mechanism is very flexible and universal for any tissue in the plant body. To investigate this mechanism and its causal relationships, we observed the capacity to re-orient the division plane at different stages of the plant cell cycle. One possibility is that the division plane switch can happen any time after the removal of a neighbouring cell, relying on non-genomic factors only. Hence, we observed cells during the nuclear breakdown – the first step of the M-phase – and ablated cell patches at their outer adjacent side. Using *35S::MAP4-GFP*, a marker line for microtubule bundles (Marc *et al.*, 1998), we observed slightly tilted spindle orientations compared to reference cells without ablations (Fig. 1A & B). However, during the subsequent cytokinesis, the phragmoplast, which contains the new, dividing cell wall, was dragged back to a complete anticlinal orientation. Occasionally, the cell in M-phase left the cell cycle by spindle breakdown without cytokinesis, suggesting strong stress during the ablation (Fig. S1A & B). This implies that the division plane is already pre-set at this point and cannot be overwritten by the ablation of adjacent cells.

As our results suggest that the division plane is pre-set to be anticlinal at the point of division, we observed the role of the PPB, which is a presumed determining factor for the CDZ (Rasmussen, Humphries and Smith, 2011). Indeed, we found cells with narrowed microtubule arrays, an indication for the PPB, not able to respond to an ablation with the typical periclinal division (Fig. 1C & D). However, the daughter cells of these anticlinally divided cells still responded with a change in division plane to periclinal. This further supports our observation that division planes cannot be switched through ablation if the division plane is already pre-defined.

Finally, we wanted to observe the earliest point at which the division plane can still switch from anticlinal to periclinal. For this, we used a variety of cell cycle markers as we have described previously (Marhava *et al.*, 2019). Using the G2 phase marker CYCB1;1 (Ubeda-

Tomás *et al.*, 2009), we observed cells in G2 that performed a division plane switch. Notably, those cells remained in G2 much longer than usual: ~ 5 h instead of 1-2 h usually (Fig 1E & F) (Mickelson-Young *et al.*, 2016). This suggests that the division plane orientation is decided at the early stages of the G2 phase and that the establishment of a new division plane requires approx. 5 hours. Interestingly, this fits with our previous observation that there are no periclinal divisions occurring in the first 5 hours after ablation (Marhava *et al.*, 2019).

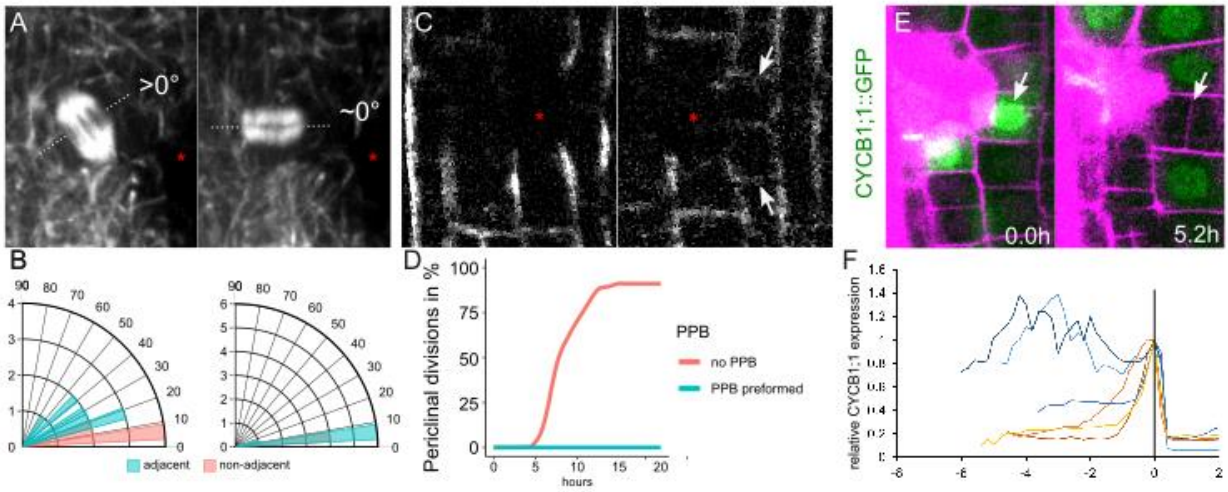


**Fig. 1 - Division plane cannot be re-positioned after PPB establishment**

**(A-B)** Division plane is fixed during M-phase. **(A)** *35S::MAP4-GFP* marked spindle at the moment of ablation (left) and phragmoplast after the ablation (right). **(B)** Quantification of the angles of spindle (left) and phragmoplast (right) after ablation (blue) and in cells non-adjacent to the ablation (red). Data are represented as histogram (bars).

**(C-D)** Division plane is fixed during PPB formation. **(C)** Time series experiment of an ablation next to cells with pre-defined PPB (as marked by *35S::MAP4-GFP* stained microtubule bundles) at the moment of ablation (left) and after the first division of the adjacent cells (right). Arrows indicate cells with a pre-defined PPB that divided anticlinally instead of periclinally. **(D)** Quantification of the rate of periclinal divisions over time in cells with pre-defined PPBs (blue) and in control cells without PPB (red). Data are represented as lines with data points every 0.2 hours.

**(E-F)** Division plane can re-orient at onset of G2. **(E)** Time series experiment of an ablation next to cells in G2 phase (as marked by *CYCB1;1::GFP* expression - green) at the moment of ablation (left) and after the first division of the adjacent cells (right). Arrows indicate cells with CYCB1;1 expression that divided periclinally. Cells were stained with propidium iodide (pink). **(F)** Quantification of the CYCB1;1 expression relative to the time point of division in wound-adjacent cells (blue) and in non-adjacent cells (orange). Notice the expression at the beginning of the time series in the blue cells. Asterisks mark ablated cells.

In conclusion, we have observed that the division plane switch cannot occur when the PPB and the underlying cortical division zone are already defined. This suggests restorative divisions cannot overwrite the normal division plane selection. Rather, it suggests that the ablation uses an altered version of the mechanism for normal division plane selection in the root.

**Restorative division orientation is defined by directional expansion**

Our results suggest restorative divisions utilize the same mechanism for division plane orientation as normal proliferative divisions. This is further supported by the fact that no genetic or pharmacological perturbation has resulted in the complete loss of division plane reorientation in our previous studies - only division speed has been affected (Marhava *et al.*, 2019; Hoermayer *et al.*, 2020). With only one exception: The inhibition of cell expansion (through hyperosmotic treatment) completely abolished periclinal divisions after ablation. Furthermore, the amount of cell expansion after ablation correlates with the speed and amount of restorative divisions. This puts cell expansion at the most promising position for understanding the upstream mechanism of division plane selection.

To study the influence of cell expansion on division plane determination, we investigated ablation sites after 24 hours in 3D. For this, we imaged z-stacks covering the whole root meristem stained with PI or FM4-64. We found a variety of different division planes around the wound, including periclinal divisions and radial divisions (Fig. 2A & C). Additionally, we found periclinal cell divisions in cells non-adjacent to the ablation (Fig. 2B). We observed previously a fraction of cells dividing periclinally without a direct contact to the removed cells. Notably, these cells lacked the expression of the wound-inducible ERF115, which stains only adjacent cells during normal regeneration (Hoermayer *et al.*, 2020). This suggests that these non-adjacent cells are not affected by the wound-responses and the induction of restorative divisions in these cells utilizes a different mechanism.

To test the influence of cell expansion on these cells, we performed long-term life imaging which allowed us to track the width of cells in close vicinity to the wound. In one of those ablation sites (Fig. 2D & E), we observed that the directly adjacent cell expanded the most, reaching ~1.5 times its thickness at the time of division (~5 hours). The non-adjacent cell expanded slower, reaching ~1.4 times the original thickness at the point of division (~8 hours),

and the neighbour expanded barely, with ~1.1 times expansion before the anticlinal division ~10 hours after ablation. We have observed this increased expansion in non-adjacent cells multiple times, however, always expanding slower than their directly adjacent cells (Fig. 2F).

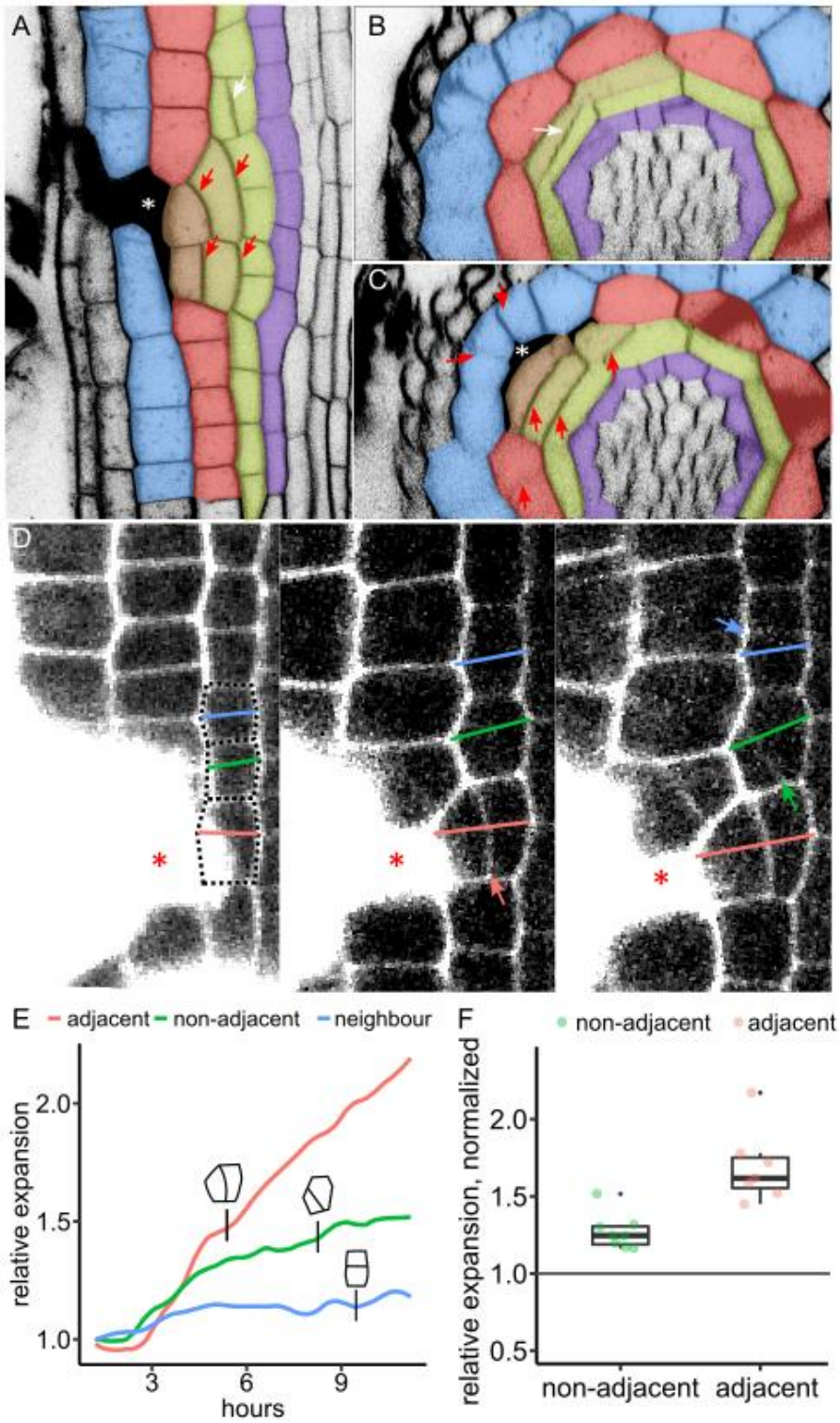


**Fig. 2 - Division orientation is defined by directional expansion**

**(A-C)** Division plane orientations 24 hours after cortex and epidermis ablation. **(A)** Front view with periclinal divisions of the inner-laying endodermis (red arrows). **(B)** Top view more distant from the ablation with periclinal divisions of non-adjacent endodermis cells (white arrows). **(C)** Top view directly adjacent to the ablation with periclinal divisions in the endodermis and radial division in cortex and epidermis (red arrows). Roots were stained with FM4-64. Cell types were re-colorized as epidermis (blue), cortex (red), endodermis (green) and pericycle (purple).
**(D-F)** Non-adjacent periclinal division are preceded by cell width expansion. **(D)** Time series of cells close to ablation. Maximum cell width is drawn as line: red for adjacent cell, green for non-adjacent cell and blue for distant neighbour. Divisions are marked by arrows. **(E)** Quantification of cell width from (D) and time point of division. Division orientation is drawn in schematic next to time of division (black line). **(F)** Quantification of cell width expansion in multiple roots in non-adjacent cells (green) and adjacent cells (red) before periclinal divisions. Expansion was normalized to closest neighbour. Notice the significant increase of width expansion compared to neighbouring cells in both groups. Asterisks mark ablated cells.

---

Here, our results show how non-adjacent cells expand towards the wound resulting in a re-orientation of the division plane. As those non-adjacent cells are not next to a wound-induced hole, we assumed that it is the whole tissue, which expands and deforms. This suggests that the cell expansion can be a passive process and this indirect stretching transforms into a cue for the division plane positioning mechanism. Again, this suggests that the mechanism utilizes the pre-existing division plane selection that usually occurs during the growth of the root meristem with its proliferative divisions.

**Tissue regeneration is pre-defined by instant, wound-induced deformations**

Our results suggest that the amount and direction of cell expansion is causal to initiating periclinal, restorative cell divisions. Previously, we have found that the vast majority of restorative divisions occur at the inner adjacent side of an ablated cell (Marhava *et al.*, 2019). Similarly, we have not observed any directional cell expansion from outer lying cells after the ablation of inner cortex or endodermis cells. However, why these outer lying cells cannot expand remains elusive, especially considering that the same cells (e.g. cortex cells) can expand after the ablation of their outer neighbour (epidermis) but not if their inner neighbour

(endodermis). This might suggest that cells cannot sense the death of their inner neighbour and activate expansion towards the wound.

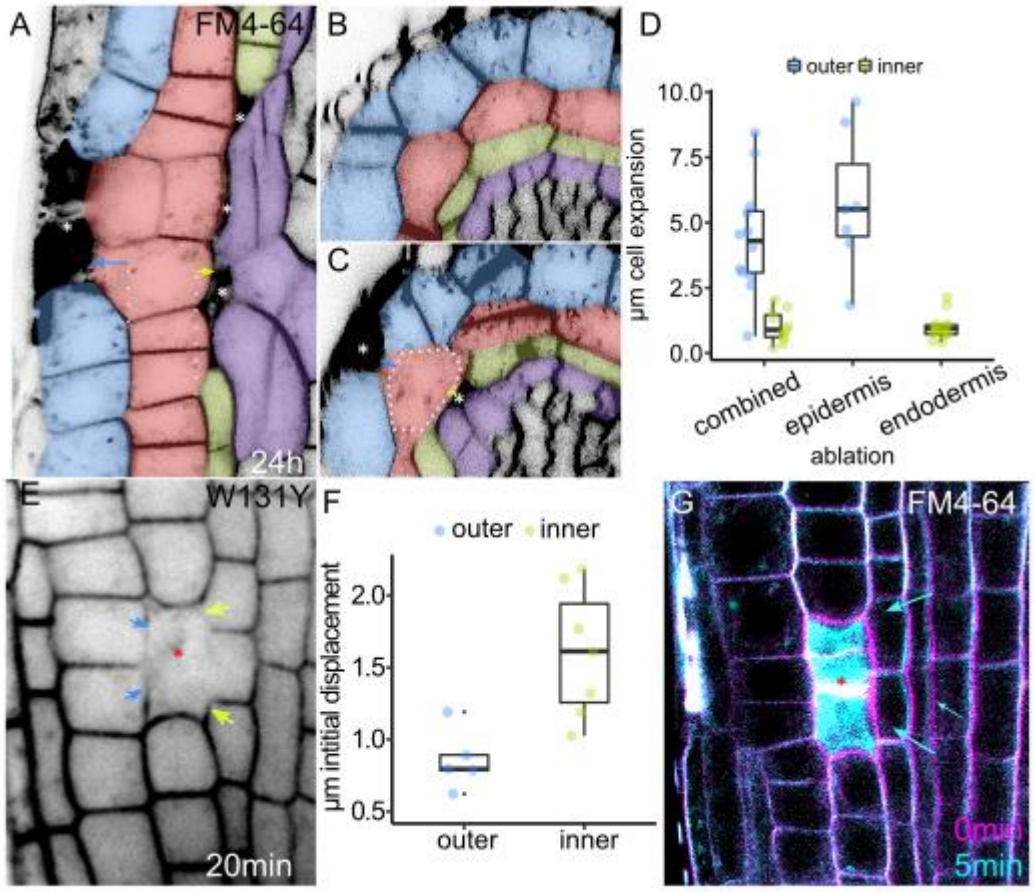


**Fig. 3 – Tissue regeneration is pre-defined by instant, wound-induced deformations**

**(A-D)** Expansion rate in cortex 24 hours after simultaneous epidermis and endodermis ablation. **(A)** Front view with expansion of cortex cells outwards - towards ablated epidermis (blue arrow) - and inwards - towards ablated endodermis cells (green arrow). **(B)** Top view more distant from the ablation without any ablation-induced expansions. **(C)** Top view directly adjacent to the ablation with expansion of cortex cells outwards - towards ablated epidermis (blue arrow) - and inwards - towards ablated endodermis cells (green arrow). Roots were stained with FM4-64. Cell types were re-colorized as epidermis (blue), cortex (red), endodermis (green) and pericycle (purple). (D) Quantification of expansion of cortex cells 24 hours after ablation towards outer side (blue) and inner side (green) in combined ablations and separate ablations of epidermis and endodermis (from left to right).

**(E-G)** Asymmetry of inner vs. outer expansion is established at moment of ablation. **(E)** *W131Y* plasma membrane marker 20 min after ablation. Image is generated from summed slices of 10 images from a spinning disk microscope (10 s total). Arrows indicate initial deformations from inner (green) and outer (blue) cells. **(F)** Quantification of initial displacement/deformation in µm within first 20min after

ablation. **(G)** Time series overlay of cortex cell death directly before death (purple) and 5 min after death (blue). Cells were stained with FM4-64. Arrows indicate displacement of membranes. Asterisks mark ablated cells.

---

To investigate this phenomenon, we studied cortex cells where we ablated cells both on the inside (endodermis) and the outside (epidermis cells). After 24 h we found that those cells only expanded towards the outer, epidermal cells, but not the inner endodermis cells (Fig 3 A-C). The expansion was similar to cells adjacent to only outer ablated epidermis or inner ablated endodermis (Fig. 3D). This suggests that the expansion towards the inner cells is inhibited somehow, likely because of geometrical hindrances.

Previously, we found a nearly instantaneous deformation of adjacent cell walls after the death of the most outer lying cells (Hoermayer *et al.*, 2020). To investigate the asymmetry of expansion from inner vs. outer cells, we ablated cortex cells and imaged the deformations in the adjacent cells after 5-20min. Notably, we found that similar to the subsequent expansion, the deformations also occurred asymmetrically, with stronger deformation in inner endodermis cells and nearly no deformation in outer epidermal cells (Fig. 3E-G). These deformations occur within a few minutes only, ruling out the possibility of developmentally driven transcriptional responses as cause for this asymmetry. Notably, when we ablated bigger areas in the root, we observed a strong fluid-like dragging-in of the inner tissues into the wound, while the outer tissue stayed mostly in place (SVideo 1). This suggests that the inner tissues are softer or under higher pressure, which leads to the asymmetric deformation directly after ablation. Furthermore, this implies that this tissue-driven asymmetry is the cause of expansion and divisions only at the inner side of ablated cells.

**Auxin inhibition of cell expansion sensitizes cells for ablation-induced stretches**

Given that the asymmetry of inner vs. outer divisions is caused by the tissue geometry and its initial deformation during the wounding, we wanted to observe perturbations, which break this asymmetry. Previously, we have shown that exogenous auxin increases the amount of outer cells dividing periclinally, partly breaking the asymmetry (Hoermayer *et al.*, 2020). Further investigation of 1 µM NAA treated roots revealed that even cells in further inner tissues, not connected to the wound, can induce periclinal cell divisions 24 hours after ablation (Fig. 4A & B). To investigate whether auxin affects the initial tissue deformation, we pre-treated roots 1 h

with auxin, performed ablations and imaged those within 5-20 min. The observed initial displacement of inner and outer cells completely mimicked the ablation in untreated roots (Fig. 4C, Fig. S2A). This suggests that auxin is not affecting the tissue integrity underlying the asymmetry of division occurrences.

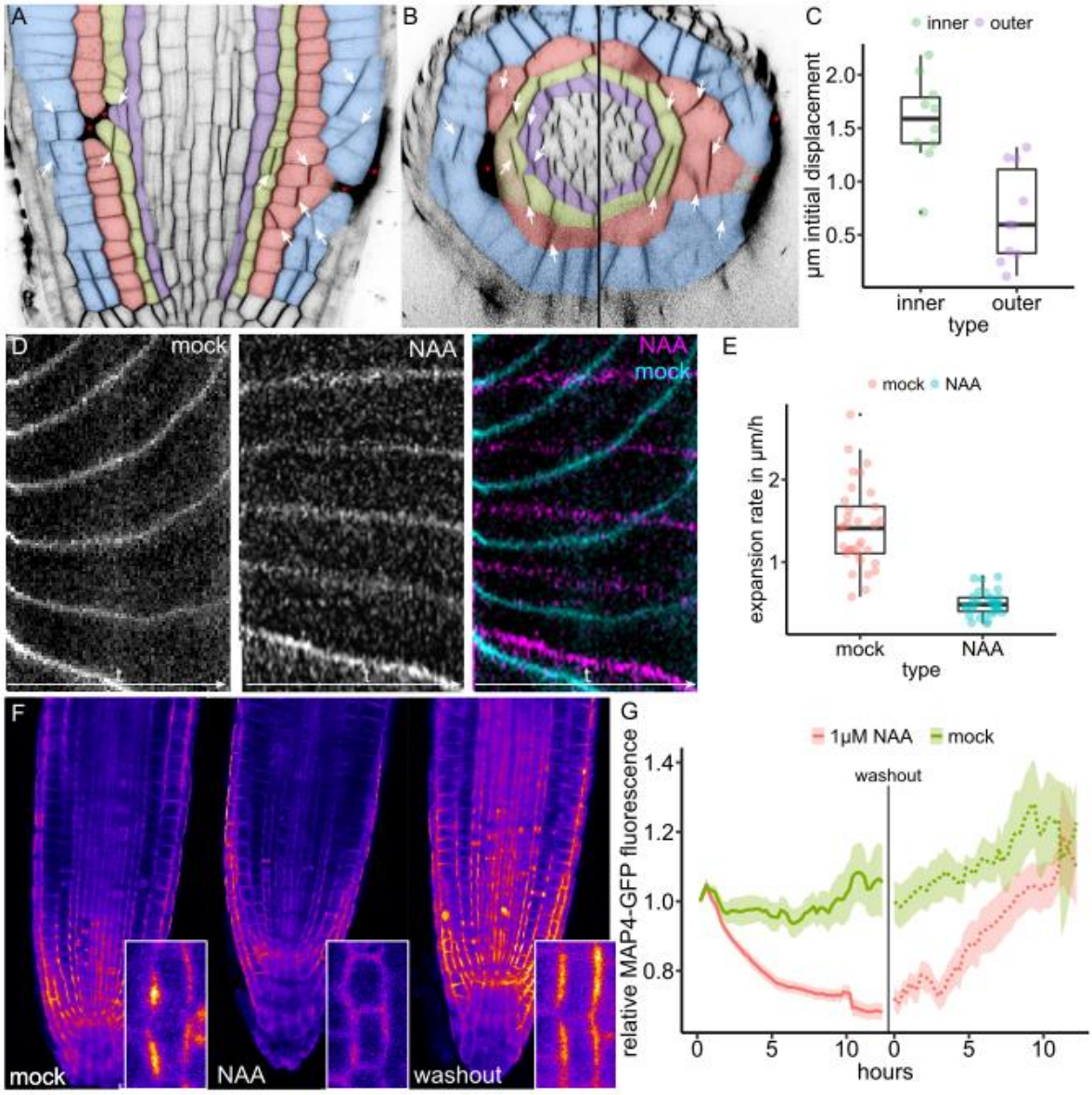


**Fig. 4 - Auxin reduces expansion and transversal MT arrays in the meristem**

**(A-C)** Divisions and expansion upon auxin treatment 24 hours after ablation. Front view **(A)** and top view **(B)** of auxin treated root 24 hours after ablation. Roots were stained with FM4-64. Cell types were re-colorized as epidermis (blue), cortex (red), endodermis (green) and pericycle (purple). **(C)** Quantification of initial displacement/deformation in µm within first 20min after ablation. Note the similar asymmetry as in untreated roots (see Fig. 3F). Asterisks mark ablated cells.

**(D-E)** Auxin inhibition on cell expansion. **(D)** Kymographs of propidium iodide stained cortex cell walls upon mock (left), 1µM NAA treatment (middle) and overlay (right). Time is displayed on the x-axis. **(E)** Quantification of expansion rates from kymographs between mock (red) and 1 µM NAA treatment (blue).
**(F-G)** Auxin inhibition on MT arrays. **(F)** 35::MAP4-GFP marked microtubule arrays after 12 hours of mock (left) and 1 µM NAA (middle) treatment, and after 12 hours NAA followed by 12 hours mock treatment ("washout", right). Insets show microtubule polarity changes in endodermis cells. **(G)** Quantification of 35S::MAP4-GFP signal over time after mock (green) and 1 µM NAA treatment (red). Dotted lines are after washout: pre-treated seedlings were transferred to a new agar block without any treatment. Lines represent mean and lighter background represents standard error.

---

Hence, we assume that auxin affects the later response of cells to increase periclinal cell divisions in outer cells. One of the most prominent effects of auxin in root tissues is the inhibition of cell expansion (Barbez *et al.*, 2017; Fendrych *et al.*, 2018). This phenomenon was heavily studied in the elongation and transition zone and it is suggested to partly require non-transcriptional responses. However, this effect was not investigated in the root meristem. Hence, we observed individual cell elongation rates in the meristem and found that also here, auxin massively inhibits cell expansion (Fig 4D & E).

The inhibition of cell expansion by auxin is accompanied by a re-orientation of cortical microtubule arrays - from transversal to longitudinal – inhibiting their role in cell wall extension (Montesinos *et al.*, 2020). To further explore the effect of auxin on cell expansion in the root meristem, we investigated microtubule behaviour after auxin treatment. During a long-term live imaging, we observed a strong downregulation of microtubule arrays by auxin (Fig. 4F & G). The typical transversal arrays either vanished or became replaced by less organized, partly longitudinal arrays. Furthermore, after a washout of auxin, we found that both general microtubule abundance and transversal arrays re-appeared during the recovery of root growth and cell elongation. Notably, in a similar experiment, roots treated with IXB 10 µM (also reducing cell elongation through cellulose synthesis inhibition (Scheible *et al.*, 2001)) showed a strong reduction of microtubule arrays (Fig S2B). Upon IXB treatment however, most of the remaining microtubule arrays became radially longitudinal, leading to radial divisions, which are usually absent from the meristem (Fig S2C). This suggests that inhibited cell

elongation/expansion after longer time leads to microtubule de-stabilization and reorientation towards longitudinal and/or disorganized arrays.

Here our results suggest that auxin effect on restorative divisions is independent of tissue deformation after wounding. Rather, auxin inhibits elongation and expansion of cells in the meristematic zone and henceforth reduces the microtubule polymerization and the amount of transversal arrays.

**Wound-induced transient re-orientation of microtubule arrays**

The strongly affected microtubule dynamics upon auxin and IXB induced elongation inhibition motivated us to investigate the microtubule dynamics within the meristem during the division plane switch. Notably, microtubule strands are strongly disorganized in the meristematic zone, likely due to the small cells and a plethora of mechanical and developmental cues affecting their stability. However, transverse arrays can be observed (Panteris *et al.*, 2013), especially by examining MAP4 decorated microtubule strands at the lateral and apical/basal walls as imaged by front view confocal microscopy.

To investigate the microtubule behaviour, we chose *35S::MAP4-GFP* marked microtubules and used vertical stage microscopy to observe their behaviour in a long term time series. We found that inner adjacent cells performing restorative, periclinal divisions underwent a series of altered microtubule stability events: i.) transversal microtubule arrays, as observed at the inner lateral membrane, were reduced (Fig. 5A); ii.) longitudinal arrays appeared and became visible at the apical and basal membranes (Fig. 5B); iii) Finally, these longitudinal arrays contracted to form longitudinally oriented PPBs (Fig. 5C) which then resulted in longitudinal, i.e. periclinal division planes. Notably, the time series experiments revealed that the loss of transversal arrays and the gain of longitudinal arrays occur at the same time and not subsequently (Fig. 5D, FigS5A). This leads to a period in which the restorative dividing cells show a mixed population of transversal and longitudinal arrays (Fig. 5E & F). The length of this period was varying and probably, the amount of longitudinal vs. transversal arrays was indicative for which PPB was forming afterwards as during the contraction of the arrays, only one regime of either transversal or longitudinal arrays was present. The changed microtubule behaviour was accompanied by cell expansion; however, MT depolymerisation by Oryzaline treatment did not affect the ability to expand to the wound (Fig. S3B). This suggests that microtubule orientation responds to changes in cell expansion, possibly with the amount of transversal vs. longitudinal arrays depending on the amplitude of expansion.

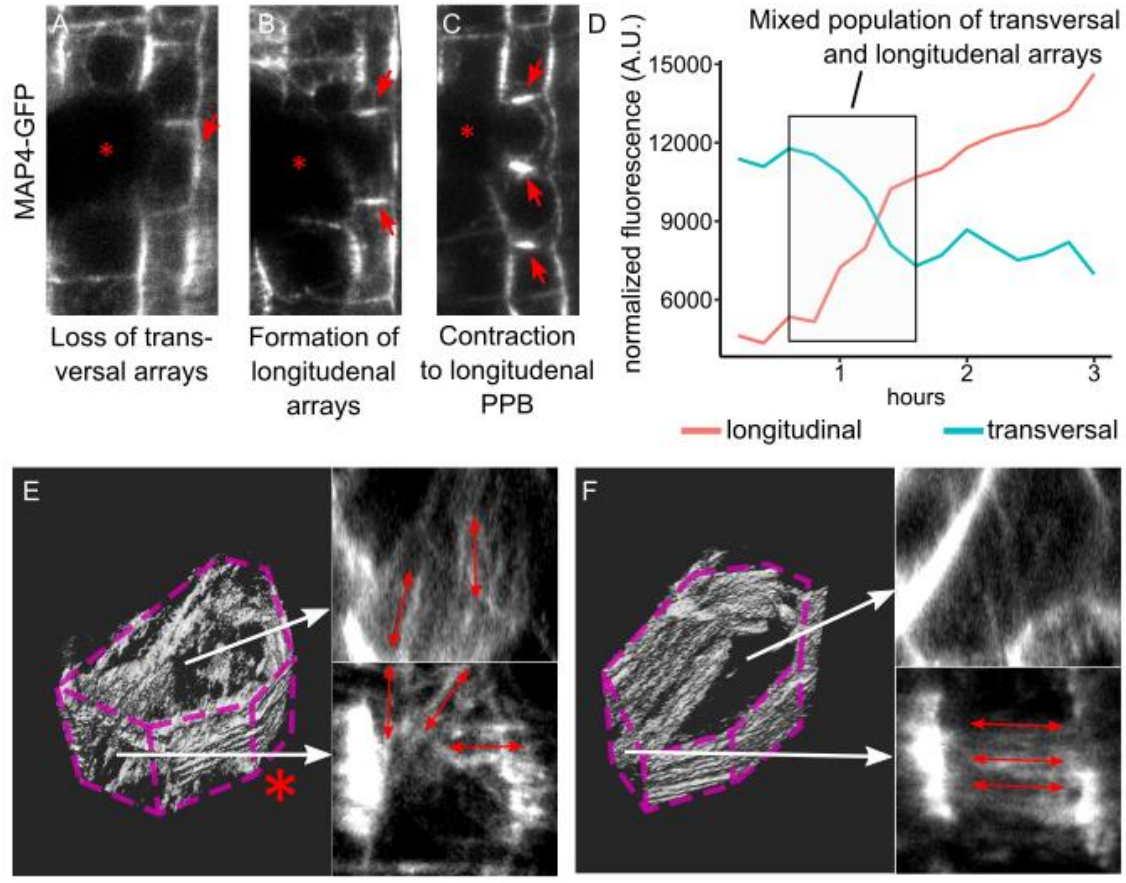


**Fig. 5 - Wound-induced transient re-orientation of microtubule arrays**

**(A-D)** Microtubule arrays changes during restorative divisions. **(A)** Endodermis cell with a reduced amount of transversal MT arrays (red arrow) compared to neighbouring cells. **(B)** Endodermis cell with increased amount of longitudinal MT arrays (red arrows) compared to neighbouring cells. **(C)** Endodermis cell with formed longitudinal PPB. Confocal images from *35S::MAP4-GFP* roots were taken 8 hours after ablation and pictures represent summed slices of 3 z-planes. **(D)** Quantification of a MAP4-GFP fluorescence at transversal and longitudinal sites within the same endodermis cell over time. Boxed area shows time frame of overlapping increase of longitudinal and decrease of transversal arrays.

**(E-F)** 3D reconstruction of MT arrays after ablation. **(E)** Imaris-generated image of a cortex cell next to ablation (red asterisk) with mixed population of transversal (bottom inset) and longitudinal (top inset) MT arrays (red arrows). **(F)** Imaris-generated image of a non-adjacent control cortex cell from the same root, with transversal (bottom inset) but no longitudinal (top inset) MT arrays (red arrows).

**Microtubule array formation is driven by cell stretching**

Our results suggest an interdependency of cell expansion and microtubule dynamics. Now the question arises, how is directional expansion transformed into altered microtubule orientation? We have already seen that auxin and IXB inhibition of cell expansion leads to a loss of MT bundles and a re-orientation towards radially longitudinal arrays. It has been proposed that MTs follow the direction of maximal tensile stress and tensile stress is perpendicular to cell expansion direction (Louveaux *et al.*, 2016; Hamant *et al.*, 2019). Hence, loss of tensile stress upon expansion inhibition and change of expansion direction might directly influence MT stability and orientation.

To investigate this, we observed microtubule dynamics around wounds in the very moment of cell ablation. We pre-treated roots 12 hours with auxin to reduce the amount of transversal MT arrays. During the application of the UV laser, we observed a complete loss of microtubule bundles and the above-described dragging-in of the inner tissues (Fig S4A). Shortly afterwards, the MT arrays re-appeared in a slightly dis-organized way. We wanted to observe the re-organization of MT bundles further, so we performed laser ablations with weaker pulses to harm the cell and induce the complete MT depolymerisation, but to retard the collapse of the harmed cell (Fig. 6A). After a short time frame of 5-20 min the harmed cell collapsed leading to deformations in the neighbouring cells. Notably, MT bundles did not re-appear until the very moment of neighbouring cell collapse and subsequent deformation of the observed cell (Fig. 6B, Fig. S4B). This suggests that the MT are involved in the perception of cell stretch and MT bundles are initialised or stabilised upon cell stretching.

To further test this hypothesis, we used the micropipette system used in animal research to investigate membrane cortical tension (Maître *et al.*, 2012) and modified it to induce stretches on cells in living root tissue. For this, we pre-treated 5 d old *MAP4-GFP* seedlings with 1% Macerozyme and 0.2 M Mannitol for 20 min to decrease cell wall stiffness and turgor pressure, hence softening the tissue. After a 2 hours recovery, we transferred single seedlings to liquid medium containing 0.2 M Mannitol and mounted them on a confocal microscope with a micromanipulator. Using micropipettes of 20 µm diameter, we applied forces of -750 Pa on the outer surface of the root and managed to suck up and stretch single epidermis cells for up to 1 hour. Microtubules were mostly depolymerized after mannitol treatment, but when we applied the stretching force small patches of increased GFP signal, presumably resembling

polymerisation events appeared (Fig. 6C). This signal increase occurred nearly instantaneous and was highly reversible: after release of the stretching force, the signal decreased to the background level within seconds (Fig. 6D). Over longer time, the MT signal continued to increase to ~2.5 times the pre-stretch levels, and around ~30 min single bundles became apparent (Fig. 6E-G). To test whether these accumulations are a general effect of the aspiration on the cytosol, we observed the same effect in *35S::GFP* (free cytosolic GFP) and in Oryzalin treated seedlings (Fig. S4C-E). Both experiments have not showed any accumulation of GFP after aspiration, indicating that the observed effect is specific to the formation of MT bundles. These results resemble the previous observation of increased MT bundle formation upon cell stretching and suggest that MT stability is dependent on cell expansion mediated cell stretching. Furthermore, our results imply that changes of directional cell expansion, as observed after ablation, alter MT stability and might be transformed into MT array orientation.

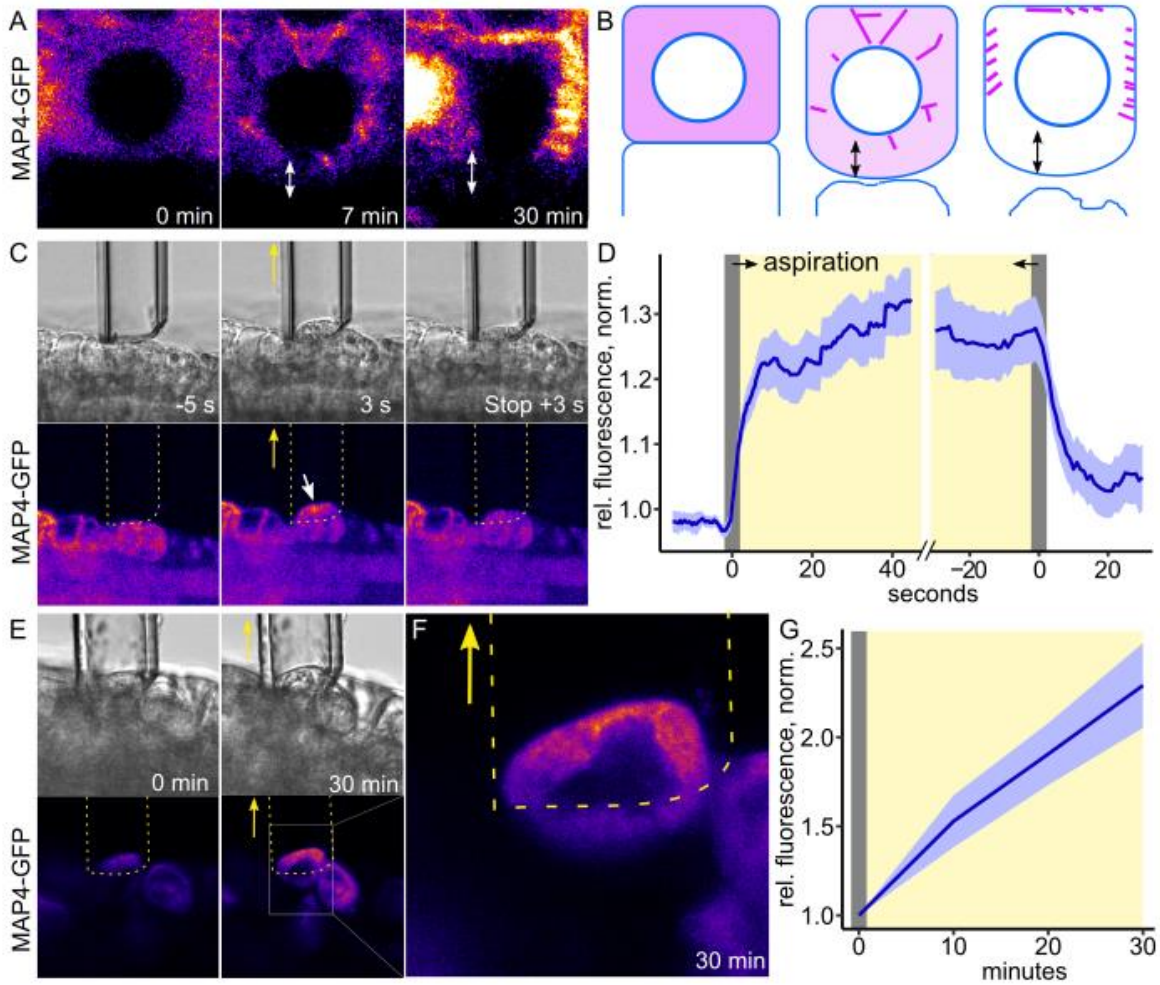

**Fig. 6 – Stretching induced microtubule array formation**

**(A-B)** Microtubule re-polymerisation during neighbour cell collapse. **(A)** *35S::MAP4-GFP* fluorescence of a cortex cell adjacent to UV-laser harmed neighbour (white asterisk) after 12 hour 1 µM NAA pre-treatment. Microtubule signal before (left), during (middle) and after collapse of neighbour (right). **(B)** Schematic representation of observed MT arrays (purple lines) from (A).

**(C-G)** Micropipette mediated aspiration causes increase in MT marker signal. **(C)** Short-term aspiration of epidermis cells from meristems after 20 min cell wall digestion with 1% Macerozyme and 0.2 M Mannitol and 2 hour recovery on 0.2 M Mannitol. Top row: brightfield; bottom row: *35S::MAP4-GFP* fluorescence before (left) during (middle) and after (right) aspiration. Aspirated cell is marked by white arrow. **(D)** Quantification of *35S::MAP4-GFP* signal from aspirated epidermis cells. Fluorescence values are relative to imaging start, smoothed over 5 time points (0.4 s each) and normalized to closest non-aspirated neighbour. Data are represented as mean from individual cells and lighter background indicates standard error. Yellow background represents time frame of aspiration. **(E)** Long-term aspiration of epidermis cells. Top row: brightfield; bottom row: *35S::MAP4-GFP* fluorescence at start of aspiration (left) and during aspiration (right). **(F)** Higher magnification of aspirated cell from 6E. **(G)** Quantification of *35S::MAP4-GFP* signal from aspirated epidermis cells. Fluorescence values are relative to imaging start and normalized to closest non-aspirated neighbour. Data are represented as mean from individual cells and lighter background indicates standard error. Yellow background represents time frame of aspiration. Yellow arrows mark direction of aspiration.

---

## Discussion

In this work, we addressed the question how root cells can change their division planes towards the direction of ablated cells in their vicinity. We found that the direction of growth, independent of the vicinity to the wound is transmitted to microtubule bundle stability and drives the selection of the division plane directly after ablation. While the underlying mechanism between this connection of directional cell expansion and MT arrays orientation remains elusive, our data revealed some behaviours that will help elucidating this mechanism. In summary, our data shows that (i) MT bundle stability is dependent on the expansion rate, (ii) less expanding cells are orienting MT arrays radially, (iii) MT arrays reorient transiently with mixed population of different orientations and (iv) MT bundle formation is induced upon fast cell stretching.

Restorative divisions require at least 5 hours to switch division plane from anticlinal to periclinal and they are not able to switch division plane once it is set by formation of the PPB. This suggested us that restorative divisions go through the normal process of cell cycle

regulation and division-plane selection acting on all root cells. Furthermore, any cell, being adjacent or non-adjacent can change division plane if it expands towards a changed direction. This probably distinguishes the basic capacity of restorative divisions from developmentally regulated division plane switches like during stomatal development or lateral root formation.

Microtubule orientation and cell expansion direction are tightly linked as the microtubules serve as guiding strings for the deposition of new cell wall material (Kropf, Bisgrove and Hable, 1998). Cellulose synthase complex is travelling along the microtubule filaments to deposit cellulose fibrils in the orientation of cortical MTs (Paredez, Somerville and Ehrhardt, 2006). Consequently, the cell wall extends easiest at the position of the MT arrays. Turgor pressure is equally distributed in the whole cell, hence mediates the anisotropic cell expansion at the point of easiest extension. As MTs orient perpendicular to the growth axis, this creates a feedback loop that leads to the anisotropic growth of plant cells. However, what drives MTs to align perpendicular to the growth axis remains unknown.

MTs itself have been proposed as tensile stress sensors (Louveaux *et al.*, 2016; Hamant *et al.*, 2019). In vivo experiments have suggested that microtubule stability can be increased during tensile stress, i.e. stretching. We have provided similar observations here in this study. Additionally, the well-defined tension field in the shoot allowed prediction of MT orientation very precisely. Perturbations of this tissue tension by laser ablation led to a reorientation of MT arrays. In the case of shoot apical meristem that meant circumferential of the ablation site from the neighbouring cells of the same cell file. This is similar to our observation, where MTs orient circumferentially from the inner side around the wound.

In conclusion, our results show how division plane selection in the root depends on directional cell expansion, mediated by tissue stretching and microtubule orientations. The underlying molecular mechanism remains elusive, but results suggesting MTs as tension sensor indicate that there are no extra components needed for the observed phenotypes. However further analysis of cell wall receptors, microtubule associated proteins and cell division plane selective proteins might give additional hints about whether or not additional mechanisms are needed.

**References**

Abrash, E. B. and Bergmann, D. C. (2009) ‘Asymmetric Cell Divisions: A View from Plant Development’, *Developmental Cell*. Cell Press, 16(6), pp. 783–796. doi:

10.1016/J.DEVCEL.2009.05.014.

Barbez, E. *et al.* (2017) 'Auxin steers root cell expansion via apoplastic pH regulation in Arabidopsis thaliana', *Proceedings of the National Academy of Sciences of the United States of America*. National Academy of Sciences, 114(24), pp. E4884–E4893. doi: 10.1073/pnas.1613499114.

van den Berg, C. *et al.* (1995) 'Cell fate in the Arabidopsis root meristem determined by directional signalling', *Nature*. Nature Publishing Group, 378(6552), pp. 62–65. doi: 10.1038/378062a0.

Besson, S. and Dumais, J. (2011) 'Universal rule for the symmetric division of plant cells', 108(15). doi: 10.1073/pnas.1011866108/-/DCSupplemental.

Bloch, R. (1941) 'Wound Healing in Higher plants', *Botanical Review*, 7(2), pp. 110–146. Available at: https://www.jstor.org/stable/pdf/4353245.pdf?casa_token=hez8JLlZDa0AAAAA:fxsg5P0Hwze29UWw_tdgJ1PVuUY_xNvq9kk-0EfEQY7_E3hODqpD5jC53Y8p_xNx26LcrS6cTzwTwpMFfVWouWp2YLon2PdBqw4_lxV6oCRtXK4XIxUw5g (Accessed: 15 June 2019).

Canher, B. *et al.* (2020) 'Rocks in the auxin stream: Wound-induced auxin accumulation and ERF115 expression synergistically drive stem cell regeneration', *Proceedings of the National Academy of Sciences*. National Academy of Sciences, 117(28), pp. 16667–16677. doi: 10.1073/PNAS.2006620117.

Damme, D. Van, Vanstraelen, M. and Geelen, D. (2007) 'Cortical division zone establishment in plant cells', *Trends in Plant Science*. Elsevier, 12(10), pp. 458–464. doi: 10.1016/J.TPLANTS.2007.08.011.

Dolan, L. *et al.* (1993) 'Cellular organisation of the Arabidopsis thaliana root', *Development*, 119(1), pp. 71–84.

Fendrych, M. *et al.* (2018) 'Rapid and reversible root growth inhibition by TIR1 auxin signalling', *Nature Plants*. Palgrave Macmillan Ltd., 4(7), pp. 453–459. doi: 10.1038/s41477-018-0190-1.

Hamant, O. *et al.* (2008) 'Developmental patterning by mechanical signals in Arabidopsis', *Science*. American Association for the Advancement of Science, 322(5908), pp. 1650–1655.

doi: 10.1126/science.1165594.

Hamant, O. *et al.* (2019) 'Are microtubules tension sensors?', *Nature Communications 2019 10:1*. Nature Publishing Group, 10(1), pp. 1–12. doi: 10.1038/s41467-019-10207-y.

Heyman, J. *et al.* (2013) 'ERF115 Controls Root Quiescent Center Cell Division and Stem Cell Replenishment', *Science*. American Association for the Advancement of Science, 342(6160), pp. 860–863. doi: 10.1126/SCIENCE.1240667.

Heyman, J. *et al.* (2016) 'The heterodimeric transcription factor complex ERF115–PAT1 grants regeneration competence', *Nature Plants*, 2(11), p. 16165. doi: 10.1038/nplants.2016.165.

Hoermayer, L. *et al.* (2020) 'Wounding-induced changes in cellular pressure and localized auxin signalling spatially coordinate restorative divisions in roots', *Proceedings of the National Academy of Sciences*. National Academy of Sciences, 117(26), pp. 15322–15331. doi: 10.1073/PNAS.2003346117.

Hoermayer, L. and Friml, J. (2019) 'Targeted cell ablation-based insights into wound healing and restorative patterning', *Current Opinion in Plant Biology*. Elsevier Ltd, pp. 124–130. doi: 10.1016/j.pbi.2019.08.006.

Ikeuchi, M. *et al.* (2019) 'Molecular Mechanisms of Plant Regeneration', *Annual Review of Plant Biology*. Annual Reviews, 70(1), pp. 377–406. doi: 10.1146/annurev-arplant-050718-100434.

Koizumi, K., Hayashi, T. and Gallagher, K. L. (2012) 'SCARECROW reinforces SHORT-ROOT signaling and inhibits periclinal cell divisions in the ground tissue by maintaining SHR at high levels in the endodermis', *Plant Signaling & Behavior*. Taylor & Francis, 7(12), p. 1573. doi: 10.4161/PSB.22437.

Kropf, D. L., Bisgrove, S. R. and Hable, W. E. (1998) 'Cytoskeletal control of polar growth in plant cells', *Current Opinion in Cell Biology*. Elsevier Current Trends, 10(1), pp. 117–122. doi: 10.1016/S0955-0674(98)80094-X.

Louveaux, M. *et al.* (2016) 'Cell division plane orientation based on tensile stress in Arabidopsis thaliana', *Proceedings of the National Academy of Sciences*. National Academy

of Sciences, 113(30), pp. E4294–E4303. doi: 10.1073/PNAS.1600677113.

Louveaux, M. and Hamant, O. (2013) 'The mechanics behind cell division', *Current Opinion in Plant Biology*. Elsevier Current Trends, 16(6), pp. 774–779. doi: 10.1016/J.PBI.2013.10.011.

Maître, J. L. *et al.* (2012) 'Adhesion functions in cell sorting by mechanically coupling the cortices of adhering cells', *Science*. Science, 338(6104), pp. 253–256. doi: 10.1126/science.1225399.

Marc, J. *et al.* (1998) 'A GFP-MAP4 reporter gene for visualizing cortical microtubule rearrangements in living epidermal cells', *Plant Cell*. American Society of Plant Biologists, 10(11), pp. 1927–1939. doi: 10.1105/tpc.10.11.1927.

Marhava, P. *et al.* (2019) 'Re-activation of Stem Cell Pathways for Pattern Restoration in Plant Wound Healing', *Cell*. Cell Press, 177(4), pp. 957-969.e13. doi: 10.1016/j.cell.2019.04.015.

Mickelson-Young, L. *et al.* (2016) 'A flow cytometric method for estimating S-phase duration in plants', *Journal of Experimental Botany*. Oxford University Press, 67(21), p. 6077. doi: 10.1093/JXB/ERW367.

Montesinos, J. C. *et al.* (2020) 'Phytohormone cytokinin guides microtubule dynamics during cell progression from proliferative to differentiated stage', *The EMBO Journal*, 39(17). doi: 10.15252/embj.2019104238.

Panteris, E. *et al.* (2013) 'Differential responsiveness of cortical microtubule orientation to suppression of cell expansion among the developmental zones of Arabidopsis thaliana root apex', *PLoS ONE*, 8(12). doi: 10.1371/JOURNAL.PONE.0082442.

Paredez, A. R., Somerville, C. R. and Ehrhardt, D. W. (2006) 'Visualization of Cellulose Synthase Demonstrates Functional Association with Microtubules', *Science*. American Association for the Advancement of Science, 312(5779), pp. 1491–1495. doi: 10.1126/SCIENCE.1126551.

Rasmussen, C. G. and Bellinger, M. (2018) 'An overview of plant division-plane orientation', *New Phytologist*. New Phytol, 219(2), pp. 505–512. doi: 10.1111/nph.15183.

Rasmussen, C. G., Humphries, J. A. and Smith, L. G. (2011) 'Determination of Symmetric and Asymmetric Division Planes in Plant Cells', *http://dx.doi.org/10.1146/annurev-arplant-*

*042110-103802*. Annual Reviews , 62, pp. 387–409. doi: 10.1146/ANNUREV-ARPLANT-042110-103802.

De Rybel, B. *et al.* (2013) 'A bHLH Complex Controls Embryonic Vascular Tissue Establishment and Indeterminate Growth in Arabidopsis', *Developmental Cell*. Cell Press, 24(4), pp. 426–437. doi: 10.1016/J.DEVCEL.2012.12.013.

Rybel, B. De *et al.* (2014) 'Integration of growth and patterning during vascular tissue formation in Arabidopsis', *Science*. American Association for the Advancement of Science, 345(6197). doi: 10.1126/SCIENCE.1255215.

Schaefer, E. *et al.* (2017) 'The preprophase band of microtubules controls the robustness of division orientation in plants', *Science*. American Association for the Advancement of Science, 356(6334), pp. 186–189. doi: 10.1126/SCIENCE.AAL3016.

Scheible, W.-R. *et al.* (2001) 'Modifications of cellulose synthase confer resistance to isoxaben and thiazolidinone herbicides in Arabidopsis Ixr1 mutants', *Proceedings of the National Academy of Sciences*. National Academy of Sciences, 98(18), pp. 10079–10084. doi: 10.1073/PNAS.191361598.

Shao, W. and Dong, J. (2016) 'Polarity in plant asymmetric cell division: Division orientation and cell fate differentiation', *Developmental Biology*. Academic Press, 419(1), pp. 121–131. doi: 10.1016/J.YDBIO.2016.07.020.

Ubeda-Tomás, S. *et al.* (2009) 'Gibberellin Signaling in the Endodermis Controls Arabidopsis Root Meristem Size', *Current Biology*. Cell Press, 19(14), pp. 1194–1199. doi: 10.1016/J.CUB.2009.06.023.

Yoshida, S. *et al.* (2014) 'Genetic Control of Plant Development by Overriding a Geometric Division Rule', *Developmental Cell*. Cell Press, 29(1), pp. 75–87. doi: 10.1016/J.DEVCEL.2014.02.002.

Zhou, W. *et al.* (2019) 'A Jasmonate Signaling Network Activates Root Stem Cells and Promotes Regeneration', *Cell*. Cell Press, 177(4), pp. 942-956.e14. doi: 10.1016/J.CELL.2019.03.006.

## Supplementary Information

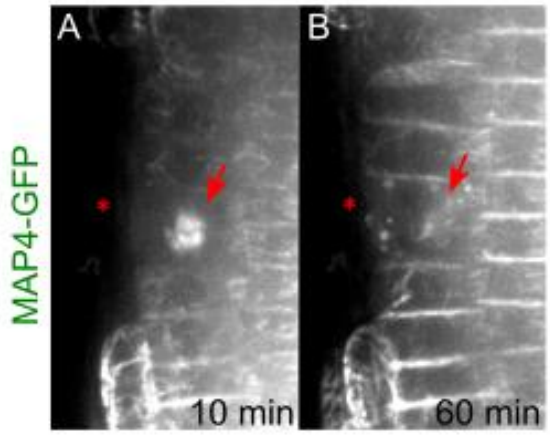


**Fig. S1 – Laser ablation induced abortion of mitosis**

**(A)** 35S::MAP4-GFP marked spindle 10min after ablation. Spindle progress is stalled at this point (red arrow). **(B)** Subsequent exit of mitosis without division as marked by breakdown of spindle (red arrow), marked by 35S::MAP4-GFP. Asterisks mark ablated cells.

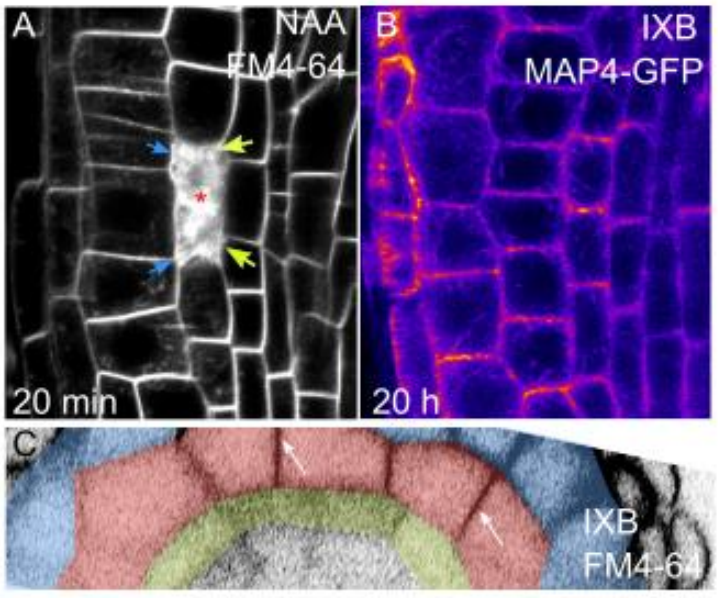


**Fig. S2 – Effects of inhibited cell expansion on MT arrays and divisions**

**(A)** FM4-64 stained ablation of cortex cell (red asterisk) 20 min after ablation upon 1 hour pre-treatment with 1µM NAA. Arrows indicate initial deformations from inner (green) and outer (blue) cells. **(B)** 35::MAP4-GFP marked microtubule arrays after 20 hours of 10 µM IXB treatment. Notice the absence of transversal arrays. **(C)** Top view of 10 µM IXB treated root 20 hours after ablation. Roots were

stained with FM4-64. Cell types were re-colorized as epidermis (blue), cortex (red), endodermis (green) and pericycle (purple). Arrows indicate radial divisions in cortex.

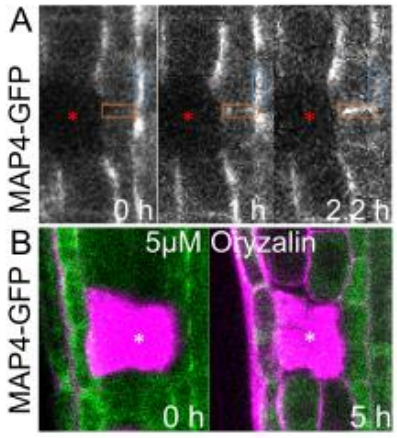


**Fig. S3 – Microtubules during restorative divisions**

**(A)** Times series of 35S::MAP4-GFP decorated MT arrays during restorative division (for quantification see Fig. 5D). Rectangles show measured area of transversal (blue) arrays and longitudinal (orange) arrays. **(B)** Time series of 35S::MAP4-GFP signal (green) upon 5µM Oryzalin treatment. Notice the predominately cytosolic localisation. Cell walls were stained with propidium iodide (pink). Asterisks mark ablated cells.

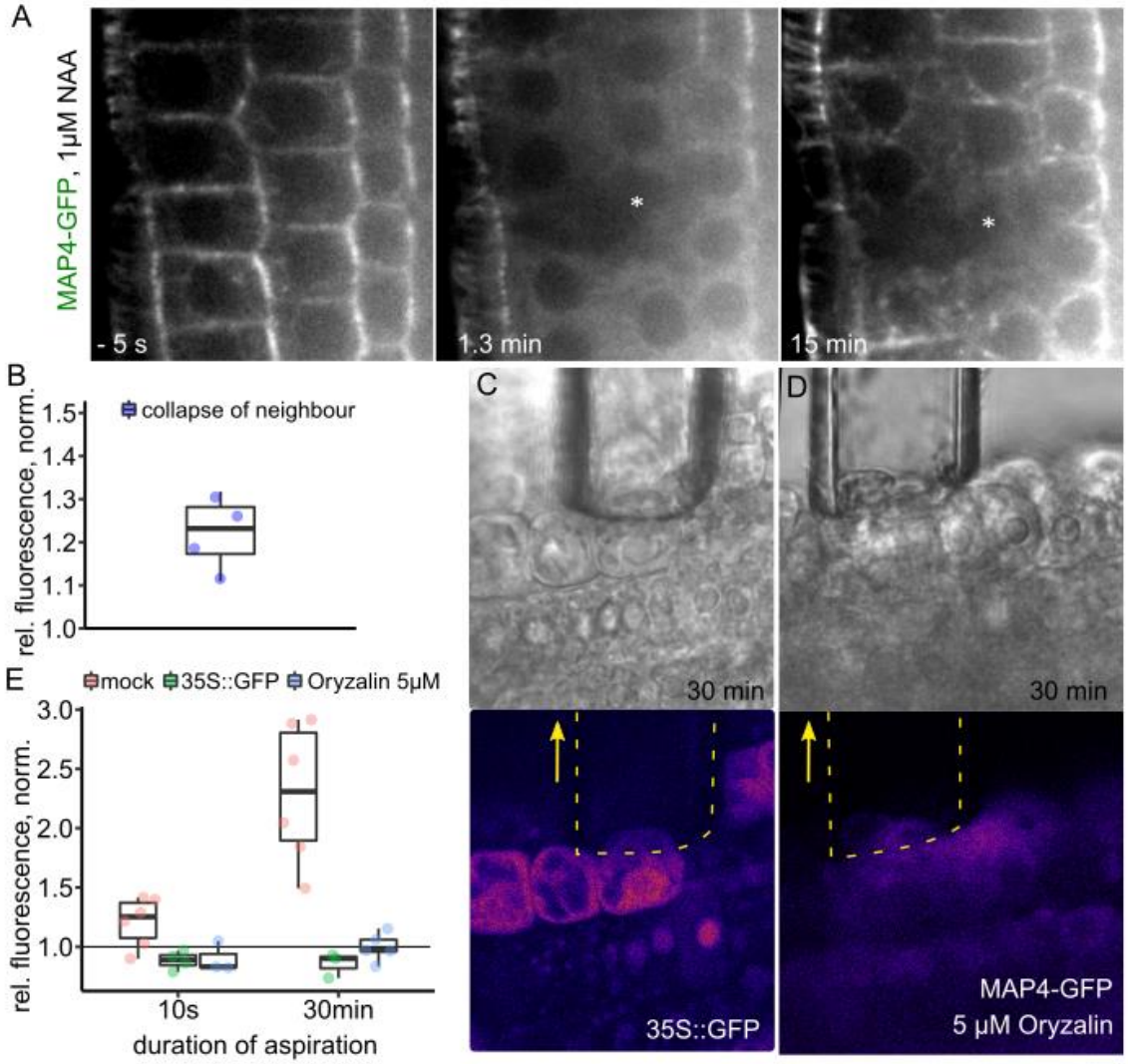


**Fig. S4 – Dynamics of microtubules and free GFP during stretching experiments**

**(A)** Times series of 35S::MAP4-GFP decorated MT arrays during UV laser ablation upon pre-treatment with 1 µM NAA for 12 hours. Loss of MT arrays happens immediately after laser application (middle) and re-polymerisation happens after collapse of ablated cell (right). **(B)** 35S::MAP4-GFP fluorescence in wound-adjacent cells within first time point after collapse of neighbour, relative to imaging start, normalized to non-adjacent neighbouring cell. Values above 1 represent increased MT polymerisation. **(C)** Long-term aspiration of epidermis cells. Top row: brightfield; bottom row: 35S::GFP fluorescence during aspiration for 30min. **(D)** Long-term aspiration of epidermis cells. Top row: brightfield; bottom row: 35S::MAP4-GFP fluorescence upon 5 µM Oryzalin treatment during aspiration for 30min. Yellow arrows mark direction of aspiration. Yellow dotted lines indicate position of micropipette. **(G)** Quantification of GFP signal from aspirated epidermis cells from mock 35S::MAP4-GFP (red), mock 35S::GFP (green) 5 µM Oryzalin 35S::MAP4-GFP (blue) treatments. Fluorescence values are relative

to imaging start and normalized to closest non-aspirated neighbour. Data are represented as mean from individual cells.

## METHODS

### Plant material

*Arabidopsis thaliana* (L.) Heynh (accession Columbia-0) was used in this work (WT). The following transgenic *Arabidopsis thaliana* lines were described previously:
*35S::MAP4-GFP* (Marc et al. 1998), CYCB1;1::GFP (Ubeda-Tomás et al. 2009).

#### Growth conditions

Seeds of *A. thaliana* were sown on Murashige and Skoog (1/2MS) medium (Duchefa) with 1% sucrose and 1% agar, stratified for 1-2 d and grown for 3-5 d at 21°C in a 16 h light/8 h dark cycle.

### Pharmacological treatments

Seedlings were transferred on solid MS medium containing the indicated chemicals: propidium iodide (PI, 10 μM, Sigma-Aldrich or Thermofisher), Naphthylacetic acid (NAA, Duchefa Biochemie, final concentration as indicated - if nothing indicated: 1 μM), Mannitol (Sigma-Aldrich, final concentration 0.2 M), Isoxaben (Sigma Aldrich, final concentration 10 μM), Latrunculin B (LatB, Sigma-Aldrich, final concentration 2 μM), Oryzaline (Duchefa Biochemie, final concentration 5 μM), Macerozyme R-10 (Serva, final concentration 1% w/v).

### Sample preparation

Seedlings were placed on chambered cover glass (VWR, Kammerdeckgläser, Lab-Tek™, Nunc™ - eine kammer, catalog number: 734-2056) as described (Marhavý and Benková 2015). With the chamber, a block of solid MS media was cut out and propidium iodide solution was added. After the liquid soaked in, 10-15 seedlings were transferred to the agar and the block was inserted into the chamber.

## Confocal imaging and image processing

Confocal imaging was performed with Zeiss LSM700/800 inverted microscopes using 20x or 40x objectives. Detection of fluorescence signals was carried out for GFP (excitation 488 nm, emission 507 nm), YFP (excitation 514 nm, emission 527 nm) and PI or FM4-64 (excitation 536 nm, emission 617 nm). For fixed time point measurements, samples were observed 12 hours after ablation or at indicated time points. Images were analyzed using the ImageJ (NIH; http://rsb.info.nih.gov/ij) and Zeiss Zen 2.3 "Black" or "Blue" software. Where necessary, images were processed by adjusting contrast and lightness. Where indicated, images where processed by sum slice operation to summarize multiple confocal planes or time points into one image. For 3D images, confocal (z) planes where chosen to fit ½ airy unit. To obtain top view images, z-stacks were processed using the "Reslice" tool.

## Spinning disk imaging

For the observation of immediate effects during/after ablation, an Andor spinning disk microscopy (CSU X-1, camera iXon 897 [back-thinned EMCCD], FRAPPA unit and motorized piezo stage) 63× water immersion objective was used. Videos were acquired with 1 focal plane, every 0.2 or 1.0 seconds. All images in a single experiment were captured with the same settings.

## Vertical stage microscopy, root tracking and image processing

Vertical stage microscopy for long-term tracking of root meristems was performed as described (Glanc, Fendrych, and Friml 2018; Marhava et al. 2019; von Wangenheim et al. 2017). Roots were imaged with a vertically positioned LSM700 or LSM800 inverted confocal microscope and Zeiss Zen 2.3 "Black" or "Blue" software, respectively, with 20x objective and detection of PI, GFP (see above) and transmitted light. Z-stacks of 30-42 µm were set accordingly to image each cell at least once. For the root-tracking, the TipTracker MATLAB script (Zen Black) or the TipTracker internal macro (Zen Blue) were used; interval duration was set between 600 s (10 min) and 720 s (12 min). The resulting images were concatenated and analysed using ImageJ. For registration, ImageJ macros "correct 3D drift", "StackReg" or "MultiStackReg" were used. Kymographs were generated using the "Reslice" tool.

**UV laser ablation setup**

The UV laser ablation was performed as described in ref. (Marhava et al. 2019; Marhavý et al. 2016) which are based on the layout published in ref. (Colombelli, Grill, and Stelzer 2004). The laser was applied in the upper corner of the cell of interest.

**Aspiration assay**

The aspiration setup was designed as previously described (Maître et al. 2012). 20 μm glass pipettes (BioMedical Instruments) with 30° bent angle were filled with distilled water and then connected to a Microfluidic Flow Control System (Fluigent, Fluiwell), with negative pressure ranging from 7-750 Pa. The microfluidic setup was mounted on a micromanipulator (Eppendorf, Transferman NK2) and micropipette movement and pressure were controlled via a custom-programmed Labview (National Instruments) interface.

5-d old seedlings were transferred onto 1% Macerozyme and 0.2 M Mannitol containing agar medium. After 20 min the seedlings were transferred very carefully to a 0.2 M Mannitol containing agar medium to recover from the cell wall digestion. Finally, the seedlings were transferred to liquid medium containing 0.2 M Mannitol in a MatTek 50mm Glass Bottom Dish, so that the cotyledons touched the glass and the root was facing towards the center of the coverslip.

For the aspiration, the micropipette was placed touching a single epidermis cell in the center of the root meristem and during imaging, full negative pressure (-750 Pa) was applied. After a few minutes, the aspiration force was removed and the imaging was stopped after that. Imaging was performed using a Leica SP5 confocal microscope with a resonant scanner and a Leica 20X, 0.7 NA objective, (Argon laser: 488 nm) for simultaneous imaging of fluorescent and brightfield channels. Higher resolution image (Fig. 6F) was taken with a 40x water objective.

**3D visualization**

3D images were obtained and analyzed using Imaris software. For Fig. 5E,F, fluorescent signal was displayed as volume display option “volume shading”.

**Quantification and statistical significance**

Asterisks illustrate the p-value: $p < 0.001$ is ***, $p < 0.01$ is ** and $p < 0.05$ is *

**Spindle and phragmoplast angles**

Spindle/phragmoplast angle was determined using the ImageJ "Angle" tool, taking the anticlinal walls as reference (0°). Data was plotted as histogram on a polar coordination system using R.

**Periclinal divisions**

Division events were counted by marking the time point at which a new cell wall (stained by propidium iodide) appeared in the first, inner adjacent cell of the ablation site. Only periclinal divisions (vertical cell walls) were counted. The percentage of cumulative division events over time was plotted using R.

**Fluorescence intensity within time series**

Signal intensity of each observed cell from multi-stack (3D) videos in the green channel was quantified using ImageJ and recorded for each available time frame. To obtain relative values, the raw data was divided by the first time point value. Similarly, data from reference cells (neighbouring, non-adjacent cells) was recorded and the ratio of sample to reference value was calculated to obtain normalized values.

**Cell expansion**

Cell expansion within time series was approximated by the cell width, which was quantified as the distance between the midpoint of the inner and outer cell wall using ImageJ. Expansion values are relative to first time point and if indicated, normalized to neighbouring (reference) cells.

During fixed time points, cell expansion or initial displacement was approximated as the horizontal distance between the wound-adjacent membrane and the first, non-adjacent membrane of a neighbouring cell (see dotted lines in Fig. 3A).

Expansion rates were determined from kymographs of growing root tips. One patch of cortex cells was registered over time, turned into a kymograph, coordinates of each line were obtained using Kymobutler, and the rate of expansion was calculated from the slope of the lines.

**Microtubule intensity within time series**

Microtubule intensity (35S::MAP4-GFP) in growing root tips was measured in selections from one confocal plane over time, obtained from the "Threshold" tool in ImageJ. Every time frame was evaluated separately with a new selection. To obtain relative values, the raw data was divided by the first time point value.

Microtubule array intensity of a single cell was measured in a rectangular section from one confocal plane over time (see Fig. S3A). All time frames were evaluated with the same selection.

Microtubule bundle intensity of a single cell during collapse of the neighbouring cell was measured in both, the first available time frame before collapse and after collapse and relative values were obtained by division. Values were normalized by division with values from neighbouring cells, not adjacent to collapsed cells.

**Microtubule intensity within aspiration assays**

Microtubule intensity (35S::MAP4-GFP) epidermis cells was measured in selections from one confocal plane over time. All time frames were evaluated with the same selection, but the selection was moved if the registration did not allow stable tracking of the aspirated cell. The same selection was used for reference cells (neighbouring, non-aspirated cells). Time series data was smoothed by taking the mean of a period of 1.8 s (5 frames for 0.37 s interval and 9 frames for 0.2 s interval). No smoothing has been applied for long-term aspiration (10 min interval). Relative values were obtained from division with first value and normalized values from division with reference cells.

**Summary**

Plants as sessile organisms have to endure attacks and wounding during their lifecycle. Hence, they needed to evolve efficient and fast regeneration mechanisms to heal wounds and prevent further damage. While wounding studies have been performed since centuries, a deep understanding of how plants deal with wounds on a single cell level is still missing. In my work, I have addressed these questions. Chapter 1 gives a brief introduction to wounding studies on whole tissues and organs. Further, it elucidates on single cell ablation studies, ranging from early investigation of positional information to primary and secondary messenger analyses. The chapter aims to draw attention to the possibilities of studying cellular responses after wounding in vivo and in situ under controlled conditions.

In Chapter 2, restorative divisions and their importance for tissue regeneration are introduced. Within this study, we showed that those periclinal, asymmetric divisions occur only at the inner side of ablations, are universal for the whole meristem and lead to eventual cell fate changes of the outer daughter cells touching the wound. Furthermore, the chapter shows the importance of stem cell regulators PLETHORA and key components of the stem cell niche transcriptional program, which is supporting the execution of those restorative divisions. Finally, it shows that restorative divisions accumulate between 5 and 12 hours after ablation and require normal cell cycle progression.

In Chapter 3, we discovered a small auxin accumulation in cells continuously adjacent to ablated cells. These cells often continuously divided periclinally to regenerate the wounded tissue – a behaviour that we could induce with exogenous auxin application, even until a level of tumorous overproliferation at the wound sites. We also showed the strong induction of the wound-responsive expression of ERF115 upon auxin. Finally, we show how the maintenance of turgor pressure is crucial for the induction of restorative divisions and reveal a link between cell expansion towards the wound and speed of division initiation. This study shows a universal inhibition of restorative divisions in hypoosmotic conditions, suggesting a crucial role for turgor-driven cell expansion and division plane selection.

In Chapter 4, the wound signal responsible for the expression of ERF115 in wound-adjacent cells is investigated. We showed that ROS signalling, auxin signalling via ARF transcription factors and PEPR receptor signalling are crucial enhancers of ERF115 expression. Further, our bioinformatics analysis of the promoter and co-expression data supports the JA and BL enhanced expression of ERF115. However, while our study provides a long list of possible enhancers of ERF115, the actual activation signal remains mysterious. Histone

acetylation datasets and our bioinformatics investigation suggest a complex involvement of pathogen related genes and multiple repressor and activator complexes.

In chapter 5, we take on the previous observation of cell expansion driven restorative divisions and show how tissue stretching that is translated in cell width increase is sufficient to mediate division plane change. Further, we reveal a connection of expansion rate and MT polymerisation and array orientation in the root meristem. Finally, we show how MT bundle stability can be increased through fast stretching or deformation of meristematic cells. While the underlying molecular mechanism of these processes remain unknown, the provided insights suggest that a basic cell expansion/stretching-MT interdependence is sufficient to explain the observed division plane switches after wounding and the contribution of inner vs. outer tissues during the regeneration process.